Research on

Engineering Structures & Materials

Special Focus On

Light Alloy and
Composite Materials

Edited by
Burak Dikici
Bilge Demir

Research Group

The International Journal of **Research on Engineering Structures and Materials (RESM)** is a peer-reviewed open access journal (p-ISSN: 2148-9807; o-ISSN: 2149-4088) published by MIM Research Group. It is published in February, June, September, and December.

The main objective of RESM is to provide an International academic platform for researchers to share scientific results related to all aspects of mechanical, civil and material engineering areas.

RESM aims the publication of original research articles, reviews, short communications technical reports, and letters to the editor on the latest developments in the related fields.

All expenditures for the publication of the manuscripts are most kindly reimbursed by *MIM Research Group*. Thus, authors do not need to pay for publishing their studies in the journal.

The scope of the journal covers (but not limited to) behavior of structures, machines and mechanical systems, vibration, impact loadings and structural dynamics, mechanics of materials (elasticity, plasticity, fracture mechanics), material science (structure and properties of concrete, metals, ceramics, composites, plastics, wood, etc.,), nano-materials performances of new and existing buildings and other structural systems, design of buildings and other structural systems, seismic behavior of buildings and other structural systems, repair and strengthening of structural systems, case studies and failure of structural systems, safety and reliability in structural and material engineering, use of new and innovative materials and techniques in energy systems and mechanical aspects of biological systems (biomechanics and biomimetics).

The topics covered in RESM include:

- Structural Engineering
- Mechanical Engineering
- Material Engineering
- Earthquake Engineering
- Nano-technology
- Energy Systems
- Biomechanics and Biomimetics

Abstracting and Indexing
Please visit http://www.jresm.org for more information.

Graphics and Design

H Ersen Balcioglu ersen.balcioglu@usak.edu.tr
Yunus Demirtaş yunus.demirtas@usak.edu.tr

RESEARCH on
ENGINEERING STRUCTURES &
MATERIALS

RESEARCH on ENGINEERING STRUCTURES & MATERIALS

Editorial Board

Advisory Board Members

Yasin	Alemdag	Turkey
Duygu	Alparslan	Turkey
Irekti	Amar	Algeria
Carla Tatiana Mota	Anflor	Brazil
Ozgur	Avsar	Turkey
Ayse	Aytac	Turkey
Hüseyin Ersen	Balcıoğlu	Turkey
Kleber	Bianchi	Brazil
Sanjay Kumar	Chak	India
Leda	Coltro	Brazil
Eduardo Costa	Couto	Brazil
Thiago	da Silveira	Brazil
Hasan	Demir	Turkey
Umit Bilge	Demirci	France
Leonid	Director	Russia
Yavuz	Ergün	Turkey
TUBA	Ersen Dudu	Turkey
Carlos Eduardo Marcos	Guilherme	Brazil
Alper	Gurarslan	Italy
Ahmet	Güral	Turkey
Saddam	Hossain	Bangladesh
Liércio André	Isoldi	Brazil
Berrin	ikizler	Turkey
Ali	Karaipekli	Turkey
Alp	Karakoc	Finland
Mehdi	Khorasanian	Iran
João Paulo Silva	Lima	Brazil
Gabriela	Lujan Brollo	Brazil

Advisory Board Members

Avik	Mahata	USA
K. K.	Mahato	India
Upendra K.	Mallela	India
Najoua	Mekaddem	Tunisia
Suha Orcun	Mert	Turkey
Márcio Wrague	Moura	Brazil
Muhammad	Muddassir	Germany
Engin	Nacaroglu	Turkey
Susmita	Naskar	USA
Mu	Naushad	SAUDI ARABIA
Olga	Netskina	Russia
Hayri B.	Ozmen	Turkey
Fehime	Özkan	Turkey
Charlei Marcelo	Paliga	Brazil
Krishna Murari	Pandey	India
Matheus	Poletto	Brazil
Mauro de Vasconcellos	Real	Brazil
Raif	Sakin	Turkey
Kamyar	Shirvani Moghaddam	Australia
Hossein	Taghipoor	Iran
Paulo	Teixeira	Portugal
Canan	Uraz	Turkey
Abid	Ustaoglu	Turkey
Kursat Oguz	YAYKASLI	Turkey
Şeyda	ZORER ÇELEBİ	Turkey

In This Issue

In This Issue

ABSTRACTING / INDEXING

The international journal of Research on Engineering Structures and Materials (RESM) is currently Absracted/Indexed by CrossRef, Google Scholar, Universal Impact Factor, Scientific Indexing Service, Research Bible, CiteFactor, Electronic Journal Library, Open Academic Journals Index, Global Impact Factor, Directory of Research Journals Indexing, Materials Science & Engineering Database (ProQuest) Engineering Journals (ProQuest), ULAKBİM TR Index (Tubitak) and under evaluation by many other respected indexes.

Check web site for current indexing info.
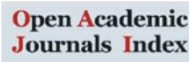
Research Article

Flexural properties of glass fiber/epoxy/MWCNT composites

Özgür Demircan*[1, 2], Pınar Çolak[1], Kemal Kadıoğlu[1], Erdinç Günaydın[1]

[1]Metallurgical and Materials Engineering Department, Faculty of Engineering, Ondokuz Mayıs University, Samsun, Turkey
[2]Department of Nanoscience and Nanotechnology, Graduate School of Science, Ondokuz Mayıs University, Samsun, Turkey

Article Info	Abstract
	Glass fiber/epoxy resin/multi-walled carbon nanotubes (MWCNTs) were used to fabricate the nano materials integrated thermoset composite materials in this study. Thermoset composites with and without nano materials were fabricated using resin transfer molding (RTM) methods. In order to characterize fabricated samples, three-point flexural tests were used. The best improvement of the flexural modulus and strength with 19% and 7% were obtained by the samples in the 90° direction and MWCNTs compared to the samples without MWCNTs. An increase in interfacial adhesion between glass fibers and epoxy matrix due to the existing of the carbon nanotubes was the reason of the improvement of the flexural properties of carbon nanotubes integrated composites.

1. Introduction

The using of thermoplastics and thermosets polymeric composite materials were considerably developed in recent years. Nano materials can be used as an assistant factor for strengthening of the composites. Carbon nanotubes (CNTs) have superior properties such as, strength and stiffness, with high aspect ratio. Because of unique properties of CNTs (such as Young's modulus of ca. 1 TPa and tensile strength of ca. 200 GPa), CNTs has become an ideal candidate for polymer reinforcement [1]. In the literature, some articles were found addressing the flexural properties of CNT modified laminates [2-10].

Agnihotri et al. [2] studied effect of carbon nanotube grafting on the wettability and average mechanical properties of carbon fiber/polymer multiscale composites. They found that CNT grafting leads to a significant improvement in interfacial shear strength as well as flexural and tensile response of carbon fiber/polymer composites with the epoxy resin. Prusty et al. [3] studied mechanical, thermomechanical, and creep performance of CNT embedded epoxy at elevated temperatures. They recorded higher flexural strength and modulus of carboxylic functionalized CNT (FCNT) embedded epoxy nanocomposites over pristine CNT (UCNT) embedded epoxy nanocomposites and neat epoxy at room temperature environment. Avcı et al. [4] studied preparation and mechanical properties of carbon nanotube grafted glass fabric/epoxy multi-scale composites. They reported that

the multi-scale composite laminates prepared with CNT grafted glass fabric represent increasing resistance to applied load after primary load fall occurred. Rahaman et al. [5] studied epoxy-carbon nanotubes as matrix in glass fiber reinforced laminated composites. They found that flexural strength, flexural modulus and storage modulus of carbon nanotubes/glass fiber/epoxy composite were considerably improved by the addition of MWCNTs. Coelho et al. [6] studied glass fiber hybrid composites molded by RTM using a dispersion of carbon nanotubes/clay in epoxy. They reported that the low clay content used and, especially, the very low MWCNT content, did not significantly alter the studied flexural properties. Zhouo et al. [7] studied fabrication and characterization of carbon/epoxy composites mixed with multi-walled carbon nanotubes. They found that the glass transition temperature, decomposition temperature, and flexural strengths were improved by infusing CNTs. Tensile behavior of MWCNT enhanced glass fiber reinforced polymeric composites at various crosshead speeds was investigated by Mahato et al. [8]. They reported that addition of 0.1% CNT and 0.3% CNT enhanced the tensile strength by 6.11% and 9.28% respectively than control GFRP composite. Panchagnula et al. [9] studied improvement in the mechanical properties of neat GFRPs with multi-walled CNTs. They found that the tensile and flexural strengths of MWCNT-GFRPs increased nearly 36.04% and 39.41% with the addition of 0.3% of MWCNTs. Interface enhancement of glass fiber fabric/epoxy composites by modifying fibers with functionalized MWCNTs was reported by Shen et al. [10]. They found that the interlaminar shear, tensile and flexural strengths of MWCNTs-grafted glass fiber fabric/epoxy composites were enhanced by 24.0%, 24.9% and 21.1%.

In the literature, it was found some researchers who they coated the surface of the reinforcements using nano materials. Lagoudas et al. [11] studied effect of carbon nanotubes on the interfacial shear strength of T650 carbon fiber in an epoxy matrix. They found that randomly oriented MWCNT and aligned MWCNT coated fibers demonstrated a 71% and 11% increase in interfacial shear strength over untreated, unsized fibers due to the presence of the nanotubes. Kim et al. [12] studied tensile strength of glass fibers with carbon nanotube–epoxy nanocomposite coating. They reported that the single fibers coated with the 0.3 wt% CNT–epoxy nanocomposite exhibited larger strength improvement than fibers with a neat epoxy coating, compared to fibers without coating. Epoxy matrix composites with carbon fiber/selectively integrated graphene as multi-scale reinforcements was investigated by Zanjani et al. [13]. They found about 51% improvements in the flexural strength in their fabricated composite materials by using nano materials. Interfacial shear strength of a glass fiber/epoxy bonding in composites modified with carbon nanotubes was reported by Gorbatikh et al. [14]. They obtained 90% improvement in interfacial shear strength by using carbon nanotubes in the fiber sizing. Demircan et al. [15] reported mechanical properties of thermoplastic and thermoset composites reinforced with 3d biaxial warp-knitted fabrics. They found about 97% and 58% improvements in the flexural modulus and strength of composites by using carbon nanotubes in the fiber sizing.

It was found little work about the three-point flexural properties of the MWCNTs integrated glass fiber epoxy thermoset composites reinforced with the non-crimp fabrics in the literature. The aim of this research was to study the effect of the MWCNTs integration on the three-point flexural properties of the thermoset composites. In this study, the flexural properties of 0.0 wt% and 0.4 wt% MWCNTs integrated specimens in the 0° and 90° directions were investigated. In order to design of the new thermoset composite materials, the results from our research can be used.

2. Experimental procedure

2.1. Constituents of Thermoset Composites

In order to fabricate nano materials integrated thermoset composites, the non-crimp fabrics (NCF) with glass fibers (Metyx Composites Ltd., Turkey), epoxy resin (DTE 1200, Duratek, Turkey) and hardener (DTS 1155, Duratek, Turkey) were used. The properties of the NCF are shown in Table 1.

Table 1 Properties of non-crimp fabric (NCF) of composites

E glass samples	Biaxial yarn 0° (warp) fibers, tex	Biaxial yarn 90° (weft) fibers, tex	Area weight of 0° warp fibers (gr/m^2)	Area weight of 90° weft fibers (gr/m^2)	Fabric weight (warp, weft and binding fibers) (gr/m^2)
LT1200E 05B 0/90	2400	1200	566	614	1187

The MWCNTs were supplied from Ege Nanotek Kimya Sanayi Limited Sirketi, Izmir, TURKEY. The properties of the MWCNTs were: 10–20 nm (the outer diameter), 5–10 nm (the interiour diameter), 10–30 micro m (length of the MWCNTs) and >200 m^2/g (the surface area of the MWCNTs). Figure 1 shows the SEM images of the MWCNTs.
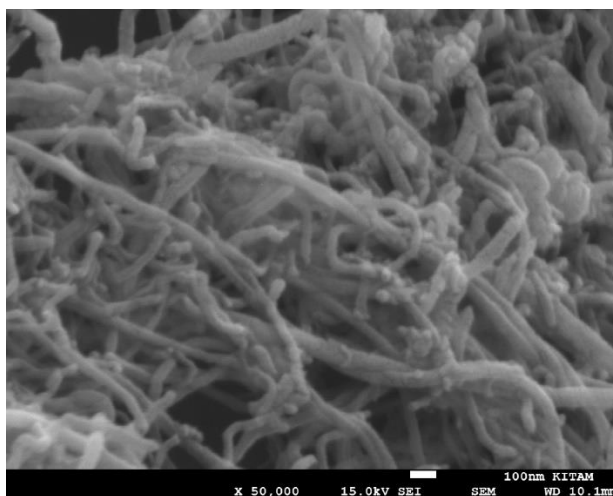
Fig. 1 SEM images of MWCNTs

2.2. Fabrication Method of Thermoset Composites

In order to fabricate the thermoset composites with nanomaterials, the resin transfer method (RTM) was chosen to manufacture four layers biaxial warp-knitted (BWK) reinforced composites plates as shown in Figure 2.

At first ethanol and MWCNTs solutions were prepared to coat each faces of the NCFs. MWCNTs were dispersed in ethanol using a magnetic stirrer device. After that the solution of MWCNTs and ethanol were stayed in an ultrasonic bath. Later, each faces of the NCFs were coated using of the solution of MWCNTs and ethanol. After coating of the NCF with

the MWCNTs solution, the specimens were left for two days in the room temperature to ensure the full evaporation of the ethanol. Then, MWCNTs coated four layers fabrics were laid in mold cavity in a symmetrical stacking sequence ($[90_{wa}/0_{we}/90_{wa}/0_{we}]_s$) of the RTM system (Figure 3).

Fig. 2 The RTM apparatus

$$[90_{wa}/0_{we}/90_{wa}/0_{we}]_s$$
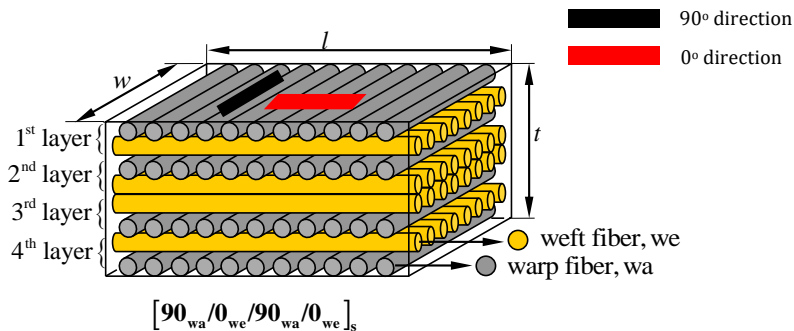
Fig. 3 Schematic drawing of the thermoset composites. Here, l: length, w: width and t: thickness of the fabricated composite plate

In the fabricated composite plates, the carbon nanotubes weight percentages were 0.4 wt %. After fabricating of the composites, burn off method in a muffle furnace was performed in order to determine the percentages of each of the constituents in the thermoset composites. The burn off process of the composites was conducted according to the ASTM D3171–99 standards. Table 2 shows the fiber volume fraction and thickness of the fabricated composites.

Table 2 Fiber volume fraction and thickness of fabricated composites

Composites	Weft Vf (%)	Warp Vf (%)	Binding Vf (%)	Total (warp, weft and binding) Vf (%)	Thickness (mm)
0.0 wt % MWCNT	17.4	16.1	0.66	34.2	5.4
0.4 wt % MWCNT	16.8	18.2	0.28	35.3	5.0

2.3. Characterization of Thermoset Composites

The ASTM-D790 test standards were used to prepare the specimens and test conditions for the the three-point flexural tests. The INSTRON 5982 100KN universal testing machine type with flexural tests apparatus was used to perform the three-point flexural tests. The tests speeds and the sample dimensions were 1 mm/min and 110 x 15 x 5.0–5.4 mm³ for the three-point flexural tests. The test span lengths were 74 mm and 90 mm. Three specimens from each type of the composite panels were tested both in the 0° and 90° directions. The 0° and 90° directions of the specimens were cut after fabricating of the composite panels. The 0° and 90° directions of the specimens can be seen in Figure 3 (0° direction was shown by red color and 90° was shown by black color).

The flexural strength, modulus and strain were calculated using following Equations (1-3) [16].

$$\sigma_f = 3PL/bd^2 \tag{1}$$

$$\epsilon_f = 6Dd/L^2 \tag{2}$$

$$E_B = L^3 m/4bd^3 \tag{3}$$

Where, σ_f is the flexural strength (MPa); P is the flexural load (N); L is the support span length (mm); b is the sample width (mm); d is the sample thickness (mm); E_B is the flexural modulus (GPa); m is the slope of the tangent to the initial straight-line portion of the load-deflection curve; ε_f is the flexural strain (%); D is the maximum displacement of the centre of the sample (mm).

3. Results and Discussion

The results of the flexural properties of the specimens are shown in Figure 4. The flexural modulus and strength of the specimens with 0 wt% and 0.4 wt% MWCNTs were 12.8 GPa, 375.2 MPa, 15.9 GPa and 403.7 MPa in 90° direction and these were 17.2 GPa, 503.3 MPa, 20.1 GPa and 525.5 MPa in 0° direction. CNT integrated specimens showed 19% and 7% improvement of flexural modulus and strength against specimens without CNTs in 90° degree direction. That was 14% and 4% in 0° degree direction.

The specimens with 0 wt% MWCNT had a higher flexural modulus and strength in the 0° direction (17.2 GPa and 503.3 MPa) than those in the 90° direction (12.8 GPa and 375.2 MPa) due to the higher volume fraction of the weft fibers (17.4%) than the warp fibers (16.1%). Additionally, composite materials reinforced with thin plies showed higher mechanical properties than that was with thick plies [17-20]. The weft fibers (thin plies) of the specimens are aligned with the length of specimen in the 0° direction. The warp fibers (thick plies) of the specimens are aligned with the length of specimen in the 90° direction. Because of the alignment of thin fibers with the length of specimen in the 0° direction, the results of flexural modulus and strength were higher in the 0° direction compared to the 90° direction.

Since the volume fraction of the warp fibers (18.2%) is higher than the weft fibers (16.8%) with 0.4 wt% MWCNT, one will expect the specimens had a higher flexural modulus and strength in the 90° direction than those in the 0° direction. The fact that flexural modulus and strength in the 0° direction was higher than those in the 90° direction with 0.4 wt% MWCNT. As mentioned earlier, because of the alignment of thin fibers with the length of specimen in the 0° direction, the results of flexural modulus and strength were higher in the 0° direction compared to the 90° direction.

The flexural properties of the thermoset composites were improved by integrating of the MWCNTs on the surface of the NCF. The best improvement of the flexural modulus and strength with 19% and 7% were obtained from the samples in the 90° direction and 0.4 wt% MWCNTs. The interfacial properties between fiber and epoxy matrix could be improved by coating of the fiber surface with CNTs nano particles and this might be the possible reason of the enhancement of the flexural properties of composites. Since the CNTs having superior mechanical properties with large surface area, they improve mechanical properties of composites.
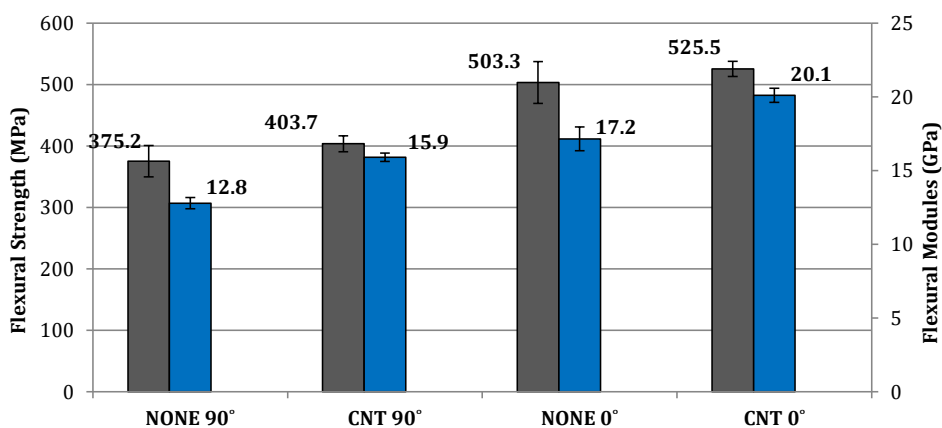
Fig. 4 Results of flexural properties of thermoset composites

Comparing these results with others found in the literature, 11% and 4.7% increase in flexural strength and modulus for addition of 0.1% pristine CNT (UCNT) in epoxy was reported by Prusty et al. [3]. About 14% increase in flexural strength for addition of 0.3% oxidized MWCNTs in epoxy was reported by Avcı et al. [4]. 27% increase in flexural modulus for carbon nanotubes/glass fiber/epoxy laminates containing 0.5% MWCNT was reported Rahaman et al. [5]. 11.7% increase in flexural modulus for addition of 0.4% MWCNT and 28.3% in flexural strength in epoxy was reported by Zhouo et al. [7]. The good agreement between our results and literature supported our mechanical tests.

4. Conclusions

The addition of the carbon nanotubes on the surface of the reinforcements enhanced the flexural modulus and strength of the thermoset composites.

From the results of this study, the following conclusions can be drawn:

- The results of flexural properties were higher in the 0° direction compared to the 90° direction.

- Composite materials reinforced with thin plies showed higher mechanical properties than that was with thick plies in the same volume fraction.
- The best improvement of the flexural modulus and strength with 19% and 7% were obtained from the specimens in the 90° direction and 0.4 wt% MWCNTs due to the superior properties of carbon nanotubes.
- The highest results of flexural modulus and strength were achieved with 0.4 wt% MWCNTs in 0° direction.
- There was a good agreement of results of flexural tests of nano materials integrated composites from literature and from us.

In future study, we will try to investigate the impact properties of the nano materials integrated composite materials with the NCFs reinforcements.

Acknowledgment

References

[1] Meyyappan M. Carbon Nanotubes Science and Applications, CRC Press, New York, ISBN 9780849321115, 2005

[2] Agnihotri KP, Padhee SS, Bedi SH. Effect of carbon nanotube grafting on the wettability and average mechanical properties of carbon fiber/ polymer multiscale composites, Polymer Composites, 2018; 39: 1184-1195. https://doi.org/10.1002/pc.24714

[3] Prusty KR, Ray CB, Tathore KD. Mechanical, thermomechanical, and creep performance of CNT embedded epoxy at elevated temperatures: An emphasis on the role of carboxyl functionalization. Journal of Applied Polymer Science, 2017; 134: 44851-44862.

[4] Avci A, Eskizeybek V, Gülce A. Preparation and mechanical properties of carbon nanotube grafted glass fabric/epoxy multi-scale composites. Advanced Composite Materials, 2017; 26: 169–180. https://doi.org/10.1080/09243046.2015.1052188

[5] Rahaman A, Imran M. Epoxy-carbon nanotubes as matrix in glass fiber reinforced laminated composites. Fullerenes, Nanotubes and Carbon Nanostructures, 2017; 25: 559–562. https://doi.org/10.1080/1536383X.2017.1330264

[6] Coelho FAL, Ramirez MA, Becker D, Amico CS, Silva da VL, Sene ST. Glass fiber hybrid composites molded by rtm using a dispersion of carbon nanotubes/clay in epoxy. Materials Research, 2013; 16: 1128–1133. https://doi.org/10.1590/S1516-14392013005000104

[7] Zhou Y, Pervin F, Lewis L, Jeelani S. Fabrication and characterization of carbon/epoxy composites mixed with multi-walled carbon nanotubes. Materials Science and Engineering A, 2008; 475: 157–165. https://doi.org/10.1016/j.msea.2007.04.043

[8] Mahato KK, Rathor e DK, Prusty RK, Dutta K and Ray BC. Tensile behavior of MWCNT enhanced glass fiber reinforced polymeric composites at various crosshead speeds. IOP Conf. Ser. Mater. Sci. Eng., 2017; 178. https://doi.org/10.1088/1757-899X/178/1/012006

[9] Panchagnula KK, Kuppan P, Improvement in the mechanical properties of neat GFRPs with multi-walled CNTs. J Mater Res Technol., 2018; https://doi.org/10.1016/j.jmrt.2018.02.009

[10] Zeng S, Duan P, Shen M, Xue Y, Lu F, Lu, Y, Interface enhancement of glass fiber fabric/ epoxy composites by modifying fibers with functionalized MWCNTs. Composite Interfaces, 2018; https://doi.org/10.1080/09276440.2018.1499354

[11] Sager RJ, Klein PJ, Lagoudas DC, Zhang Q, Liu J, Dai L, Baur JW. Effect of carbon nanotubes on the interfacial shear strength of T650 carbon fiber in an epoxy matrix.

Composite Science and Technology, 2009; 69: 898–904. https://doi.org/10.1016/j.compscitech.2008.12.021

[12] Siddiqui NA, Sham ML, Tang BZ, Munir A, Kim JK. Tensile strength of glass fibers with carbon nanotube–epoxy nanocomposite coating. Composite Part A, 2009; 40: 1606 – 1614. https://doi.org/10.1016/j.compositesa.2009.07.005

[13] Zanjani JSM, Okan BS, Menceloglu YZ, Yıldız M. Nano-engineered design and manufacturing of high-performance epoxy matrix composites with carbon fiber/selectively integrated graphene as multi-scale reinforcements. RSC Advances, 2016; 6: 9495–9506. https://doi.org/10.1039/C5RA23665G

[14] Godara A, Gorbatik L, Kalinka G, Warrier A, Rochez, O, Mezzo L, Luizi F, Vuure AWV, Lomov SV, Verpoest I. Interfacial shear strength of a glass fiber/epoxy bonding in composites modified with carbon nanotubes. Composite Science and Technology, 2010; 70: 1346–1352. https://doi.org/10.1016/j.compscitech.2010.04.010

[15] Al-darkazali A, Çolak P, Kadıoğlu K, Günaydın E, Inanç I, Demircan Ö. Mechanical properties of thermoplastic and thermoset composites reinforced with 3d biaxial warp-knitted fabrics, Applied Composite Materials, 2018. https://doi.org/10.1007/s10443-018-9725-x

[16]ASTM D790:2010. Standard test methods for flexural properties of unreinforced and reinforced plastics and electrical insulating materials.

[17] Tsai SW, Sihn S, Kim RY. Thin-ply composites. In: 46th AIAA/ASME/ASCE/AHS/ASC structures, structural dynamics & materials conference, Austin, Texas, 18–21 April 2005, pp. 1–5. Sawston, Cambridge: Woodhead Publishing.

[18]Sihn S, Kim RY, Kawabe K, Tsai SW. Experimental studies of thin-ply laminated composites. Composite Science and Technology, 2007; 67: 996–1008. https://doi.org/10.1016/j.compscitech.2006.06.008

[19] Guillamet G, Turon A, Costa J, Renart J, Linde P, Mayugo JA. Damage occurrence at edges of non-crimp-fabric thin-ply laminates under offaxis uniaxial loading. Composite Science and Technology, 2014; 98:44–50. https://doi.org/10.1016/j.compscitech.2014.04.014

[20] Yokozeki T, Aoki Y, Ogasawara T. Experimental characterization of strength and damage resistance properties of thin-ply carbon fiber/toughened epoxy laminates. Composite Structures, 2008; 82: 382–389. https://doi.org/10.1016/j.compstruct.2007.01.015

Research Article

Wear performance investigation of AlSi₈Cu₃Fe aluminum alloy related to aging parameters

Ebru Baser, Alper Incesu, Sedef Sismanoglu, Ali Gungor*

Department of Metallurgical and Materials Engineering, Karabuk University, Karabuk, TURKEY

Article Info	Abstract
	Aluminum silicon alloys are the most preferred alloys for industrial applications due to their ease of production and lightness. It is important to improve the mechanical properties of these materials in order to increase their usage. Wear properties are one of these mechanical properties that can be improved. In this present investigation, 3 different artificial aging durations; 2hrs, 4 hrs, 8 hrs aging at 200 °C were applied after solution heat treatment for 4 hrs. at 540 °C to the AlSi8Cu3Fe alloy. Microstructural analysis, mechanical tests were applied to understand the effect of aging parameters on wear performance and also hardness values of AlSi8Cu3Fe alloy. According to the results obtained from tests and analyzes, the highest wear resistance was reached on the 4 hrs. aged sample.

1. Introduction

In recent year's aluminum, magnesium and similar materials that have the high specific strength (strength/density) have become the focus of attention by the aviation and automotive industries where weight gain is important [1–3]. The weight gain in these areas will reduce fuel consumption and therefore also reduce greenhouse gasses (GHGs) emissions. It is important to improve the mechanical properties of these materials in order to increase their use. Wear properties are one of these mechanical properties that can be improved. Factors that increase the wear rate of material adhesion, abrasion, delamination, thermomechanical effect, fatigue, sub-surface damage, and oxidation depending on the sliding conditions (contact load, relative speed, counter surface, dry or lubricated) nature of contact (pin on disc/ring/bush), metallic properties of sliding surfaces, oxidation and thermal softening behavior [4,5]. Alloying, thermo-mechanical processes, heat treatments etc. are among the methods that can be applied to develop these properties [6].

One of the most preferred elements in the alloying of aluminum metal is silicon. Due to the high fluidity provided by the silicon, it is possible to produce parts with complex and thin sections by casting. Silicon provides fluidity to the liquid metal while also reducing the tendency to tear on the spattered part [6]. Therefore, Al-Si based alloys results in as attractive combinations of low coefficient of thermal expansion, high elastic modulus, excellent wear resistance and good thermal stability [7]. Copper can be used up to 5% as an alloying element when high strength values are required but corrosion resistance is not very important [6]. Iron is generally found as an impurity in aluminum alloys especially in Al-Si alloy. It is usually considered detrimental and has the potential to seriously degrade

castability. In the absence of Si, iron forms Al_3Fe and Al_6Fe intermetallic compounds with aluminum. These intermetallics are highly stable but have brittle nature which, negatively affects the ductility of the part and also reduces the corrosion resistance [6]. When Si is present, the dominant phases are the hexagonal α-Al_8Fe_2Si phase and the monoclinic/orthorhombic β-Al_5FeSi phase [8]. If Mg is present with Si in Al, π-$Al_8FeMg_3Si_6$ phase can form [9]. To minimize the harmful effects of iron, some manganese or cobalt is added to the alloy. Zinc is the another alloying element that has a relatively high solubility in aluminum both at high temperature and at room temperature; also, it is stated that there is no significant effect of zinc addition below 3% on the Al-Si alloys [10].

Aluminum-silicon alloys have been commonly used as components which have sliding movement with a contacting counter body. The performance of these components greatly depends on material-related parameters, e.g., shape, size, content, and type of distribution of given micro constituents etc. [11]. Also, it can be argued that service conditions have a considerable effect on the wear performance of Al-Si alloys.

In this study, attempts have been made to determine wear behavior of T6 heat treatment (artificial aging after solution heat treatment) applied to hypoeutectic Al-Si alloy which is commercially produced as AlSi8Cu3Fe aluminum alloy.

2. Materials and Method

The chemical composition of the alloy in this study was given in Table 1. In accordance with T6 heat treatment, artificial aging heat treatment was applied at a temperature of 200 °C for 2, 4 and 8 hrs. after application of the solution heat treatment for 4 hrs. at 540 °C. After aging heat treatment, all specimens were cooled by water at room temperature.

Table 1 A chemical composition of AlSi8Cu3Fe aluminum alloy (in wt.%)

ISO Norm	Fe	Si	Cu	Mn	Mg	Zn	Ni	Ti
AlSi8Cu3Fe	1.00	7.50-9.00	3.00-4.00	0.50	0.30	1.00	0.20	0.20

X-Ray Diffraction (XRD) analysis for phase identification was carried out using Rigaku ULTRA IV Diffractometer with Cu-Kα X-ray radiation under 40-kV acceleration voltage and 40 mA current. A scan speed of the measurements was 3 deg./min. and scan range was between 30° to 90°. ICDD database was used to identify the phases of the X-ray diffraction pattern of the alloys.

Detailed microstructural investigations of alloys are carried out by Carl Zeiss ULTRA PLUS FESEM Field Emission Scanning Electron Microscopy (FESEM). Also, Energy Dispersive Spectroscopy (EDS) was performed to assess the chemical compositions of the phases.

Brinell hardness test was performed via Q250 M QNESS macro hardness test machine using 62.5 kg loads with a holding time of 20 seconds and 2.5 mm diameter indenter. Brinell hardness values of the specimens were the averages of measurements taken at 5 different points at one indent per point.

Wear tests were conducted on UTS Tribometer T10/20 at forward and reverse movement module. AISI 52100 steel brand ball was used during the test. Wear tests were carried out

at 130 mm/s. test speed with a stroke distance of 10 mm. 5 N loads were applied to the samples and 500 meters distance were taken. Lubricant was not used.

3. Results and Discussions

XRD analyses result of sample aged at 200 °C for 8 hrs. sample were given in Figure 1. In XRD analysis, only peaks of Al and Si phases were observed, any other phases were not detected. This may be due to the low amount of other phases in the structure and overlapping peaks of intermetallic phases with Al and Si peaks. Possible phases are investigated in the literature. Sallah and Omar [12] have determined the phases of Al, Si, Al2Cu, β-Al5FeSi, Al5Cu2Mg8Si6 by XRD analysis in similar alloys to the studied AlSi8Cu3Fe alloy. Some of these phases which could not be determined with XRD analysis were determined in EDX analysis.
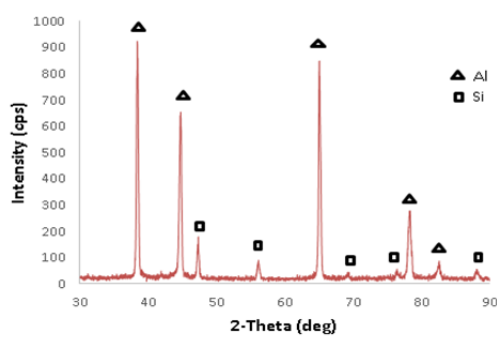
Fig. 1 XRD analyses result of sample aged at 200 °C for 8 hrs

Figure 2 shows SEM micrographs of aged alloys. Figure 3 shows EDS analyzed the region of aged at 200 °C 8 hrs. alloy and EDS results of the phases in at.%.
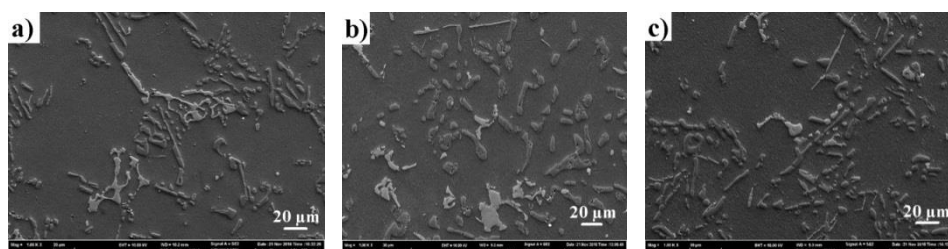
Fig. 2 SEM micrographs of aged alloys at 200 °C for; a) 2 hrs. b) 4 hrs. c) 8 hr

In both aging durations, the microstructure is relatively coarse and mostly dendritic. Three different phases were observed from SEM-EDS analyses, namely; α-Al matrix, Si and β-Al$_5$FeSi. α-Al matrix contains low amount of Si, Cu, and Fe elements. Si phase contains low amount of Al and intermetallic phase composed of mainly Al and other elements; Si, Cu, Fe, Mg and Mn elements. Figure 3 and Table 2 show microstructural features and their composition.
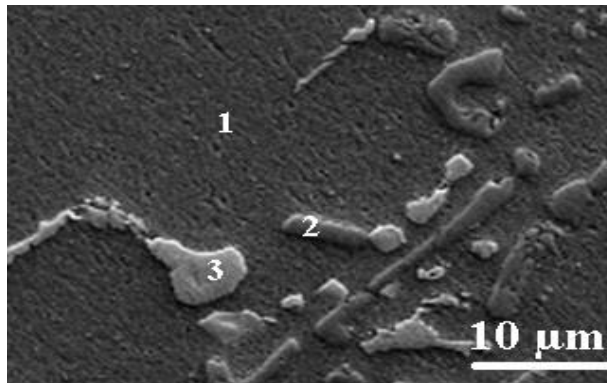
Fig. 3 EDS analysis region of the alloy aged at 200 °C for 8 hrs

Table 2 EDS results of the phases.

Spectrum (at.%)	Al	Si	Cu	Fe	Mg	Ti	Mn	Ni
Point 1	94.99	1.16	2.00	0.59	0.00	0.17	0.00	0.21
Point 2	2.17	97.61	0.00	0.10	0.00	0.08	0.00	0.00
Point 3	63.40	11.93	4.17	15.09	5.02	0.24	5.02	0.15

Brinell hardness values from five different points of aging application samples and average values of them are given in Table 3, and graphical comparison of Brinell Hardness values as a function of aging time was given in Figure 4. Brinell hardness's of specimens are 106.8 HB, 89.2 HB, and 120.6 HB with an increasing aging duration, respectively. It is well known that the Si particles have higher hardness and lead to an increase in wear resistance [4]. With the increase in the aging time, it was found that the Si containing particles exhibited a noticeable effect on hardness and wear especially after 4 hours aging period.

Table 3 Brinell hardness measurement results related about aging duration

Aging Duration	Indentation 1	Indentation 2	Indentation 3	Indentation 4	Indentation 5	Average
2 hrs.	109	107	106	105	107	106,8
4 hrs.	92,3	84,0	89,4	90,8	89,7	89,2
8 hrs.	121	117	121	122	122	120,6
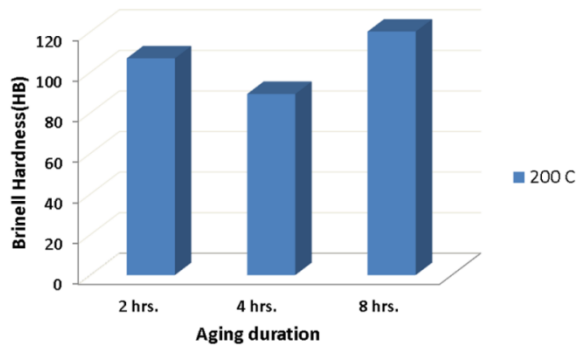
Fig. 4 Graphical comparison of Brinell hardness values of the samples

Effect of aging time on the wear loss of the alloy was given in Figure 5. Wear loss of specimens are 1.9, 1.7 and 2.6 in mg with an increasing aging duration, respectively.
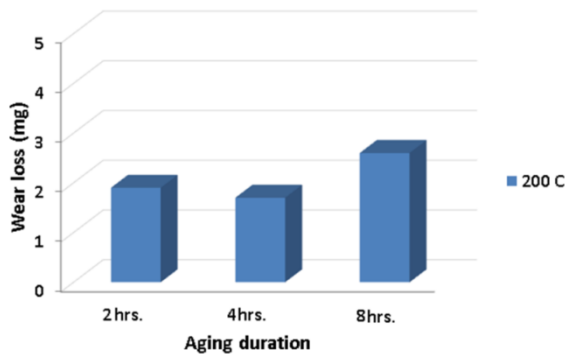
Fig. 5 Wear loss of the aged alloy

When Figure 4 and Figure 5 are compared, we see that both of them follow a similar trend. As aging duration is increased from 2 hrs. to 4 hrs., both hardness value and wear loss of the AlSi8Cu3Fe alloy decreases. Further, increasing aging duration to 8 hrs., both hardness value and wear weight loss increase to maximum values. The reason is that intermetallic particles in the structures became larger with aging duration from 2 hrs. to 4 hrs. after this duration Si-based intermetallic grows faster than the intermetallics. Therefore, these large particles on the surface resulted in less weight loss due to the breakage during wear. Lasa and Rodriguez-Ibabe express that the high wear resistance is generally attributed to the presence of hard silicon particles distributed throughout the matrix [13]. It can be said that optimum silicon particle size was approached at 4 hrs. aging for higher wear resistance.

4. Conclusion

In this study, the wear performance of the AlSi8Cu3Fe aluminum alloy was investigated depending on the artificial aging time. Solution heat treatment of the alloy was carried out at 540 °C for 4 hours. After that aging heat treatment was applied at a temperature of 200 °C for 2, 4 and 8 hrs. Minimum weight loss was detected in 4 hrs. aged sample which has also lowest hardness. On the other hand, the alloy aged for 8 hrs. has the highest hardness and weight loss.

From the results of this study, the following conclusions can be drawn:

- Microstructure of all specimens composed of α-Al matrix, Si and Al-rich intermetallic phase containing Si, Cu, Fe, Mg and Mn elements. From the ratio of the elements, it is thought to be β-Al$_5$FeSi.

- Although the wear rates and hardness values are parallel to each other depending on the aging time, it is inferred from the performance of the heat-treated specimens that the wear performance of the Al-Si based alloys is governed by the size and distribution of coarse Si particles, and that the impact of hardness is only secondary.

Acknowledgement

References

[1] Cole GS, Sherman AM. Light weight materials for automotive applications. Mater Charact 1995;35:3–9. https://doi.org/10.1016/1044-5803(95)00063-1
[2] Miller WS, Zhuang L, Bottema J, Wittebrood A, De Smet P, Haszler A, et al. Recent development in aluminium alloys for the automotive industry. Mater Sci Eng A 2000;280:37–49. https://doi.org/10.1016/S0921-5093(99)00653-X
[3] Hirsch J. Recent development in aluminium for automotive applications. Trans Nonferrous Met Soc China 2014;24:1995–2002. https://doi.org/10.1016/S1003-6326(14)63305-7
[4] Saklakoglu N, Gencalp Irizalp S, Ercayhan Y, Birol Y. Investigation of wear behaviour of thixoformed and conventional gravity cast AlSi8Cu3Fe alloys. Ind Lubr Tribol 2014;66:46–50. https://doi.org/10.1108/ILT-09-2011-0067
[5] Dwivedi DK. Adhesive wear behaviour of cast aluminium–silicon alloys: Overview. Mater Des 1980-2015 2010; 31: 2517–2531. https://doi.org/10.1016/j.matdes.2009.11.038
[6] Handbook M. Vol. 2-Properties and Selection: Nonferrous Alloys and Special-Purpose Mater. ASM Inter 1990:1119–1124.
[7] Wang F, Liu H, Ma Y, Jin Y. Effect of Si content on the dry sliding wear properties of spray-deposited Al–Si alloy. Mater Des 2004; 25:163–166. https://doi.org/10.1016/j.matdes.2003.08.005
[8] Kral MV. A crystallographic identification of intermetallic phases in Al–Si alloys. Mater Lett 2005;59:2271–2276. https://doi.org/10.1016/j.matlet.2004.05.091
[9] Taylor JA. Iron-containing intermetallic phases in Al–Si based casting alloys. Procedia Mater Sci 2012;1:19–33. https://doi.org/10.1016/j.mspro.2012.06.004

[10]   Gowri S, Samuel FH. Effect of alloying elements on the solidification characteristics and microstructure of Al-Si-Cu-Mg-Fe 380 alloy. Metall Mater Trans A 1994;25:437–448. https://doi.org/10.1007/BF02647989

[11]   Prasad BK, Venkateswarlu K, Modi OP, Jha AK, Das S, Dasgupta R, et al. Sliding wear behavior of some Al-Si alloys: Role of shape and size of Si particles and test conditions. Metall Mater Trans A 1998; 29: 2747–2752. https://doi.org/10.1007/s11661-998-0315-7

[12]   Salleh MS, Omar MZ. Influence of Cu content on microstructure and mechanical properties of thixoformed Al–Si–Cu–Mg alloys. Trans Nonferrous Met Soc China 2015;25:3523–3538. https://doi.org/10.1016/S1003-6326(15)63995-4

[13]   Lasa L, Rodriguez-Ibabe JM. Effect of composition and processing route on the wear behaviour of Al–Si alloys. Scr Mater 2002; 46: 477–481. https://doi.org/10.1016/S1359-6462(02)00020-9

Research Article

Corrosion behavior of heat treated Mg-xZn (x=0.5 – 3) alloys

Erkan Koç[*,a,1], Fozi Mustafa Salem Makhlof[b,2]

[1]Department of Metallurgical and Materials Engineering, Karabük University, Karabük
[2]Department of Mechanical Engineering, Higher Institute of Comprehensive Occupations, Misrata, Libya

Article Info	Abstract
	The purpose of this study is to investigate the effects of zinc (0,5-1-2-3 wt.%) additions and heat treatment parameters on the microstructure, hardness and corrosion properties of magnesium zinc alloys. After the solution heat treatment at 400ºC, the samples subjected to 8 and 16 hours heat treatment. Microstructure studies showed that the grain size decreased with the increase of Zn content and the MgZn intermetallic phase was formed by the addition of 3 wt.% Zn. Hardness of the samples was increased with increase of Zn content before and after heat treatment. For the as-cast samples, as the amount of Zn increased, corrosion current density (I_{corr}) and corrosion rate (P_i) increased. As the amount of Zn increased, I_{corr} and P_i values decreased after 8 hours and 16 hours of heat treatment respectively. It can be suggested that in the galvanic couple of Mg-3Zn, α-Mg matrix phase behaves as an anode and MgZn intermetallic phase behaves as a cathode.

1. Introduction

Magnesium and its alloys with good ductility, strength and good corrosion resistance, as well as having low density, are becoming the focus of interest for researchers in the automotive, aerospace and electronics industries [1-3]. Mg with a density of 1.74 gr/cm^3, is 36% and 78% lighter than Al and steel respectively and magnesium alloys are the lightest metallic material used today as a construction material [1-5]. However, magnesium alloys which have poor corrosion resistance due to their electrochemically active conditions limit their use especially in aerospace and automotive fields [6]. Mg is a very active metal with an electrochemical standard potential value of -2.37 V at 25 ° C and -1.7 V at 3% NaCl and is used as a sacrificial anode [7]. Important studies have been done to understand the corrosion principles for magnesium and to improve the corrosion resistance through the design and development of new alloys, inhibitor addition, heat treatment and coatings [8-13]. Heat treatment may have a significant effect on the corrosion behavior due to its modifying properties in the microstructure [14]. Zn also increases the hardness, strength and also the fluidity of the alloy at ambient temperatures through the precipitation hardening [15]. Bakhsheshi-Rad et al. [6] reported that heat treatment improved the corrosion resistance of both Mg-3Zn and Mg-6Zn alloys. Xian-bin et al. [10] indicated that compared with as-cast alloy, the amount of MgZn particles decreased by the T4 treatment, and consequently T4 treatment increased the corrosion resistance while the T6 treatment decreased the corrosion resistance of the Mg-3Zn alloy in 0.1 mol/L NaCl solution. Cai et al. [15] studied on Mg-Zn alloys containing 1, 5 and 7 wt.% Zn in simulated body fluid (SBF) suggests that corrosion resistance increased with increasing Zn content in the range 1-5 wt.% despite the presence of the potentially

detrimental MgZn intermetallic. Excessive addition of Zn over 7 wt.% resulting microgalvanic corrosion acceleration. In addition, a wide variety of magnesium alloys, including magnesium-aluminium-zinc (AZ series) were investigated for in vitro and in vivo conditions for implant applications [16-20]. In this study, systematically it was aimed to investigate the effects of both zinc content and heat treatment on the corrosion behavior of the binary Mg - Zn alloys containing low levels (0.5-1-2 and 3 wt.%) of zinc.

2. Experimental Procedure

High purity magnesium (99.99 wt.%) and zinc (99.999 wt.%) which were purchased from Bilginoglu Industry in Turkey were used to prepare magnesium-zinc binary alloys by melting magnesium in a graphite crucible under argon gas atmosphere at 750ºC. In order to prevent losses due to evaporation, the addition of zinc was carried out 1 min. before the casting process. The casting process of the molten alloy was carried out using a shielded CO_2 + 0.8% SF_6 mixed gas into a cast iron mold (preheated to 250 ° C) having a length of 20 mm and a length of 200 mm. The chemical compositions of the alloys were analyzed using a chemical analysis method (Spectrolab M8 Optical Emission Spectrometer (OES)) and presented in Table 1. The samples were etched in 5 ml acetic acid, 6 gr picric acid, 10 ml distilled water and 100 ml ethanol and then observed under optical microscope (Nikon MA200) for microstructure analysis. Depending on the nominal zinc content, as-cast Mg-Zn binary alloys were designated as Mg-0.5Zn, Mg-1Zn, Mg-2Zn and Mg-3Zn, respectively.

Table 1. Chemical compositions of the as-cast magnesium-zinc binary alloys.

Alloy	Composition wt.%				
	Zn	Mn	Fe	Cu	Mg
Mg-0.5Zn	0.56	0.003	0.004	0.0002	
Mg-1Zn	1.08	0.004	0.002	0.0004	
Mg-2Zn	2.11	0.002	0.003	0.0003	Balance
Mg-3Zn	3.12	0.003	0.004	0.0003	

Hardness measurements were performed using a Vickers Hardness tester (Model Shimadzu HMV2) with a steel ball indenter of 2.5 mm in diameter under the load of 5N and maintained for 10s. Hardness values were also determined by taking averages of 5 different values.

Heat treatments were carried out for 24 hours at 400°C for homogenization (T4) and were treated at 200 ℃ for 8h and 16 h (T6) for ageing treatment. Initially, the samples were placed in the furnace and heated slowly to 400 ° C with a heating rate of 3°C / min. Samples were taken from the furnace after 24 hours and then quenched into hot water at about 60°C. After homogenization treatment, cast samples were treated at 200 ℃ for 8h and 16 h respectively, and then cooled at room temperature.

The electrochemical corrosion test was done using a potentiostat (Model VersaSTAT 3) Electrochemical corrosion experiments were performed at room temperature in a glass cell containing 3.5 wt.% NaCl solution using a standard three-electrode configuration: graphite rod as a counter-electrode, a saturated calomel electrode as a reference electrode and the sample (2.26 cm^2 exposed area) as a working electrode. Potentiodynamic polarization curves were generated by sweeping the potential from cathodic to anodic direction at a scan rate of 1 mV s^{-1}, starting from -0.50 V up to 0.50 V, versus OCP. Corrosion potential (E_{corr}), corrosion current density (I_{corr}) were calculated by extrapolation from Tafel curves using DC corrosion software. I_{corr} (mA/cm^2) is related to the corrosion rate, P_i, (mm/year) using [21]:

$$Pi = 22.85 \, x \, Icorr \tag{1}$$

3. Results & Discussion

3.1. Microstructure and hardness properties of the Mg-xZn alloys

The microstructures of the Mg-Zn binary alloys used in the study are shown in Fig. 1. Microstructure studies have shown that the grain boundaries are larger before heat treatment and grain structures are finer after heat treatment. In the literature [22], the maximum solid solubility of Zn in Mg is given 2.5 at. % (i.e. 6.2 wt.%) at the eutectic temperature. The grain size of the alloys decreased with the increasing of zinc content and the MgZn intermetallic phase was formed by the addition of 3 wt.% Zn [10,16,17,23]. Zinc element enriches along grain boundaries to display a network microstructure for both T4 and T6-treated alloy. The grain refinement effect of a solid solute element can also be determined by calculating the grain growth limiting factor (GRF). Zn element has a higher GRF than the Al (4.32) and Y (1.70) GRF values of 5.31 GRF, has a growth-limiting effect, which means that Zn has more efficient growth restriction and better grain refinement efficiency [15].
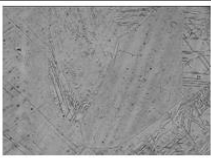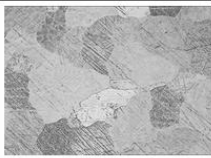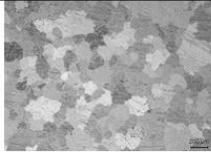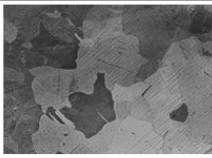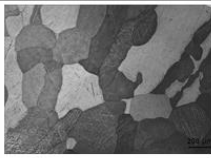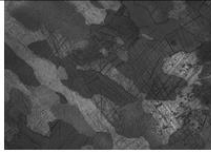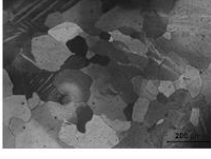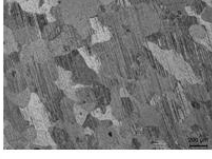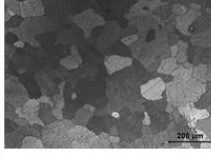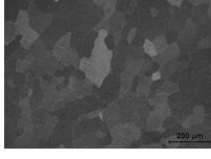
Fig 1. Optical microstructures of the alloys

In Fig. 2, hardness test results showed that hardness values of magnesium-zinc alloys increased with increasing of Zn content both as-cast and after heat treatments. The improvement of the hardness with the increasing of zinc additions can be explained by the grain refinement. Due to the solidification conditions for the as-cast samples, internal stresses are likely to be inevitable and this may also have caused the hardness to increase. After heat treatment, it is expected that the internal stresses cause relaxation and the hardness of the heat treated samples decreased. Although the grain structures decreased after 8 and 16 hours heat treatment, it was concluded that the Mg-Zn equilibrium diagram in the alloys containing 1 wt.% and 2 wt.% Zn was insufficient to form the hardening.
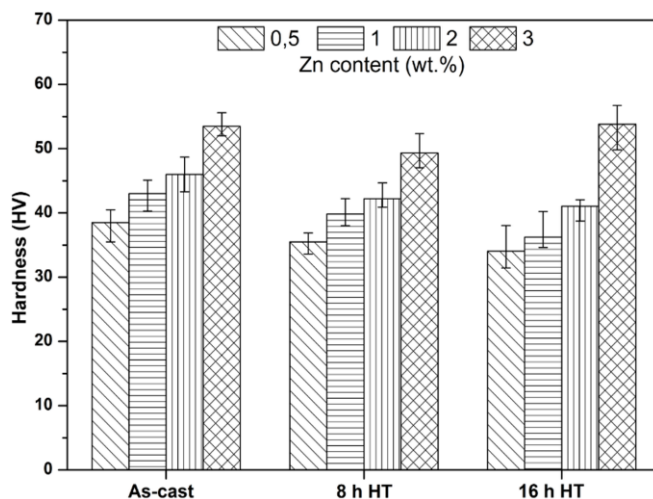
Fig. 2. Hardness values of the alloys

3.2. Electrochemical Corrosion Test

Macrographs, potentiodynamic polarization curves and the electrochemical data obtained from the polarization curves of the as cast and heat-treated samples after electrochemical corrosion tests are given in Fig.3, Fig.4 and Table 2, respectively. Macrographs of the samples after electrochemical corrosion tests are shown that in the as cast samples as the amount of Zn increases, the pits appearing on the surface increased. It can be observed that the pits on the surface of the samples after both 8 hours and 16 hours heat treatments decreased comparing with the as cast samples and thus it might be concluded that the corrosion resistance improved. As a result of the potentiodynamic polarization tests, the corrosion rate decreases as the Zn ratio increases.
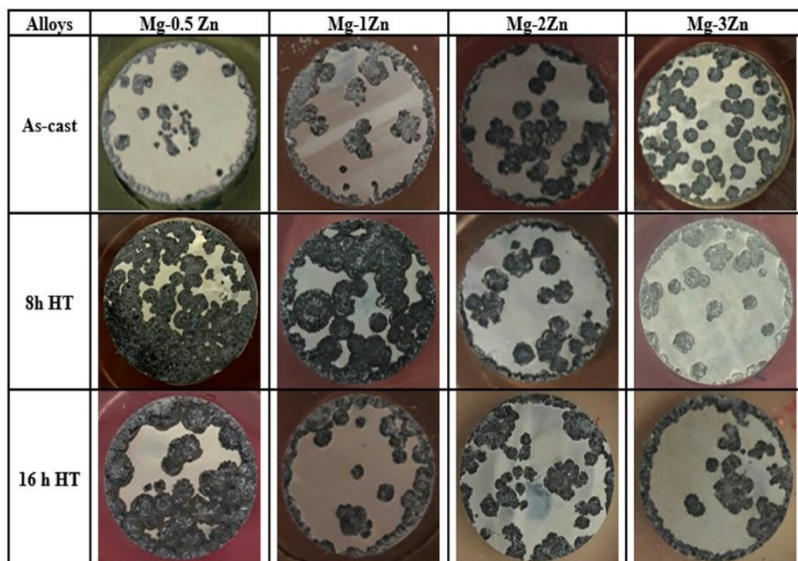
Fig. 3. Macro photographs of the corroded samples after electrochemical test.

The potentiodynamic polarization curves of as cast alloys are shown in Fig. 4. As can be seen, as the amount of Zn increases, corrosion potential (E_{corr}) value of Mg-0.5Zn is more

negative (-1.7 V) than E_{corr} value of Mg-3Zn (-1.65 V) while corrosion current density value (I_{corr}) increased from 18 µA/cm^2 in Mg-0.5Zn to 45 µA/cm^2 in Mg-3Zn. Corrosion rate (P_i) incrased from 0.41 mm/yr in Mg-0.5Zn to 1.03 mm/yr in Mg-3Zn. As the amount of Zn increased, I_{corr} and P_i increased at around 2.5 fold, in other words, the corrosion resistant decreases as the Zn ratio increases. Corrosion rate of the as-cast Mg-Zn alloys following: Mg-3Zn > Mg-2Zn > Mg-1Zn > Mg-0.5Zn. The secondary phases such as MgZn act as a micro-cathodic sites which induced to the localized corrosion in Mg-3Zn alloy [10]. However, Mg-3Zn alloy which contained high relatively high volume fraction of secondary phase particles shows improvement in the general and localized corrosion resistance [16,17]. As corrosion resistance increased with the addition of Zn in SBF solution under as-cast conditions [16,17], the corrosion resistance decreased in this study. This difference may be due to the solution used in that studies. On the other hand, there are both as low as 0.8% NaCl in SBF and different chemicals (such as $MgCl_2$, KCl, $CaCl_2$). Therefore, it is also necessary to consider the tendency of these chemicals to form a barrier on the surface during corrosion.
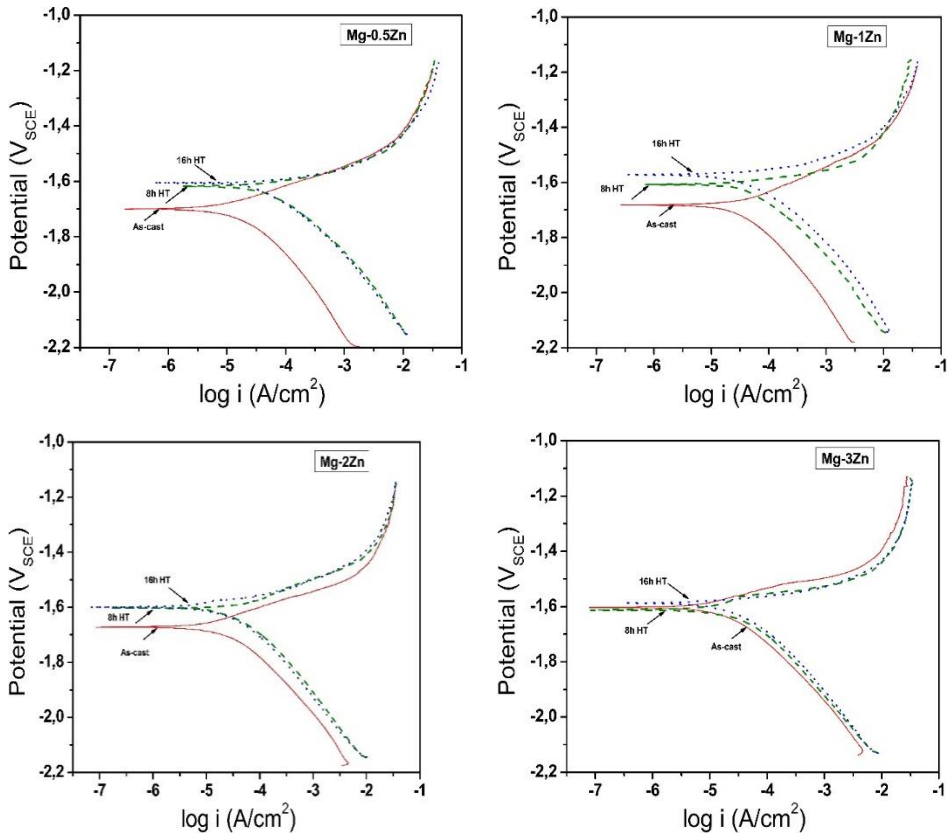
Fig. 4. Potentiodynamic polarization curves of the as cast and heat treated Mg-Zn alloys

In Fig. 4, polarization curves showed that as the amount of Zn increases, I_{corr} values decreased from 58 $\mu A/cm^2$ in Mg-0.5Zn to 28 $\mu A/cm^2$ in Mg-3Zn after 8 hours heat treatment and decreased from 45 $\mu A/cm^2$ in Mg-0.5Zn to 29 $\mu A/cm^2$ in Mg-3Zn after 16 hours heat treatment. Corrosion rate decrased from 1.33 mm/yr in Mg-0.5Zn to 0.64 mm/yr in Mg-3Zn after 8 hours heat treatment and decrased from 1.03 mm/yr in Mg-0.5Zn to 0.66 mm/yr in Mg-3Zn after 16 hours heat treatment. As the amount of Zn increased, I_{corr} and P_i values decreased by 50% and 35% after 8 hours and 16 hours of heat treatment respectively.

It can also be suggested that in the galvanic couple of Mg-3Zn, α-Mg matrix phase behaves as an anode and MgZn intermetallic phase behaves as a cathode. Therefore, after heat treatment (8 hours and 16 hours) corrosion rate of the as-cast Mg-Zn alloys following: Mg-0.5Zn > Mg-1Zn > Mg-2Zn > Mg-3Zn.

Table 2. Electrochemical data obtained from potentiodynamic polarization curves of as cast and heat treated Mg-Zn alloys.

	Alloys	E_{corr} ($V_{Ag/AgCl}$)	I_{corr} ($\mu A/cm^2$)	P_i (mm/yr)
As-cast	Mg-0.5Zn	- 1.70	18	0.41
	Mg-1.0Zn	- 1.68	33	0.76
	Mg-2.0Zn	- 1.672	40	0.93
	Mg-3.0Zn	- 1.653	45	1.03
8 hours heat treated	Mg-0.5Zn	- 1.617	58	1.33
	Mg-1.0Zn	- 1.607	56	1.29
	Mg-2.0Zn	- 1.602	39	0.91
	Mg-3.0Zn	- 1.612	28	0.64
16 hours heat treated	Mg-0.5Zn	- 1.604	45	1.03
	Mg-1.0Zn	- 1.572	38	0.88
	Mg-2.0Zn	- 1.60	32	0.75
	Mg-3.0Zn	- 1.586	29	0.66

4. Conclusions

- Microstructure studies showed that the grain size decreased with the increase of Zn content and the MgZn intermetallic phase was formed by the addition of 3 wt. % Zn. The grain boundaries are larger before heat treatment and grain structures are finer after heat treatment.

- Hardness test results showed that an increase of hardness by 36% was observed with increase of Zn content for the as-cast samples. The improvement of the hardness with the increasing of zinc additions can be explained by the grain refinement. Due to the solidification conditions for the as-cast samples, internal stresses are likely to be inevitable and this may also have caused the hardness to increase. The increase in hardness value of the samples subjected to 8 hours of heat treatment was 39%, while the values of 16 hours of heat treated samples increased to 58%. After heat treatment, it is expected that the internal stresses cause relaxation and the hardness of the heat treated samples decreased.

- For the as-cast samples, as the amount of Zn increased, I_{corr} and P_i increased at around 5.7 fold, in other words, the corrosion resistant decreases as the Zn ratio increases.

- As the amount of Zn increased, I_{corr} and P_i values decreased by 50% and 35% after 8 hours and 16 hours of heat treatment respectively. In other words, the corrosion resistant increases as the Zn ratio increases both after 8 hours heat treated and 16 hours heat treated samples. It can be suggested that in the galvanic couple of Mg-3Zn, α-Mg matrix phase behaves as an anode and MgZn intermetallic phase behaves as a cathode.

References

[1] Eliezer D, Aghion E and Froes FH. Magnesium science, technology and applications. Advanced Performance Materials, 1998; 5 (3): 201 – 212. https://doi.org/10.1023/A:1008682415141

[2] Friedrich H and Schumann S, Research for a new age of magnesium in the automotive industry. Journal of Materials Processing Technology, 2001; 117: 276 – 281. https://doi.org/10.1016/S0924-0136(01)00780-4

[3] Agnew S.R. Wrought magnesium: a 21st century Outlook. The Journal of the Minerals, Metals & Materials Society, 2004; 56 (5): 20 – 21. https://doi.org/10.1007/s11837-004-0120-8

[4] Gaines L. Cuenca R. Stodolsky F. and Wu S. Potential automotive uses of wrought magnesium alloys. Automotive Technology Development, Detroit, Michigan, 1996; 1 – 7. https://doi.org/10.2172/425305

[5] Housh S. Mikucki B and Stevenson A. Selection and application of magnesium and magnesium alloys. ASM Handbook 10th Edition, 1998; 2: 455 – 479.

[6] Bakhsheshi-Rad HR, Hamzah E, Medraj M, Idris MH, Lotfabadi AF, Daroonparvar M and Yajid MAM. Effect of heat treatment on the microstructure and corrosion behaviour of Mg–Zn alloys. Materials and Corrosion, 2014; 65(10): 999 – 1006. https://doi.org/10.1002/maco.201307492

[7] Song GL, Atrens A, St.john D, Nairn J and Li, Y. The electrochemical corrosion of pure magnesium in 1 N NaCl. Corrosion Science, 1997; 39: 855 – 875. https://doi.org/10.1016/S0010-938X(96)00172-2

[8] Zhang T, Li Y and Wang F. Roles of β phase in the corrosion process of AZ91D magnesium alloy. Corrosion Science, 2006;48: 1249 – 1264. https://doi.org/10.1016/j.corsci.2005.05.011

[9] Lee YC, Dahle AK and StJohn SH. The role of solute in grain refinement of magnesium. Metallurgical Materials Transactions A, 2000; 31(11): 2895 – 2906. https://doi.org/10.1007/BF02830349

[10] Xian-bin L, Da-yong S, Ying-wei S and En-hou H. Effects of heat treatment on corrosion behaviors of Mg-3Zn magnesium alloy. Transactions of Nonferrous Metals Society of China, 2010; 20: 1345 – 1350. https://doi.org/10.1016/S1003-6326(09)60302-2

[11] Peng LM, Chang JW, Guo, XW, Atrens A, Ding WJ and Peng YH. Influence of heat treatment microstructure on the corrosion of magnesium alloy Mg-10Gd-3Y-0.4Zr. Journal of Applied Electrochemistry, 2009; 39: 913 – 920. https://doi.org/10.1007/s10800-008-9739-4

[12] Chang JW, Guo XW, Fu PH, Peng LM and Ding WJ. Effect of heat treatment on corrosion electrochemical behaviour of Mg–3Nd–0.2Zn–0.4Zr (wt.%) alloy. Electrochimica Acta 2007; 52(9): 3160 – 3167. https://doi.org/10.1016/j.electacta.2006.09.069

[13] Jiarun L, Quantong J, Huyuan S and Yantao L. Effect of heat treatment on corrosion behavior of AZ63 magnesium alloy in 3.5 wt.% sodium chloride solution. Corrosion Science, 2016; 111: 288 – 301. https://doi.org/10.1016/j.corsci.2016.05.019

[14] Aung NN and Zhou W. Effect of heat treatment on corrosion and electrochemical behaviour of AZ91D magnesium alloy. Journal of Applied Electrochemistry, 2002; 32: 1397 – 1401. https://doi.org/10.1023/A:1022698916817

[15] Cai S, Lei T, Li N and Feng F. Effects of Zn on microstructure, mechanical properties and corrosion behavior of Mg–Zn alloys. Materials Science and Engineering: C, 2012; 32(8): 2570 – 2577. https://doi.org/10.1016/j.msec.2012.07.042

[16] Koç E, Kannan MB, Ünal M and Candan E. Influence of zinc on the microstructure, mechanical properties and in vitro corrosion behavior of magnesium-zinc binary alloys. Journal of Alloys and Compounds, 2015; 648: 291 – 296. https://doi.org/10.1016/j.jallcom.2015.06.227

[17] Koç E.. An investigation on corrosion dependent mechanical behaviours of biodegradable magnesium alloys. Ph.D. Thesis. Karabuk University, Karabuk, Turkey, 2013.

[18] Staiger MP, Pietak AM, Huadmai J and Dias G. Magnesium and its alloys as orthopedic biomaterials-A review. Biomaterials, 2006; 27(9): 1728 – 1734. https://doi.org/10.1016/j.biomaterials.2005.10.003

[19] Seal CK, Vince K and Hodgson MA. Biodegradable surgical implants based on magnesium alloys A review of current research. Materials Science Engineering, 2009; 4: 1 – 5.

[20] Schwam D, Wallace JF, Zhu Y, Viswanathan S and Iskander S. Enhancements in magnesium die casting impact properties. Final Report, Case Western Reserve University, Ohio, 2000; 5 – 22. https://doi.org/10.2172/803212

[21] Massalski TB, Okamoto H, Subramanian PR and Kacprzak L. Binary alloy phase diagrams [M]. The Materials Information Society, ASM International, 2nd Edition, 1990.

[22] Shi Z, Liu M and Atrens A. Measurement of the corrosion rate of magnesium alloys using Tafel extrapolation. Corrosion Science, 2010; 52: 579 – 588. https://doi.org/10.1016/j.corsci.2009.10.016

[23] Makhlof, FMS., Effect of zinc additions and heat treatment on the microstructure and corrosion properties of the magnesium zinc alloys. M.Sc. Thesis. Karabuk University, Karabuk, Turkey, 2018.

Research Article

Evaluation of low-velocity impact behavior of epoxy nanocomposite laminates modified with SiO₂ nanoparticles at cryogenic temperatures

Ahmet C. Tatar[a,1], Halil B. Kaybal[b,2], Hasan Ulus[*,c,1], Okan Demir[d,1] and Ahmet Avcı[e,3]

[1]*Department of Mechanical Engineering, Konya Technical University, Konya, Turkey*
[2]*Department of Mechanical Engineering, Amasya University, Amasya, Turkey*
[3]*Department of Biomedical Engineering, Necmettin Erbakan University, Konya, Turkey*

Article Info	Abstract
	Epoxy based fiber reinforced composites are widely utilized in aerospace applications due to mechanical properties, thermal stability and, chemical resistance. However, it is known that materials become brittle and due to the poor crack resist restricts their applications in cryogenic engineering applications. The purpose of this paper is to experimentally investigate the cryogenic temperatures' effect on the low-velocity impact (LVI) test of composite laminates. In addition, the effect of matrix modification in the studied composites was investigated. The LVI tests were conducted at RT (room temperature), 0 °C, -50 °C, -150 °C and -196 °C (liquid nitrogen temperature) on the composite laminates to measure influence on their energy absorption capacity. LVI tests performed according to ASTM-D-7136 standard under 10, 20 and 30 J impact energy levels. The results show that the contact forces and energy absorption capacities are improved by adding SiO₂ nanoparticles into the epoxy matrix. The absorbed energy at cryogenic temperatures is increased by 24.87% from 18.1 J of pure epoxy resin to 22.7 J of modified epoxy. For the purpose of comparison, the LVI properties of composites at room temperature (RT) are also investigated. It is noted that the energy absorption capacity is not higher at cryogenic temperatures than that at RT for the modified and neat epoxy composites. Moreover, the peak contact forces are reduced in low-temperature conditions.

1. Introduction

With the progress in science and technology, the use of polymer composites has become increasingly widespread for both scientific research and engineering applications [1]. Especially, glass and carbon fiber/epoxy composites are increasingly demanding for structural applications in aerospace, automotive and marine industries due to their excellent mechanical performance and design advantages over conventional materials [2]. At the same time, the dynamic behavior of composites under impact loading is one of the major concerns in the use of the industry as it is highly susceptible to impact loads which cause significant damage such as cracking of the matrix, delamination, and breakage of the fibers [3].

Fiber composites have the potential for extensive use in space applications, such as solar arrays, antennas, optical platforms and supports for cryogenic tanks [4]. However, the composites utilization and material selection for low-temperature applications are often

obstructed by the inconsistency of material properties of its components [5]. Because thermal contractions of fiber and matrix due to the cool conditions on the composite structure the give rise to thermal residual stresses and strains which influence most of the mechanical properties. The general of used matrices are brittle and do not allow the release of residual stresses at low temperatures [6] and the toughness degradation induced by low temperatures can lead to structural damages in the form of microcracks or delamination [7].

Dramatic changes in the properties of composites can occur when they are exposed to cryogenic temperatures [8]. Low-velocity impact exposures of the composite structure (such as the drop of an object or the impact to a harsh ground) are commonly encountered a situation in the industry. In order to develop such impact-resistant material to cryogenic applications, LVI behavior investigation is very important to optimize composite systems components. Some studies performed to investigate the impact properties of laminated composites at low temperature but the reports about the lowest temperature (down to – 60 °C) is scarce. Laminated composites become rigid with high stiffness at low temperatures (−50 °C to 120 °C) so as their deflections in impact tests were small [9]. Damage areas also smaller and higher perforation threshold resulted for laminates subjected to a low-velocity impact at low temperatures (−60 °C to 20 °C) condition [10]. However, comparatively little work has been done to understand the cryogenic temperatures of laminated composites. Therefore, in this work, the cryogenic behaviors of glass/epoxy composites are reported in terms of the LVI impact properties.

2. The Effect of Factors on Shear Force

In this study, the low-velocity impact (LVI) behaviors of glass/epoxy nanocomposite laminates were investigated using a drop weight impact test. Having been used for LVI tests, neat and nano SiO_2 (silica) added glass/epoxy laminates were produced as 10 layers. The SiO_2 nanoparticles have a specific surface area of 650 m^2/g and the average primary particle diameter of 15 nm. Adding 4 wt% SiO_2 nanoparticles were preferred as nano-reinforcements according to literature survey to perform matrix modification. It is known that best mechanical properties have been determined while using 4%wt SiO_2 nanoparticle addition [11-14]. The epoxy resin system used was a bisphenol-A (DGEBA) from Momentive Hexion, Inc. Fibers were supplied from Dost Kimya Company in Istanbul, respectively. The SEM images of the used nano SiO_2 powder is given in Fig. 1.a and it is seen that the nanoparticles form agglomeration due to attractive forces (van der Waals and others). However, it is important to avoid this situation during production because these agglomerations will cause many defects and stress concentrations in laminates [15]. SEM image of the nanoparticle distribution of 4 wt% is presented in Fig. 1.b The SiO_2 nanoparticles are seen mostly dispersed uniformly. The LVI tests were repeated three times under 10, 20, 30 Joule (J) impact energy levels and at the RT, 0 °C, -50 °C, -150 °C temperatures. In order to reach cryogenic temperature, the composite specimens were immersed in liquid nitrogen and bargain for 10 min to reach the liquid nitrogen temperature [16]. Details of experimental procedures are available in our previous studies [17-21].
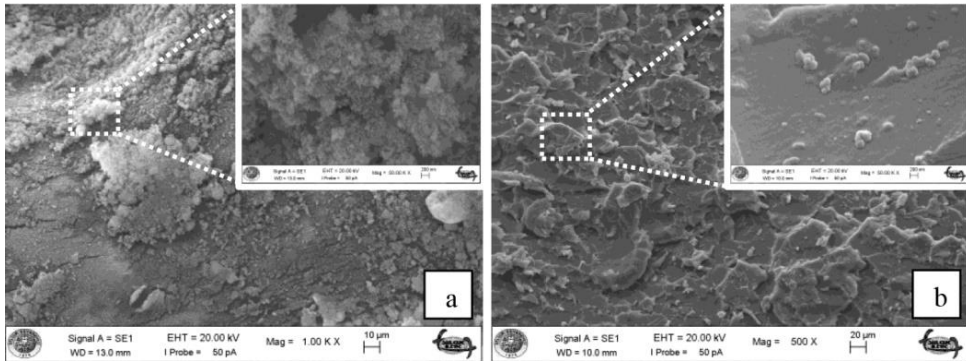
Fig. 1 a) SEM images of used nano-SiO2 powders, b) Homogeneous distribution of 4 wt% SiO2 nanoparticles in epoxy

4. Results and Discussions

Fig. 2 compares the contact force-time and force-displacement curves of the neat composite specimens with the different impact energy levels. The results show that the contact force increases significantly with the decrease of the temperatures. Meanwhile, we also compared the displacements of different temperatures in Fig. 2. It can be seen that the displacements at liquid nitrogen temperature are reduced significantly than that of at RT. Here, diminish of displacement values occur relate to the decreasing contact duration at low temperatures than that at RT. This behavior can attributed to a reduction of ductility and increase of the rigidity in laminate.

The characteristic impact parameters: peak contact force and absorbed energy for composite laminate are presented in Table 1. The peak contact force at liquid nitrogen temperature is the highest for all impact energy levels. Under the 10 J impact energy, comparing at RT to 0 °C, -50 °C, -150 °C and -196 °C the energy absorption capacity are decreased by 0.3%, 13.46%, 17.53% and 25.74% respectively. On the other hand, under the impact energy of 30 J comparing at room temperature, energy absorption capacity are decreased by 23.68%, 27.09%, 28.81% and 30.42% respectively. These results show that low velocity impact behaviors of the composite materials affected between cryogenic and room temperatures. Also clearly seen, the absorbed energy decreases with the decreasing temperature for all impact energy levels. Laminated composites exhibit relatively ductile behaviors at room temperature compared to that cryogenic temperatures because of the epoxy resins' show obviously brittle behaviors at cryogenic temperature for all compositions [22, 23]. Components of composites can create significant thermal mismatch and internal stress at low temperature applications. The internal stress within composites can greatly affect the mechanical performance by creating micro-cracks and voids [23]. On the other hand, the formed hydrogen bonds in the epoxy become stronger at cryogenic temperatures due to the shorter chemical-bond length. Free volumes in the composites would be reduced at cryogenic temperatures due to thermal shrinkage and it promotes to a higher intermolecular force then also leads to enhanced strength compared to the RT [24].
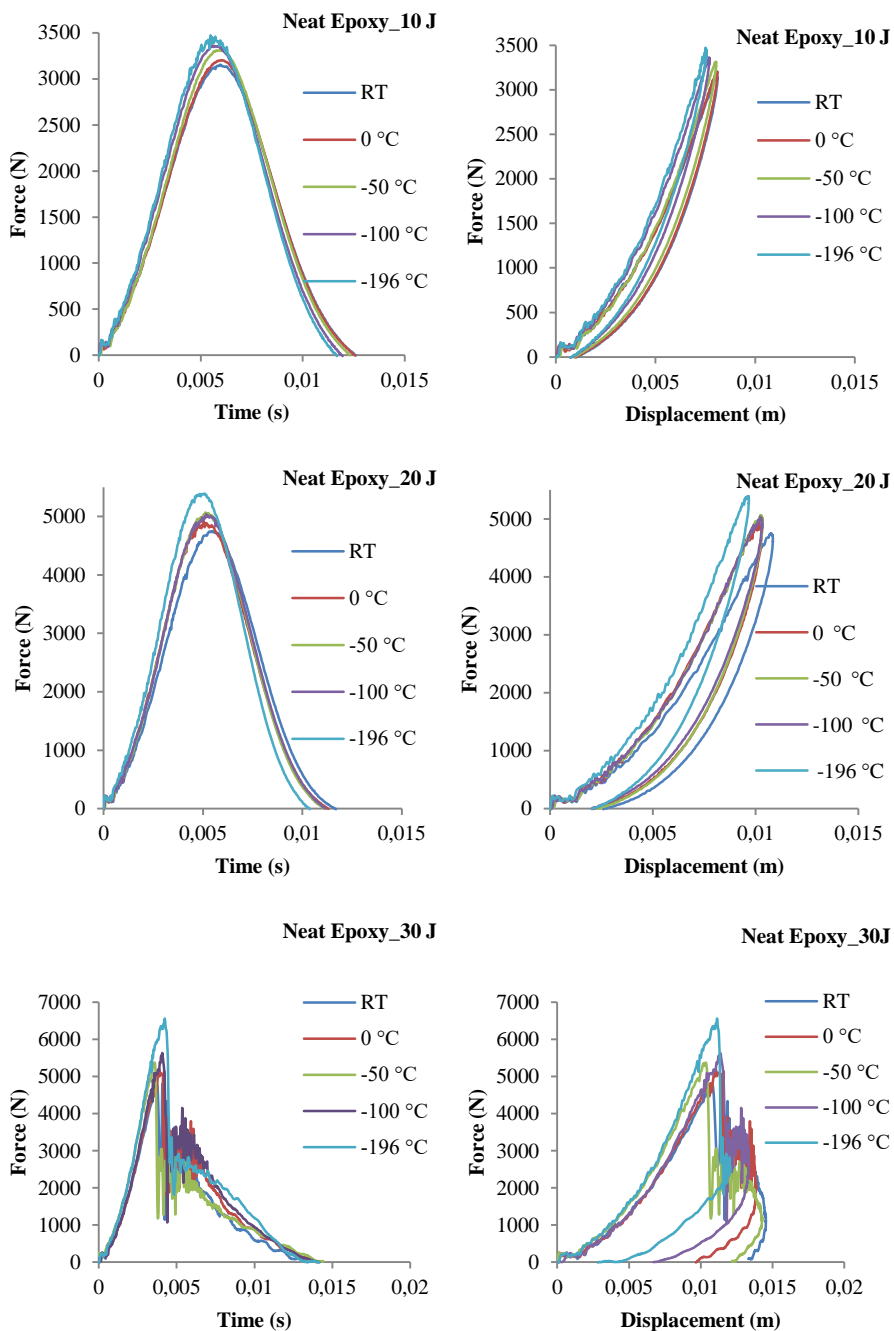
Fig. 2 Force-time and force-displacement curves at different impact energy levels

Fig. 3 shows the force-time and force-displacement histories of neat and 4 wt% nano SiO₂ reinforced for different energy levels. In the graphs, no significant change was observed with the addition of SiO₂ nanoparticles for 10 and 20- joule energy levels while average

contact force value increased significantly depending on the addition of SiO_2 nanoparticles for 30-joule energy level.
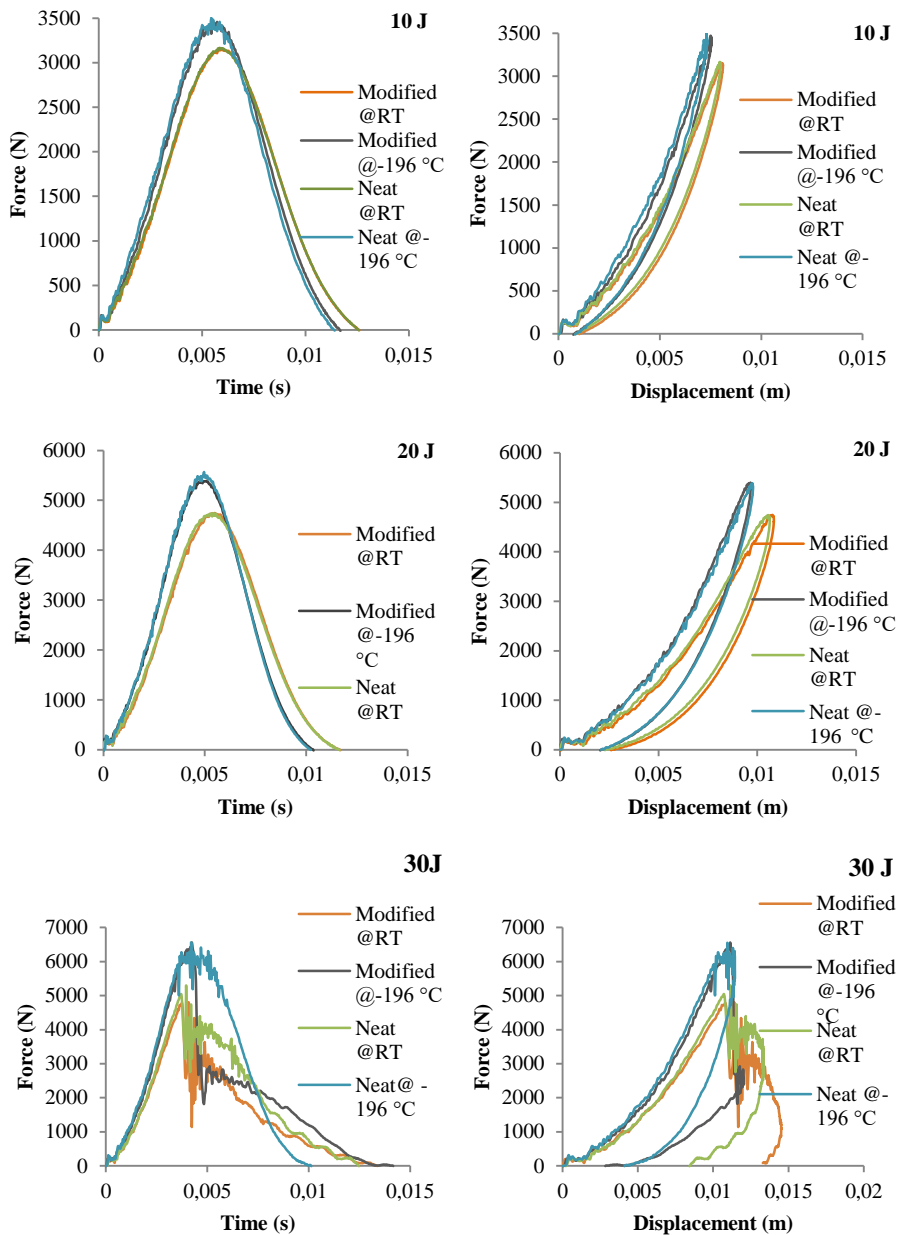
Fig. 3 Force-time and force-displacement curves of neat and modified composites at different impact energy levels

The change in the impact properties of the nanoparticle-added specimens is given in table 2. It is seen that peak forces are not affected much by the temperature under the low impact energy while it affected depending on temperature. The ratio of percentage change

of peak contact force under the 30-joule energy level are observed 13% and 24.8% for SiO_2 nanoparticle added composites, respectively.

Nano reinforcements have been extensively used to develop of the fracture toughness of matrix material and restrict of crack propagation. Therefore, to increase the mechanical performance of composite materials, researchers have been carried out to modify the matrix materials by SiO_2 nanoparticle. Many advantages of SiO_2 nanoparticles have been reported in literature to improve fracture toughness [25]. Especially, for the tests which under the 30 j impact energy level, the laminates absorbed energy is drastically increased than that of the neat epoxy matrix. This is because the laminates weren't severe destruct under the impact energy levels of 10 and 20-joule. However, it is understood that SiO_2 nanoparticles activate the toughening mechanisms for 30-joule energy levels effectively.

For the sample with the 4 wt% SiO_2 content, the specimens' absorbed energy and peak contact forces have slightly higher than that of the neat matrix. This is because the improvement of nanocomposites strongly depends on the toughening mechanisms of SiO_2 nanoparticles. When the probable crack in the matrix encounter with SiO_2 nanoparticles, it can be pinned/branched/deflected shown as in Fig. 4. The paths of crack propagation into matrix causes more fracture energy absorption. Moreover, microcracks formations in epoxy matrix are observed in Fig. 4. The microcracks formation and its propagation are also important factor for increasing fracture energy [14].
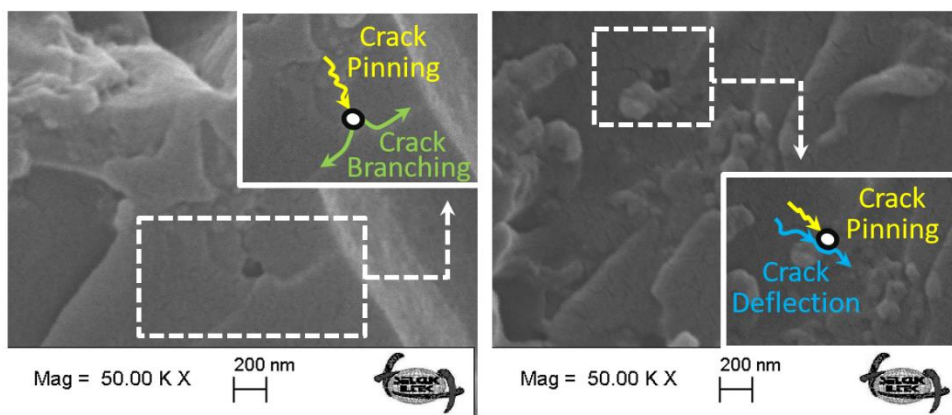
Fig. 4 Toughening mechanisms of SiO_2 nanoparticles

The cross-sectional view of LVI exposed samples at the damage site is given in Fig. 5. In the tests performed at room temperature, it is clear that the neat matrix samples failure is seen developed by delamination (shown by yellow dashed lines). In contrary less delamination is observed in the modified matrix samples, while the damage is predominantly seen as a fiber break (shown by red dashed lines). This is a clear indication that the interlaminar strength increases due to matrix modification. Moreover, in high magnification observations, a significant roughness is noticed on the fiber surfaces of modified matrix composites. This increase in fibers' roughness is evidence that fiber-matrix interface adhesion has been developed and the modified matrix supports the reduction of delamination in samples [26]. Reduction of the residual deflection which performed tests under cryogenic temperatures occurs primarily due to the show low ductility of the materials under cryogenic temperatures [11]. Similarly, nanoparticles modified composites show fewer delamination damages and better fiber-matrix interface adhesion.

Table 1 LVI properties of 10, 20 and 30 J impacted composites at RT, 0 °C, -50 °C, -150 °C and -196 °C.

Impact Energy	Temperature Condition	Peak Contact Force (N)	%↑	Absorbed Energy (J)	%↓
	RT	3143		2,95	
	-50 °C	3198	1,75	2,94	-0,34
10 J	-100 °C	3334	6,08	2,6	-13,46
	-150 °C	3375	7,38	2,51	-17,53
	-196 °C	3452	9,83	2,35	-25,74
	RT	4700		9,27	
	-50 °C	4885	3,93	9,26	-0,10
20 J	-100 °C	4971	5,76	8,71	-6,04
	-150 °C	5043	7,29	8,1	-12,62
	-196 °C	5381	14,48	7,9	-14,77
	RT	4980		26,13	
	-50 °C	5185	4,12	19,94	-23,68
30 J	-100 °C	5359	7,61	19,05	-27,09
	-150 °C	5635	13,15	18,6	-28,81
	-196 °C	6357	27,65	18,18	-30,42

Table 2 LVI properties of 10, 20 and 30 J impacted composites at different temperatures

Temperature (°C)	Neat Force (N)	SiO₂ Force (N)	Change (%)	Neat Energy (J)	SiO₂ Energy (J)	Change (%)
			10 Joule			
RT	3143	3159	0,51	2,93	2,95	0,68
-196 °C	3452	3502	1,45	2,35	2,56	0,94
	9,83%	10,86%		-19,80%	-13,22%	
			20 Joule			
RT	4700	4756	1,19	9,08	9,27	2,05
-196 °C	5381	5566	3,44	7,85	7,94	1,14
	14,49%	17,03%		-13,54%	-12,56%	
			30 Joule			
RT	4980	5295	6,33	26,13	29,54	13,05
-196 °C	6257	6741	7,71	18,18	22,7	24,86
	25,64%	27,30%		-30,42%	-23,16%	
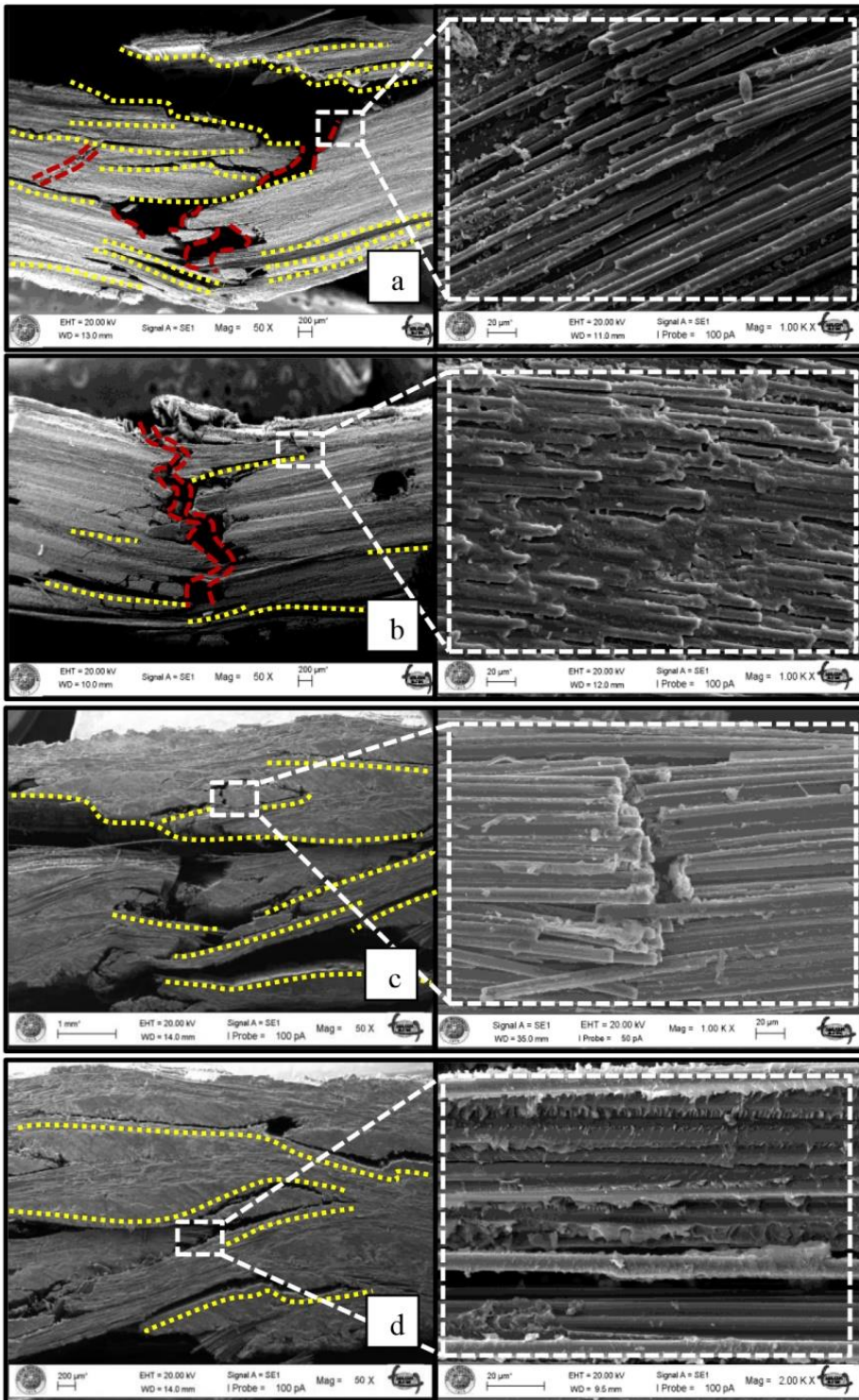
Fig. 5. Cross-sectional SEM images of impacted area: a) neat epoxy matrix_RT, b) modified epoxy matrix_RT, c) neat epoxy matrix_-196 °C, d) modified matrix_-196 °C

5. Conclusions

In this study; low-velocity impact responses of glass fiber reinforced neat epoxy composite and 4% (wt) SiO_2 modified epoxy composite laminates were investigated at different temperatures. From the results, the following conclusions can be drawn:

- It is clear that nanoparticle addition has an effect on slightly higher energy levels as opposed to low energy levels. The absorbed energy of 4%wt SiO_2 nanoparticles reinforced and neat epoxy composites for 30 J impact energy have been found an average value of 22.7 J and an average value of 18.1 J respectively for cryogenic temperature tests. SiO_2 nanoparticle addition into the epoxy matrix has provided increment by 24.8% for the absorbed energy. Besides, peak contact forces for 4%wt SiO_2 nanoparticle reinforced and neat composites, have been obtained an average of 6741 N and an average value of 6257 N respectively. Small energy absorptions were showed under cryogenic temperatures.
- It has been considered that toughening mechanisms (deflection of cracks, crack pinning and crack branching) causes enhance absorption capacities with energy dissipation. The toughness mechanisms have been observed in SEM images. The more delamination failures have also been observed on the impacted cross-sections of neat epoxy composites than SiO_2 nanoparticle reinforced specimens.
- This study revealed that cryogenic temperatures influence LVI responses of epoxy based glass fiber composites. The influence of the matrix modification by adding SiO_2 on the low-temperature behavior of composites was also investigated. Experimental results showed that the cryogenic temperatures have a direct and significant impact on the LVI behaviors. Therefore, we report that evaluate service conditions is needed especially in low-temperature applications.

Acknowledgments

References

[1] Kagitci, Y.C. and N. Tarakcioglu, The effect of weld line on tensile strength in a polymer composite part. The International Journal of Advanced Manufacturing Technology, 2016. 85(5-8): p. 1125-1135. https://doi.org/10.1007/s00170-015-8007-0 [2] Guermazi, N., et al., Investigations on the fabrication and the characterization of glass/epoxy, carbon/epoxy and hybrid composites used in the reinforcement and the repair of aeronautic structures. Materials & Design (1980-2015), 2014. 56: p. 714-724. https://doi.org/10.1016/j.matdes.2013.11.043

[3] El Moumen, A., et al., Dynamic properties of carbon nanotubes reinforced carbon fibers/epoxy textile composites under low velocity impact. Composites Part B: Engineering, 2017. 125: p. 1-8. https://doi.org/10.1016/j.compositesb.2017.05.065

[4] Bansemir, H. and O. Haider, Fibre composite structures for space applications—recent and future developments. Cryogenics, 1998. 38(1): p. 51-59. https://doi.org/10.1016/S0011-2275(97)00110- 0

[5] Praveen, R., et al., Hybridization of carbon–glass epoxy composites: An approach to achieve low coefficient of thermal expansion at cryogenic temperatures. Cryogenics, 2011. 51(2): p. 95-104. https://doi.org/10.1016/j.cryogenics.2010.12.003

[6] Hartwig, G. and S. Knaak, Fibre-epoxy composites at low temperatures. Cryogenics, 1984. 24(11): p. 639-647. https://doi.org/10.1016/0011-2275(84)90083-3

[7] Kim, M.-G., J.-B. Moon, and C.-G. Kim, Effect of CNT functionalization on crack resistance of a carbon/epoxy composite at a cryogenic temperature. Composites Part A: Applied Science and Manufacturing, 2012. 43(9): p. 1620-1627. https://doi.org/10.1016/j.compositesa.2012.04.001

[8] Timmerman, J.F., et al., Matrix and fiber influences on the cryogenic microcracking of carbon fiber/epoxy composites. Composites Part A: Applied Science and Manufacturing, 2002. 33(3): p. 323-329. https://doi.org/10.1016/S1359-835X(01)00126-9

[9] Salehi-Khojin, A., et al., The role of temperature on impact properties of Kevlar/fiberglass composite laminates. Composites Part B: Engineering, 2006. 37(7-8): p. 593-602. https://doi.org/10.1016/j.compositesb.2006.03.009

[10] Icten, B.M., et al., Low temperature effect on impact response of quasi-isotropic glass/epoxy laminated plates. Composite Structures, 2009. 91(3): p. 318-323. https://doi.org/10.1016/j.compstruct.2009.05.010

[11] Deng, S., L. Ye, and K. Friedrich, Fracture behaviours of epoxy nanocomposites with nano-silica at low and elevated temperatures. Journal of materials science, 2007. 42(8): p. 2766-2774. https://doi.org/10.1007/s10853-006-1420-x

[12] Phonthammachai, N., H. Chia, and C. He, One-Step Synthesis of Oval Shaped Silica/Epoxy Nanocomposite: Process, Formation Mechanism and Properties, in The Delivery of Nanoparticles. 2012, InTech. https://doi.org/10.5772/34800

[13] Sadej-Bajerlain, M., H. Gojzewski, and E. Andrzejewska, Monomer/modified nanosilica systems: photopolymerization kinetics and composite characterization. Polymer, 2011. 52(7): p. 1495-1503. https://doi.org/10.1016/j.polymer.2011.01.058

[14] Demirci, M.T., et al., Fracture toughness (Mode I) characterization of SiO2 nanoparticle filled basalt/epoxy filament wound composite ring with split-disk test method. Composites Part B: Engineering, 2017. 119: p. 114-124. https://doi.org/10.1016/j.compositesb.2017.03.045

[15] Zare, Y., Study of nanoparticles aggregation/agglomeration in polymer particulate nanocomposites by mechanical properties. Composites Part A: Applied Science and Manufacturing, 2016. 84: p. 158-164. https://doi.org/10.1016/j.compositesa.2016.01.020

[16] Kara, M., et al., Impact behavior of carbon fiber/epoxy composite tubes reinforced with multi-walled carbon nanotubes at cryogenic environment. Composites Part B: Engineering, 2018. 145: p. 145-154. https://doi.org/10.1016/j.compositesb.2018.03.027

[17] Kaybal, H.B., et al., Effects of alumina nanoparticles on dynamic impact responses of carbon fiber reinforced epoxy matrix nanocomposites. Engineering Science and Technology, an International Journal, 2018.

[18] Eskizeybek, V., et al., Static and dynamic mechanical responses of CaCO3 nanoparticle modified epoxy/carbon fiber nanocomposites. Composites Part B: Engineering, 2018. 140: p. 223-231. https://doi.org/10.1016/j.compositesb.2017.12.013

[19] Üstün, T., et al., Evaluating the effectiveness of nanofillers in filament wound carbon/epoxy multiscale composite pipes. Composites Part B: Engineering, 2016. 96: p. 1-6. https://doi.org/10.1016/j.compositesb.2016.04.031

[20] Ulus, H., et al., Low-velocity impact behavior of carbon fiber/epoxy multiscale hybrid nanocomposites reinforced with multiwalled carbon nanotubes and boron nitride nanoplates. Journal of Composite Materials, 2016. 50(6): p. 761-770. https://doi.org/10.1177/0021998315580835

[21] Ulus, H., Ö.S. Şahin, and A. Avcı, Enhancement of flexural and shear properties of carbon fiber/epoxy hybrid nanocomposites by boron nitride nano particles and carbon nano tube modification. Fibers and Polymers, 2015. 16(12): p. 2627-2635. https://doi.org/10.1007/s12221-015-5603-4

[22]Chen, Z.-K., et al., Reinforcement of epoxy resins with multi-walled carbon nanotubes for enhancing cryogenic mechanical properties. Polymer, 2009. 50(19): p. 4753-4759. https://doi.org/10.1016/j.polymer.2009.08.001

[23]Yang, G., S.-Y. Fu, and J.-P. Yang, Preparation and mechanical properties of modified epoxy resins with flexible diamines. Polymer, 2007. 48(1): p. 302-310. https://doi.org/10.1016/j.polymer.2006.11.031

[24]Yang, J.-P., et al., Simultaneous improvements in the cryogenic tensile strength, ductility and impact strength of epoxy resins by a hyperbranched polymer. Polymer, 2008. 49(13-14): p. 3168-3175. https://doi.org/10.1016/j.polymer.2008.05.008

[25]Demirci, M.T., et al., Fracture toughness (Mode I) characterization of SiO 2 nanoparticle filled basalt/epoxy filament wound composite ring with split-disk test method. Composites Part B: Engineering, 2017. 119: p. 114-124. https://doi.org/10.1016/j.compositesb.2017.03.045

[26]Eskizeybek, V., A. Avci, and A. Gülce, The Mode I interlaminar fracture toughness of chemically carbon nanotube grafted glass fabric/epoxy multi-scale composite structures. Composites Part A: Applied Science and Manufacturing, 2014. 63: p. 94-102. https://doi.org/10.1016/j.compositesa.2014.04.013

Research Article

Microstructure, hardness and biocompatibility properties of ceramic based coatings produced by plasma spray method

Serkan Islak[*,a,1], Nuray Emin[b,2], Cihan Özorak[c,3] and Husain R.H. Hraam[d,4]

[1] Department of Mechanical Engineering, Kastamonu University, Kastamonu, Turkey
[2] Department of Biomedical Engineering, Kastamonu University, Kastamonu, Turkey
[3] Department of Metallurgical and Materials Engineering, Kastamonu University, Kastamonu, Turkey
[4] Institute of Science, Kastamonu University, Kastamonu, Turkey

Article Info	Abstract
	Ceramic materials with excellent mechanical, corrosion and abrasion resistance is set in terms of features such as biomaterials. In this study, Al_2O_3, Al_2O_3-40% TiO_2, ZrO_2 - 8% Y_2O_3 and Cr_2O_3-2% TiO_2 ceramic coatings were produced by plasma spraying on AISI 316L stainless steel surface. It was aimed to investigate microstructure, hardness and biocompatibility properties of coatings. Scanning electron microscope (SEM) analysis and X-ray diffraction (XRD) phase analysis were used to determine the microstructure and phase composition properties. The biocompatibility properties of coatings have been tried to be determined by analyzing cytotoxicity and viability. The SEM images show that the ceramic coatings are connected in accordance with the substrate. The XRD analyzes show the formation of binary and ternary complex phases in the coating layers. Cr_2O_3-2% TiO_2 coating has the highest hardness in the coating layers. Biocompatibility tests reveal the most compatible and consistent results in terms of cytotoxicity were obtained with Al_2O_3-40% TiO_2 coating.

1. Introduction

Biomaterials are natural or synthetically obtainable materials which are used for prosthetic, diagnostic or therapeutic purposes and which are in contact with tissue, blood and other body fluids within the body [1, 2]. The performances of the materials used in the body are important. The performances of the materials placed inside the body can be examined from different angles. Depending on the area in which the problem is to be solved, a classification can be made at the tissue-organ level or according to the materials used [3]. Biomaterials can be used for a long time or for a short time. The most basic feature that implants should provide is that they are not allergenic or toxic. In addition, biomaterials, designs and mechanical behavior are important qualities. Ceramics are usually blends of metals formed by non-metallic elements. The interatomic bond is ionic or covalent. Ceramic materials have been used as medical materials for many years despite their fragility, porous structure, low tensile strength and low impact strength. With the recent development of new methods, ceramics are used in many different fields of biomolecules. They are widely used in dentistry as gold-porcelain crowns, silica–filled resin composites, and dentures. Due to its high wear resistance, high hardness and excellent corrosion resistance, Al_2O_3 and yttria–stabilized ZrO_2 are widely used in hip prostheses and dental industry with load carrying function [4, 5].

127

Plasma spraying method is spraying of powder on the surface of the material to be coated at a plasma temperature which is ionized and can reach up to 15.000 ° C-25.000 ° C, while the diatomic gases (argon-hydrogen mixture) passing between a tungsten (cathode (-)) and a copper nozzle [6-8]. Plasma spraying is effectively and economically applied to various machine parts to reduce surface defects [9]. In this method, the complete or partial melting of the powders varies depending on their thermal properties. The controllability of the system at extremely high heating and cooling rates makes it possible to produce coatings made of metallic, non-metallic and ceramics and combinations with this method [10]. Ceramic powders are used more frequently than metallic powders in the plasma spray method due to their high chemical stability at high temperatures, excellent wear resistance and corrosion resistance [11]. Ceramic materials with high resistance to corrosive and thermal conditions, relatively low density and high hardness are preferred over polymeric and metallic materials due to their existing properties. Ceramic materials such as aluminum oxide, zirconium oxide, titanium oxide, chromium oxide, silicon oxide and yttrium oxide are widely used as surface coating materials to improve wear, erosion, cavitation and corrosion resistance of materials. Such materials are particularly needed in applications where resistance to wear and corrosion is desired [12, 13].

In this study, Al_2O_3, Al_2O_3 - 40% TiO_2, ZrO_2 - 8% Y_2O_3 and Cr_2O_3 - 2% TiO_2 oxide coatings were produced by plasma spraying on AISI 316L stainless steel surface since they have high wear resistance and high corrosion resistance. Stainless steels are used in orthopedic applications. They have the ability to bear significant loads and withstand fatigue loading. Therefore, in this study, AISI 316L stainless steel was preferred as substrate. Microstructure and biocompatibility properties were experimentally investigated. Microstructure, microhardness and phase properties were determined by scanning electron microscopy (SEM), energy dispersive spectrometry (EDS) and X-ray diffractogram (XRD) analyzes. The microhardness change was measured from the top of the coating layer. The biocompatibility properties of coatings have been tried to be determined by cytotoxicity and viability analysis.

2. Materials and Methods

AISI 316L stainless steel was used as substrate and Al_2O_3 (Metco 105SFP), Al_2O_3 - 40% TiO_2 (Metco 131VF), ZrO_2 - 8% Y_2O_3 (Metco 204B-NS) and Cr_2O_3-2% TiO_2 (Metco 106F) were used as coating powders. A Sulzer Metco 9MB atmospheric plasma spray coating system with 80 kVA of power was used to produce the coating layer (Fig. 1). The flow rate of the argon gas used to produce the plasma beam in all coatings is 35-73 l/min. The plasma spray gun was fixed so that the spray distance was 75 mm, so that the coating powders were injected externally to the gun and parallel to the plasma flow. H_2 gas flow rate was 6.6 l/min and carrier gas ratio was set as 9-11.4 l/min. About 250 μm thick layer was produced as coating layer. For metallographic investigations, the samples were sanded by passing through coarse and fine sanding steps, respectively. The sanded samples were polished using diamond solutions and etched using a solution of HNO_3 (40 pct.) + C_2H_5OH (60 pct.). A FEI QUANTA 250 FEG scanning electron microscope (FEI Inc., OR, USA) was used to determine the chemical composition of the microstructure. X-ray diffraction (XRD) analysis was performed to determine the phases formed in the microstructure using a Bruker D8 Advance XRD system (Bruker Optik GmbH, Ettlingen, Germany).

The hardness measurement was made with SHIMADZU HMV-G21 brand microhardness device with a waiting period of 15 seconds from the top surface of the coating and a load of 200 gf (1.961 N). From each sample, 6 hardness measurements were taken from different regions. Their averages were taken and evaluated. Hardness tests were carried out according to ASTM C1327–15 standard [14].

The biocompatibility properties of coatings have been tried to be determined by cytotoxicity and viability analysis. The cytotoxicity tests of the prepared composite materials were performed by in vitro tests based on cell viability. For this aim, MTT [3- (4,5-dimethyldazol-2-yl) -2,5-diphenyl tetrazolium bromide] (Sigma, USA) test was used to measure cell viability and mitochondrial dehydrogenase activity. MCT3T3-E Mouse osteoblastic cells were used in the studies because of coating materials' potential to be used as a bone implant. In the tests, 6-well petri dishes were used, depending on the size of the samples. 200 µl cell suspension (containing $\sim2x10^5$ cells) was added onto each prewetted sample placed in a well of 6-well plate; kept in the incubator for 10 min and then was gently covered with basal medium. After freshly prepared 4.5 ml of medium (without FBS) was added to each well, 0.5 ml fresh MTT reagent was added to provide 10% concentration, and they were incubated at 37°C and 5% CO_2 for 4 h. However, no sample was placed in one of the wells as a control. The formazan, insoluble dark blue complex that was formed by MTT reduced in the mitochondria, was monitored under an inverted microscope (Leica DMIL LED, Germany). Semi-quantitative data were obtained spectrophotometrically at the wavelength of 570 nm using a multi-well plate reader (Biotek, USA). The MTT tests applied to the cultures were repeated three times and the mean values of the measurements were taken according to the days.
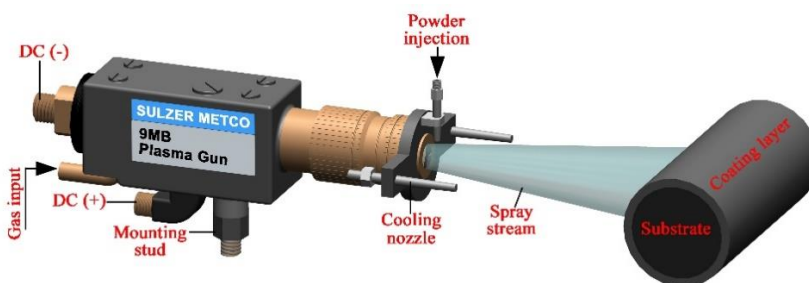
Fig. 1 Principle diagram of plasma spray coating process

3. Results and Discussion

The macro images of Al_2O_3, Al_2O_3-40% TiO_2, ZrO_2-8% Y_2O_3 and Cr_2O_3 - 2% TiO_2 ceramic based coating samples produced on AISI 316L stainless steel are given in Fig. 2. All surfaces of the samples were coated. In the samples produced, color change occurred according to the content of the coating material. It is also noted that the coating layers are smooth.

SEM images of ceramic coatings produced by plasma spray process are shown in Fig. 3. The SEM images exhibit splat by splat lamellar structure formation in all of the coatings with the presence of partially melted regions and some un-melted particles in ceramic coatings. The coating layer is connected to the bottom material as compatible. This is a positive result of the strength of the coatings against mechanical forces. The porosity in the coating layers came to fruition. Although this is negative for mechanical properties, it is considered to be favorable in terms of biocompatibility. Pore formation is inevitable in studies carried out in the literature [15, 16]. Porosity is caused by the lack of insufficient surface wetting of the melted particles striking rough substrate surface [17]. The distribution of the elements forming the coating layer in the main matrix also affects both the mechanical and physical properties. While homogeneous distribution affects the characteristics positively, heterogeneous distribution affects negatively. In order to determine the distribution of the elements, SEM-MAP analysis of the Cr_2O_3-2% TiO_2.coating given in Fig. 4 was performed. According to the analysis, the elements Ti and O were distributed relatively

homogeneously in the main element of Cr. This indicates that the features will be the same all over the coating.

Fig. 2 The macro images of ceramic based coatings
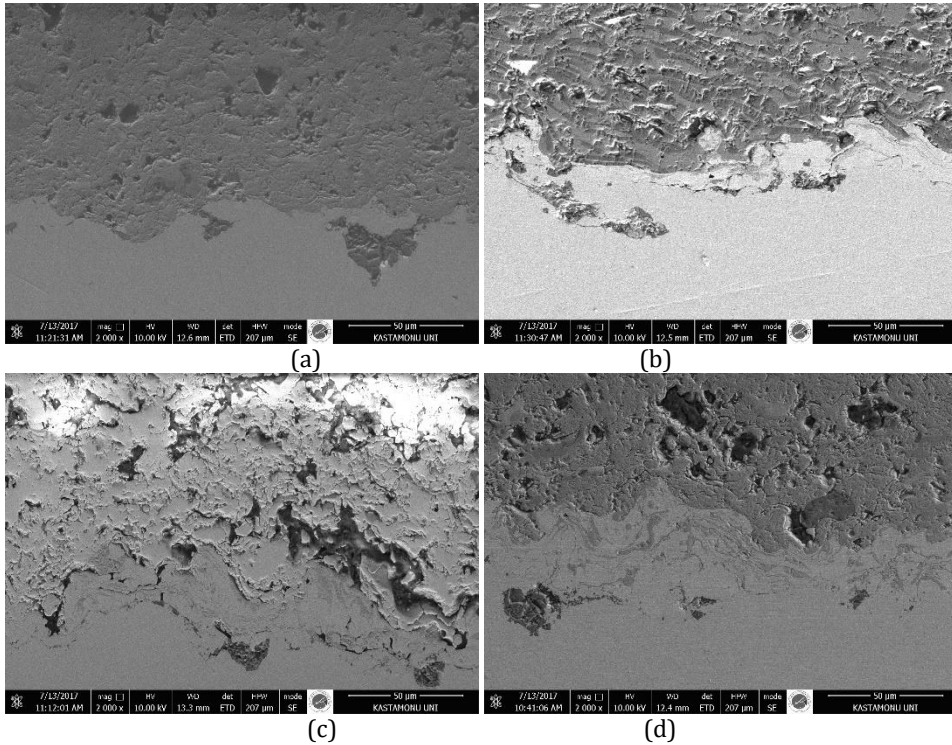
Fig. 3 (a) Al_2O_3 (b) Al_2O_3 - 40% TiO_2, (c) ZrO_2 - 8% Y_2O_3 and (d) Cr_2O_3 - 2% TiO_2.
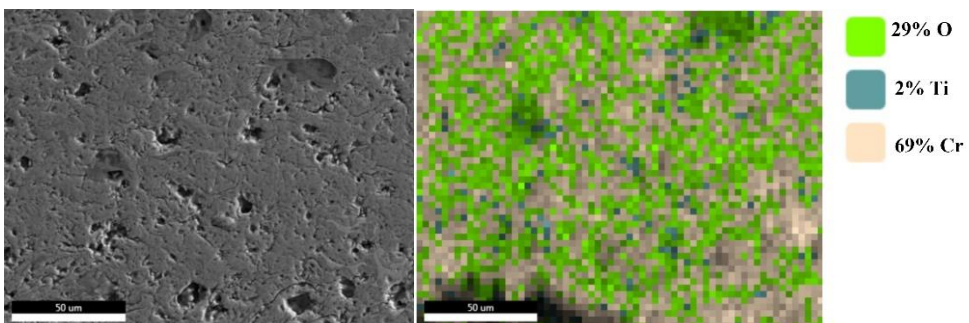
Fig.4 SEM-MAP analysis of Cr_2O_3-2%TiO_2 coating

Fig. 5 shows the XRD analyzes of the coatings. Phases seen in coatings represent powders before coating. Besides this, it is formed in ternary phases in addition to binary phases. For the Al_2O_3 coating, while the α-Al_2O_3 phase was present in the powder material, the phase γ-Al_2O_3 was detected in the coating layer. During the spraying process, the conversion from α-Al_2O_3 to γ-Al_2O_3 occurred in a crystal structure [18-20]. In the specimens coated by Al_2O_3-40%TiO_2 contents, XRD data give Al_2TiO_5, and γ-Al_2O_3-TiO_2 phases beside γ-Al_2O_3 phase. Due to very small size of the particles, the contact area among them were very large and during plasma spraying this large area caused the formation of Al_2TiO_5 reaction phase whose thermal expansion coefficient was too small and therefore it was desired for the applications where thermal resistance was needed [21-24]. For the ZrO_2 - 8% Y_2O_3 coating, tetragonal (t) ZrO_2 phase is formed in the microstructure. This phase is a metastable phase. This is an expected situation, given the work done in relation to ZrO_2-Y_2O_3 [25]. No phase other than this phase has been formed. The XRD analysis of Cr_2O_3 - 2% TiO_2 coating revealed that the strong diffraction peaks detected were related to Cr_2O_3 phase (rhombohedral crystal system). No phase related to TiO_2 was detected. 2% TiO_2 is used in the starting powder which is quite less and difficult to be detected comprehensively by XRD analysis [26, 27].
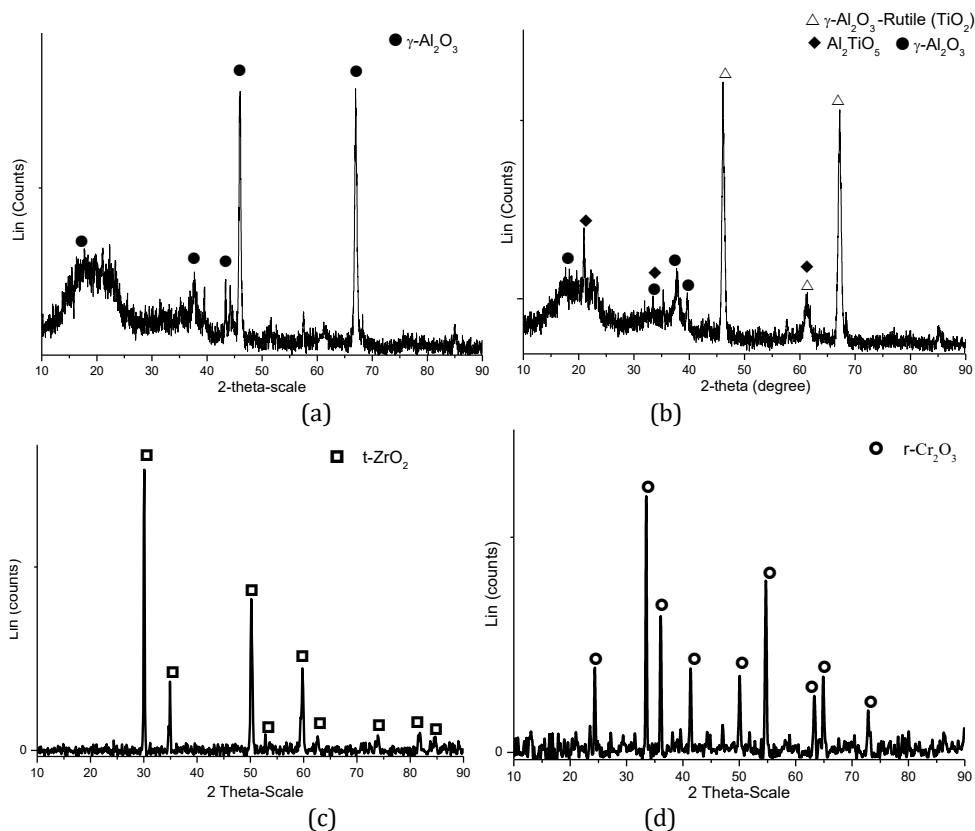
Fig. 5 XRD analyses: (a) Al_2O_3 (b) Al_2O_3 - 40% TiO_2, (c) ZrO_2 - 8% Y_2O_3 and (d) Cr_2O_3 - 2% TiO_2.

The micro hardness values of the substrate and coating layers are given in Fig. 6. Hardness values are taken from six different regions. The coating was also taken from six different regions from the layers and taken from the upper surface of the coatings. Evaluation was made by taking the average of the values received. While the hardness of the substrate is 215 $HV_{0.2}$, the hardness values of the Al_2O_3, Al_2O_3 - 40% TiO_2, ZrO_2 - 8% Y_2O_3 and Cr_2O_3 - 2% TiO_2 coating layers are 905 $HV_{0.2}$, 760 $HV_{0.2}$, 950 $HV_{0.2}$ and 1215 $HV_{0.2}$, respectively, which are 3.5-5.6 times higher than the substrate. The hardness of the Al_2O_3-40% TiO_2 coating layer was lower than the TiO_2-free Al_2O_3 coating. Al_2O_3 material is known to be harder than TiO_2 material. In the coating of Al_2O_3-40% TiO_2, TiO_2 has a toughening role [28]. Cr_2O_3 - 2% TiO_2 coating has the highest hardness value among ceramic coating layers. This measured value is compatible with the literature [26]. These increases in hardness are due to the natural hardness of the ceramic materials. During this hardness measurement, no cracks were formed in the ceramic coatings.
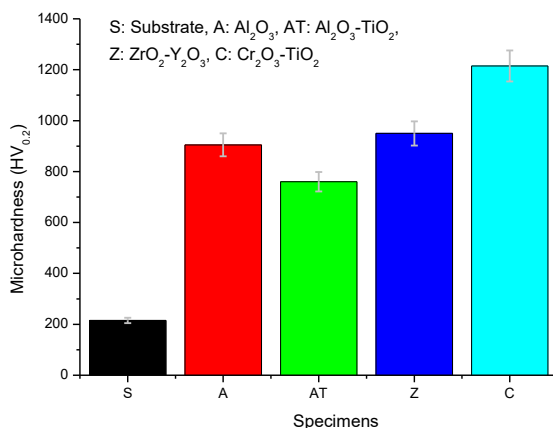
Fig. 6 Micro hardness values of the substrate and coating layers

In biocompatibility analysis, it was observed that cell viability did not change much in all ceramic coatings and the highest absorbance value was obtained on the 7th day. In addition, although it is clear that biocompatibility due to cell viability shows similar values for all coatings, the most compatible and consistent results in terms of cytotoxicity were obtained in the coating of aluminum oxide-titania. Change of absorbance values measured at 570 nm wavelength of ceramic coatings according to culture time is given in Fig. 7. According to semi-quantitative analyzes, cell viability in the alloy with the zirconium oxide coating was generally maintained in 14 days of continued cell culture, but at the 14th day a 35% reduction was determined. This change in chromoxide-titanium oxide coating was calculated as 31%, in aluminum oxide-titanium oxide coating as 24% and in aluminum oxide coating as 13%.
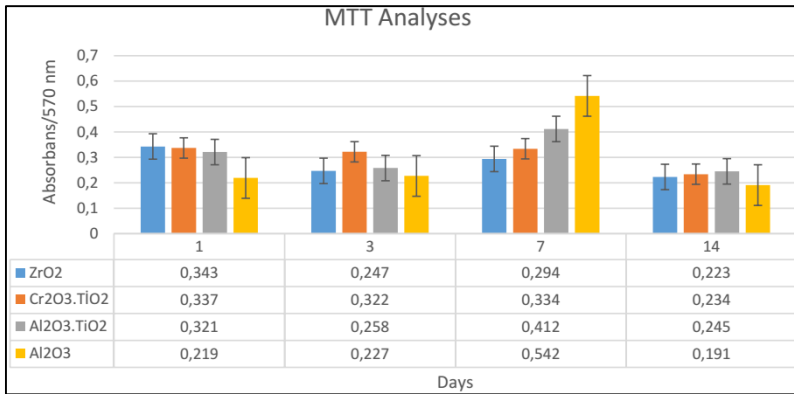
Fig. 7 Change of absorbance values measured at 570 nm wavelength of ceramic coatings according to culture time.
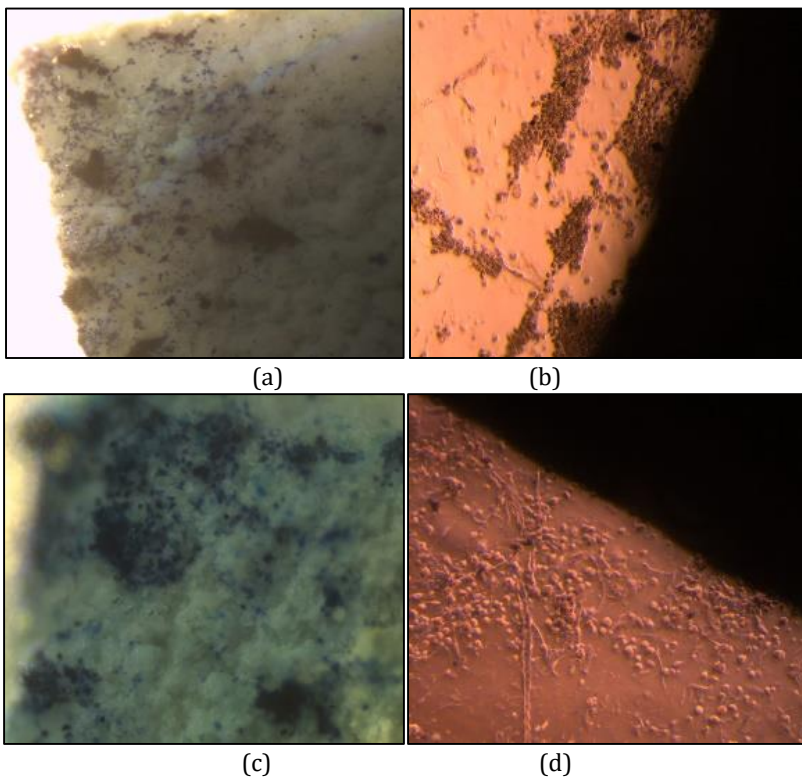
Figure 8. Formation of formazan crystals as a result of MTT analysis: (a) Al_2O_3 (b) Al_2O_3-40% TiO_2, (c) ZrO_2-8% Y_2O_3 and (d) Cr_2O_3-2% TiO_2.

Formazan crystals formed by MTT reagent reduction are shown in Fig. 8. It has been observed that formazan crystals are formed on the surface of composite structures and in micropores. In addition, because of the weak bonding with the material surfaces cells had been separated from the materials, and formazan crystals were formed in the vicinity of these scattered cells on the plate surface [29].

4. Conclusion

In this study, Al_2O_3, Al_2O_3 - 40% TiO_2, ZrO_2 - 8% Y_2O_3 and Cr_2O_3 - 2% TiO_2 oxide coatings were produced by plasma spraying on AISI 316L stainless steel surface. The conclusions drawn from this study are given below:

- The SEM images showed that the coating layers were mechanically bonded to the substrate, had a slightly porous structure, and generally the coating layers had lamella formation.
- The γ-Al_2O_3, Al_2TiO_5, γ-Al_2O_3-TiO_2, t-ZrO_2 and r-Cr_2O_3 phases were determined by the XRD analysis of the coating layers.
- The hardness of the coatings varied between 760-1215 $HV_{0.2}$ and there was a 3.5-5.6-fold increase compared to the substrate. The highest hardness was obtained in Cr_2O_3 - 2% TiO_2 coatings.
- Although it is clear that biocompatibility depends on cell viability, similar results are obtained in all coatings, but the most compatible and consistent results in terms of cytotoxicity were obtained with Al_2O_3-40% TiO_2 coating.

5. Acknowledgements

References

[1] Wong, JY, Bronzino, JD. *Biomaterials*, CRC Press, Taylor&Francis Group, LLC, 2007.
[2] Williams, DF. *Williams dictionary of biomaterials*, Liverpool University Press 1999.
[3] Lutišanová, G, Kuzielová, E, Palou, MT, Kozánková, J. Static and Dynamic In Vitro Test of Bioactivity of Glass Ceramics, Ceramics – Silikáty, 2011; 55(2): 106-113.
[4] Demirkıran, H. (2003). Biyocam Takviyeli Hidroksiapatit Kompozitlerinin Geliştirilmesi, MSc. Thesis, İTÜ Fen Bilimleri Enstitüsü, İstanbul.
[5] Lee, KY, Park, M, Kim, HM, Lim, YJ, Chun, HJ, Kim, H, Moon, SH. Ceramic bioactivity: progresses, challenges and perspectives. Biomedical materials, 2006; 1(2):R31–R37. https://doi.org/10.1088/1748-6041/1/2/R01
[6] Heimann, RB. Plasma-spray coating, VCH, New York, 1996.
[7] Pawlowski, L. The science and engineering of thermal spray coatings, John Wiley & Sons, Ltd., England. 2008.
[8] Pantelis, DI, Psyllaki, P, Alexopoulos, N. Tribological behaviour of plasma-sprayed Al2O3 coatings under severe wear conditions. Wear, 2000; 237: 197-204. https://doi.org/10.1016/S0043-1648(99)00324-5
[9] Song, EP, Ahn, J, Lee, S, Kim, NJ. Effects of critical plasma spray parameter and spray distance on wear resistance of Al_2O_3-8 wt.%TiO_2 coatings plasma-sprayed with nanopowders. Surface and Coatings Technology, 2008; 202: 3625-3632. https://doi.org/10.1016/j.surfcoat.2008.01.002
[10] Datye, A, Koneti, S, Gomes, G, Wu, KH, Lin, HT. Synthesis and characterization of aluminum oxide-boron carbide coatings by air plasma spraying. Ceramics International, 2010; 36: 1517-1522. https://doi.org/10.1016/j.ceramint.2010.02.024
[11] Wang, Y, Jiang, S, Wang, M, Wang, S, Xiao, TD, Strutt, PR. Abrasive wear characteristic of plasma sprayed nanostructured alumina/titania coatings. Wear, 2000; 237: 176–185. https://doi.org/10.1016/S0043-1648(99)00323-3
[12] Sun, Y, Li, B, Yang, D, Wang, T, Sasaki, Y, Ishii, K. Unlubricated friction and wear behaviour of zirconia ceramics. Wear, 1998; 215: 232-236. https://doi.org/10.1016/S0043-1648(97)00247-0

[13] Cadenas, M, Vijande, R, Montes, HJ, Sierra, JM. Wear behaviour of laser cladded and plasma sprayed WC–Co coatings. Wear, 1997; 212: 244-253. https://doi.org/10.1016/S0043-1648(97)00127-0

[14] ASTM C1327-15, Standard Test Method for Vickers Indentation Hardness of Advanced Ceramics, ASTM International, West Conshohocken, PA, 2015. https://doi.org/10.1520/C1327-15

[15] Daroonparvar, M, Yajid, MAM, Yusof, NM, Bakhsheshi-Rad, HR, Hamzah, E, Nazoktabar, M. Investigation of three steps of hot corrosion process in Y_2O_3 stabilized ZrO_2 coatings including nano zones. Journal of Rare Earths, 2014; 32(10):989-1002. https://doi.org/10.1016/S1002-0721(14)60173-3

[16] Krishnamurthy, N, Murali, MS, Mukunda, PG, Ramesh, MR. Characterization and wear behavior of plasma-sprayed Al_2O_3 and $ZrO_2 5CaO$ coatings on cast iron substrate. Journal of materials science, 2010; 45(3):850-858. https://doi.org/10.1007/s10853-009-4009-3

[17] Fervel, V, Normand, B, Coddet, C. Tribological behavior of plasma sprayed Al2O3-based cermet coatings. Wear, 1999; 230(1):70-77. https://doi.org/10.1016/S0043-1648(99)00096-4

[18] Rico, A, Rodriguez, J, Otero, E, Zeng, P, Rainforth, WM. Wear behaviour of nanostructured alumina–titania coatings deposited by atmospheric plasma spray. Wear, 2009; 267:1191–1197. https://doi.org/10.1016/j.wear.2009.01.022

[19] Islak, S, Buytoz, S, Ersöz, E, Orhan, N, Stokes, J, Hashmi, MS, Somunkıran, İ, Tosun, N. Effect on microstructure of TiO_2 rate in Al_2O_3-TiO_2 composite coating produced using plasma spray method. Optoelectronics and Advanced Materials – Rapid Communications, 2012; 6(9-10):844 – 849

[20] Lin, X, Zeng, Y, Lee, SW, Ding, C. Characterization of alumina–3 wt.% titania coating prepared by plasma spraying of nanostructured powders. Journal of the European Ceramic Society, 2004; 24:627-634. https://doi.org/10.1016/S0955-2219(03)00254-1

[21] Hoffmann, S, Norberg, ST, Yoshimura, M. Melt synthesis of Al_2TiO_5 containing composites and reinvestigation of the phase diagram Al_2O_3–TiO_2 by powder X-ray diffraction. Journal of Electroceramics, 2006; 16:327–330. https://doi.org/10.1007/s10832-006-9873-5

[22] Li, CJ, Yang, GJ, Ohmori, A. Relationship between particle erosion and lamellar microstructure for plasma-sprayed alumina coatings. Wear, 2006; 260:1166-1172. https://doi.org/10.1016/j.wear.2005.07.006

[23] Sundararajan, G, Sen, D, Sivakumar, G. The tribological behaviour of detonation sprayed coatings: the importance of coating process parameters. Wear, 2005; 258:377–391. https://doi.org/10.1016/j.wear.2004.03.022

[24] Tian, W, Wang, Y, Yang, Y, Li, C. Toughening and strengthening mechanism of plasma sprayed nanostructured Al_2O_3–13 wt.% TiO_2 coatings. Surface and Coatings Technology, 2009; 204(5): 642-649. https://doi.org/10.1016/j.surfcoat.2009.08.045

[25] Ouyang, JH, Sasaki, S. Microstructure and tribological characteristics of ZrO_2–Y_2O_3 ceramic coatings deposited by laser-assisted plasma hybrid spraying. Tribology International, 2002; 35(4):255-264. https://doi.org/10.1016/S0301-679X(02)00005-1

[26] Singh, VP, Sil, A, Jayaganthan, R. Tribological behavior of plasma sprayed Cr_2O_3–3% TiO_2 coatings. Wear, 2011; 272(1):149-158.https://doi.org/10.1016/j.wear.2011.08.004

[27] Wang, B, Yan, J, Cui, H, Du, S. Preparation and characterization of nano TiO_2/micron Cr_2O_3 composite particles. Journal of Alloys and Compounds, 2011; 509(15):5017-5019. https://doi.org/10.1016/j.jallcom.2011.02.008

[28] Tian, W, Wang, Y, Yang, Y. Three body abrasive wear characteristics of plasma sprayed conventional and nanostructured Al_2O_3-13% TiO_2 coatings. Tribology International, 2010; 43(5-6):876-881. https://doi.org/10.1016/j.triboint.2009.12.023

[29] Castell, JV, Gmez-Lechn, MJ. In vitro methods in pharmaceutical research. Elsevier, 1996. https://doi.org/10.1016/B978-0-12-163390-5.X5000-5

Research Article

Electrical conductivity, microstructure and wear properties of Cu-Mo coatings

Serkan Islak*, a,1, Uğur Çalıgülüb,2, Husain R.H. Hraamc,3, Cihan Özorakd,4, Vahdettin Koçe,5

1 Department of Mechanical Engineering, Kastamonu University, Kastamonu, Turkey
2 Department of Metallurgical and Materials Engineering, Fırat University, Elazığ, Turkey
3 In Institute of Science, Kastamonu University, Kastamonu, Turkey
4 Department of Metallurgical and Materials Engineering, Kastamonu University, Kastamonu, Turkey
5 Technical Sciences Vocational High School, Adıyaman University, Adıyaman, Turkey

Article Info	Abstract
	In this study, Cu–Mo composite coatings were produced on copper substrate by plasma spray technique. Electrical conductivity, microstructure and wear properties of the composite coatings were investigated. Microstructure and phase composition of the coatings were examined by using optical microscopy (OM), scanning electron microscope (SEM), X-ray diffraction (XRD), and energy-dispersive X-ray spectroscopy (EDS). The microhardness experiments were also performed by using a microhardness machine. The electrical conductivity properties of the coatings were evaluated with eddy current instruments. Wear tests were performed by pin-on-disc method. Although the electrical conductivities of the coatings are very small compared to the substrate, it has been determined that the coatings exhibit very good tribological property and high hardness in comparison to the substrate.

1. Introduction

During the reason for the copper to remain as the most important engineering materials every day is; high corrosion resistance, excellent electrical and thermal conductivity, attractive appearance, high ductility and ease of forming. Pure copper is widely used in the transmission of electric current in places related to cables, wires, electrical contacts and other electrical works. Copper and some alloys are used in automotive radiators, heat exchangers, home heating systems, panels for solar energy absorption, and applications where heat is required to quickly transfer from one point of metal to another [1]. Despite the high electrical, thermal conductivity and good corrosion resistance of copper, properties such as low hardness, yield strength, creep resistance and low wear resistance limit the use of copper. Because pure copper recrystallizes at temperatures close to 500 °C, even if hardened by cold forming, and therefore quickly loses its strength. A lot of work has been done in the literature to come from above. Most of the researchers have focused on the production of ceramic reinforced copper matrix composites. In the literature, Al_2O_3, SiC, TiB_2, TiC, B_4C and WC particles are usually added to the Cu matrix [2-6]. In these previous studies, pore formation reveals the negative side of the studies. As is known, pore formation adversely affects the mechanical properties as well as the electrical conductivity

properties. Junjie et al. [7] studied the hardness and electrical conductivity of Cu-matrix nanocomposites reinforced with in-situ TiC fabricated using long-term ball milling and hot pressing. It has been detected that as the ball milling time increased, the hardness and electrical conductivity increased. Chenchen et al. [8] reported that microstructures, mechanical and electrical properties of ZrB_2 microparticles reinforced Cu composites prepared by hot-pressed sintering. The results indicated that the relative density and electrical conductivity of the composites decrease with increasing ZrB_2 content. Huanchao et al. [9] added a new generation of graphite into the copper. The Gr/Cu composites were produced by using ball milling and cold compacting sintering process. The mechanical and physicochemical properties including hardness, relative density, conductivity and oxidation resistance were tested. The relative density, hardness, oxidation weight gain and IACS of the materials obtained by the optimum process parameters were 90.0%, 53.4HB, 1.6 mg cm^{-2} and 76.2%, respectively. While the mechanical properties of the Cu matrix composites are improved, the deterioration of the electrical conductivity properties is normal. The important thing is that the electrical conductivity does not fall too much. Zhan and Zhang report that in the study on graphite and SiC hybrid particles reinforced copper composite and its tribological characteristic, for Cu-23vol.% reinforcements (Gr+SiC) composite, while the electrical conductivity of the composite decreased by 14%, the wear rate decreased by 48% [10].

In this study, we tried to improve the wear and hardness properties without compromising the electrical conductivity of the copper material too much. For this purpose, a Cu + Mo coating layer with different ratios was produced on copper substrate using plasma spraying method. Molybdenum is a typical refractory metal with body-centered cubic (BCC) lattice structure. The high melting point (2610 °C) is characterized by low thermal expansion coefficient and high thermal/electrical conductivity [11]. In the literature, the use of Mo in copper alloys is very limited, and coating production is not available. Plasma spraying is effectively and economically applied to various machine parts to reduce surface defects [12]. In this method, the complete or partial melting of the powders varies depending on their thermal properties. The controllability of the system at extremely high heating and cooling rates makes it possible to produce coatings made of metallic, non-metallic and ceramics and combinations with this method [13]. In this study, Cu-Mo coatings produced on copper substrate with plasma spray method have both ideal wear resistance and relatively suitable electrical conductivity. In addition, these substrates are repeatedly coated with the plasma spray method and the worn parts become resistant to wear again. These two cases clearly reveal the contribution of the study to science.

2. Materials and Methods

Pure copper plates at 20 mm x 60 mm x 5 mm and 99.9% purity were selected as the substrate. Cu and Mo powders with -90+45 μm (Metco 55) and -75+45 μm (Metco 63NS) grain sizes respectively were coated on the substrate using plasma spray method. Mo was added to Cu in proportions of 10, 25 and 50% by weight. In the production of the coating layers, a Sulzer Metco F4-MB model plasma spray coating system with a power of 55 kW was used. The principle scheme of the plasma spray coating process is shown in Fig. 1. The production parameters of the coatings are summarized in Table 1. The flow rate of the argon gas used to produce the plasma beam was set at 35 l / min in all coatings. Spraying was made at a distance of 80 mm. The coating powders are injected externally into the gun. The injected powders are oriented parallel to the plasma flow. The coating powder feed rate was set to 50 g/min, the H_2 gas flow rate to 10 l/min and the carrier gas rate to 3 l/min.
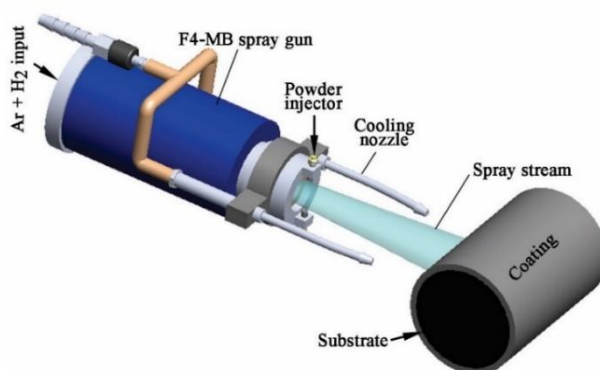
Fig. 1 Sulzer Metco F4-MB model plasma spray coating system

Table 1 Production parameters

Parameters	
Gun type	Sulzer-Metco F4
Current (A)	580
Volt (V)	60-65
Ar gas flow (l/min)	35
H_2 gas flow (l/min)	10
Spray distance (mm)	80
The amount of powder feed (g/min)	50
Carrier gas (Ar) flow (l/min)	3.0

The microstructure and phase formation properties of the coatings were determined by SEM-EDS and XRD analyses. The hardness was measured under a load of 300 grams with a microhardness device and at a waiting time of 15 seconds by using SHIMADZU HMV-G21 model microhardness machine. The electrical conductivities of coatings (Cu-Mo) and substrate (Cu) were measured according to ASTM E1004-02 standard with eddy current principle. Wear tests were performed by pin-on-disc method and ASTM G133 standard with 10 N loads, wear rate of 5 cm/s, 300 m slip distance and balls Ø6 mm 100Cr6 steel. Profiles of wear surfaces are determined by surface profilometer device. The wear volumes were determined using the wear profiles. After calculating volumes, wear rates were calculated according to Archard's law [14].

3. Results and Discussion

Fig. 2 illustrates optical images of coatings. The thickness of the interlayer coating is 300 µm. It is seen that the coating layers are homogeneous. As the Mo content increased, the porosity increased. The bond between the coating and the substrate is compatible. There is a covering layer in the appearance of a laminated structure. In all coatings, a lamellar microstructure is observed, which is well known in thermal spray coatings and is formed by molten metal droplets impacting the substrate and continuously wetting it [15, 16]. The lamellar structure occurs in the form of impingement of molten particles on the substrate,

deformation, and solidification. [17]. According to Kuroda and Kobayashi [18] the lamella is formed parallel to the substrate and the middle part of the lamella is thick and the thickness is decreased towards the end parts.

(a)

(b)

(c)
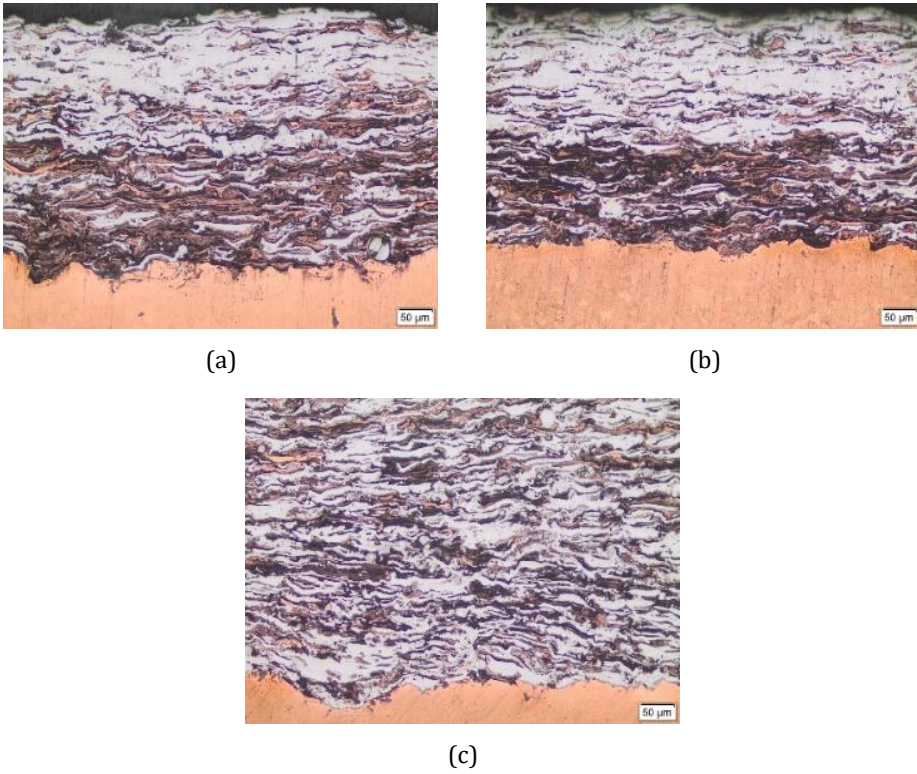
Fig. 2 (a) Cu-10 Mo coating (b) Cu-25 Mo coating, (c) Cu-50 Mo coating.
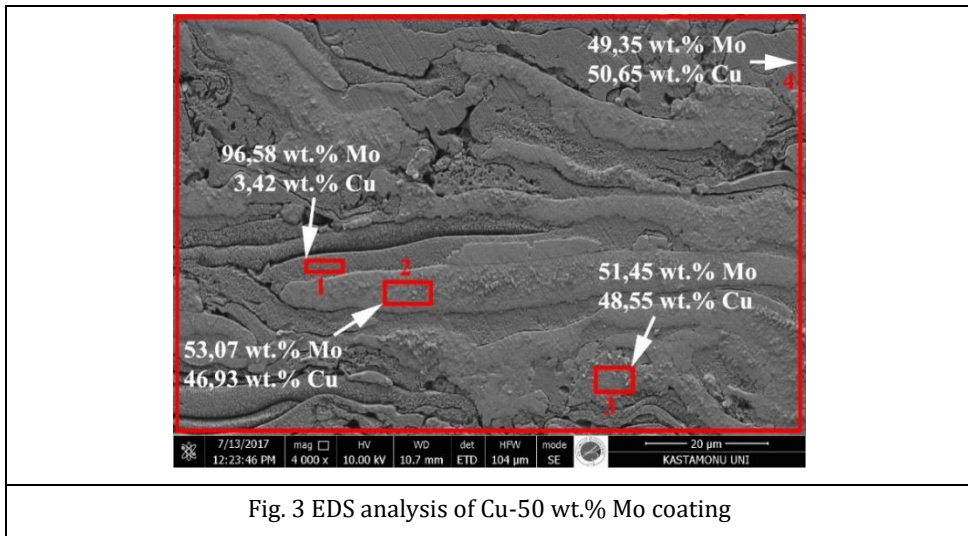
Fig. 3 EDS analysis of Cu-50 wt.% Mo coating

The EDS analysis of the Cu-50 wt.% Mo coating produced by the plasma spray method on the Cu substrate is given in Fig. 3. The chemical compositions of different lamellae are formed in the coating. When the area from the coating layer EDS is examined, it is seen that the coating represents the Cu-50 wt.% Mo content. The MAP analysis of Fig. 4 shows that all three coatings with relatively homogeneous distribution of the elements present in the coating layer. The distribution of the elements in the coating affects the electrical conductivity and mechanical properties.

(a)   (b)

(c)
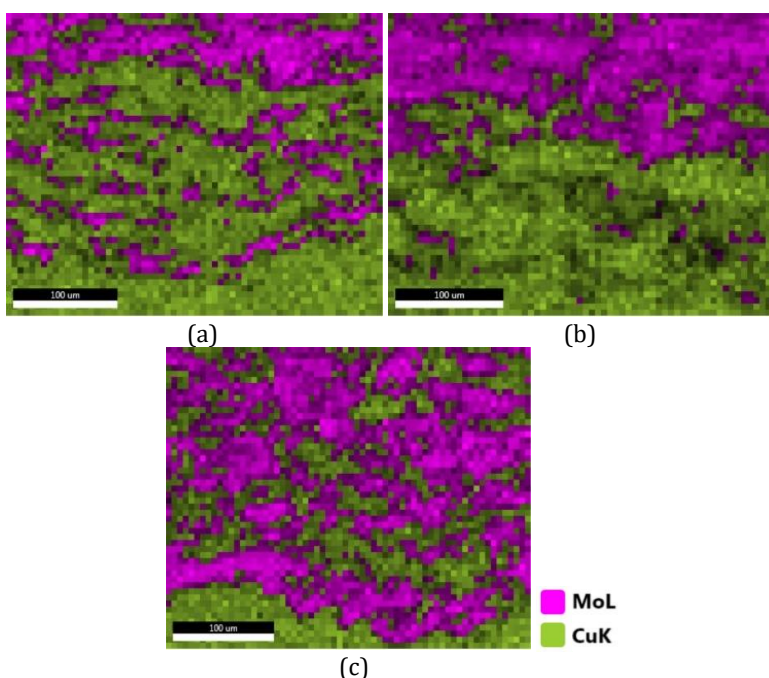
Fig. 4 SEM-MAP analyses of coatings; (a) Cu-10 wt.% Mo coating (b) Cu-25 wt.% Mo coating, (c) Cu-50 wt.% Mo coating

Fig. 5 illustrates the XRD graphic of Cu-Mo composite coatings which are produced with plasma spray. Cu and Mo phases are present in the coating layers. No oxide formation has occurred in the coatings and substrate. No phase formation occurred between Cu and Mo. According to the Cu-Mo phase diagram, this is normal. Because the Cu-Mo phase diagram is a monotectic diagram [19]. The result is that Cu-Mo coatings are mechanical mixtures of the refractory metal Mo and Cu with a face-centered cubic structure. Fathy et al [20] investigated effect of ZrO_2 content on properties of $Cu-ZrO_2$ nanocomposites synthesized by optimized high energy ball milling. They reported that no chemical reaction occurred between Cu and the reinforcing element and no new phase was formed.
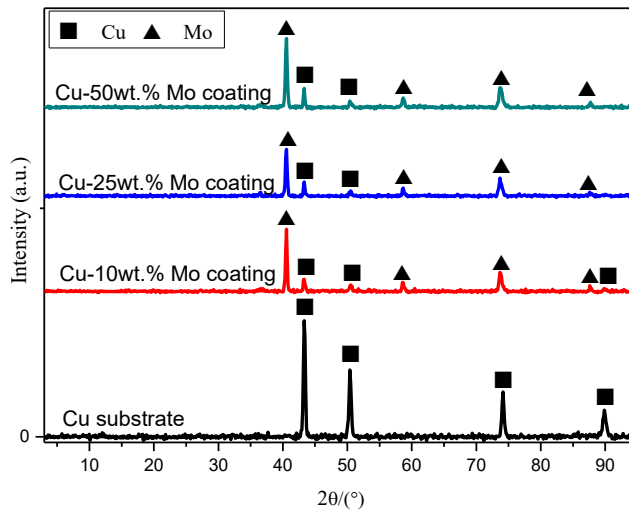
Fig. 5 XRD graphic of Cu-Mo composite coatings

The hardness graph of the coatings is given in Fig. 6a. Six hardness measurements were taken from each sample. Averages of hardness were taken and evaluated. The hardness of the Cu substrate was 81 $HV_{0.3}$, while the hardness of the 10, 25, and 50% Mo coating was measured as 127 $HV_{0.3}$, 140 $HV_{0.3}$ and 155 $HV_{0.3}$, respectively. The hardness was increased by coating with Cu substrate (56-91%). As the addition of Mo increases, the hardness of the coatings increases. This is due to the natural hardness of Mo (2 GPa) [21]. The electrical conductivity graph of the coatings is given in Fig. 6b. With the increase of molybdenum, the electrical conductivities of the coatings decreased. This is due to the fact that the electrical conductivity of Mo is lower than that of Cu and the porosity is increased by the addition of Mo.

(a)

(b)
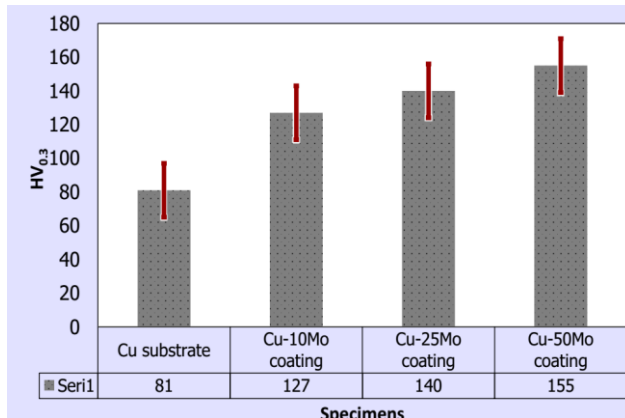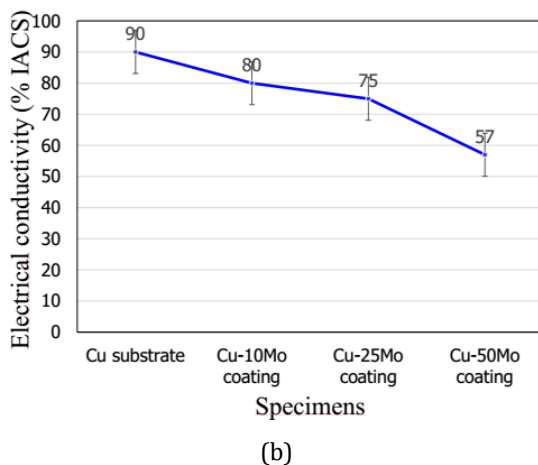
Fig. 6 (a) Hardness graph (b) Electrical conductivity graph

Coating of Cu substrate with Cu-Mo powder mixture resulted in a significant increase in the hardness. The electrical conductivity of the Cu substrate is measured as 90% IACS, while the electrical conductivities of the coatings are in the range of 57-80% IACS. These coatings can be used in areas where the electrical conductivity value is not too high than 57-80% IACS and the hardness is high.

The friction coefficient and wear rates of all samples are given in Figure 7. The friction coefficient for the copper base is 0.596. It varies in the range of 0,515-0,554 depending on the Mo additive in the Mo doped samples. As it is understood from these values, Mo particles showed solid lubricant and lowered the friction coefficient according to the substrate material. The wear rate for the copper substrate is $\sim 0.112 \times 10^{-3}$ mm^3/Nm, while the wear rates for 10%, 25 and 50% of Mo are changed as $\sim 0.097 \times 10^{-3}$ mm^3/Nm, $\sim 0.095 \times 10^{-3}$ mm^3/Nm and $\sim 0.075 \times 10^{-3}$ mm^3/Nm, respectively.
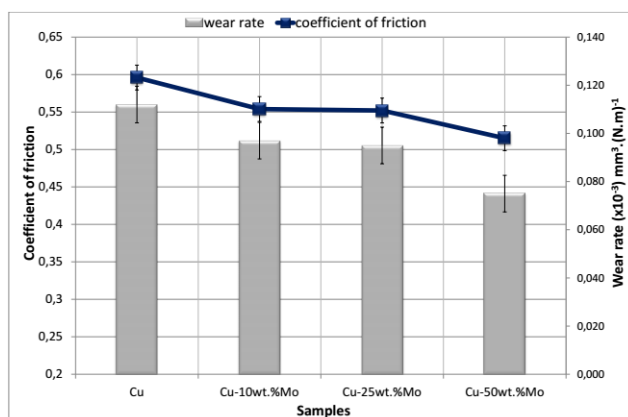
Fig. 7 Wear rate and COF of Cu-Mo composite coatings

Figure 8 shows the morphology of the worn surfaces of the substrate and coating layers under 10 N load. Both the adhesive and abrasive wear types dominate the substrate and coating layers. Material wastage after abrasion of the substrate, dense plastic deformation and micro-wedge gutters, and at least wedge formation and debris appear. On the wear surface of the coating layer, plastic deformation and micro-waviness are not to be investigated. This is due to the fact that the coating layer is hard and friction coefficient are low.
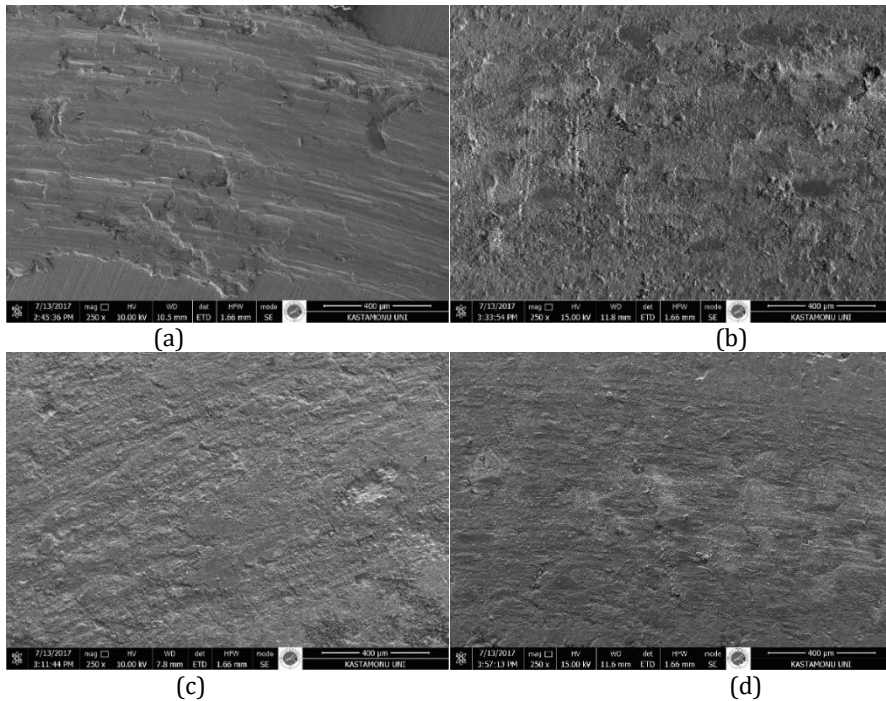
Fig. 8 Morphology of worn surfaces (a) Cu substrate, (b) Cu-10wt.%Mo, (c) Cu-25wt.%Mo and (d) Cu-50wt.%Mo

4. Conclusion

Cu-Mo composite coatings have been successfully produced on copper substrate by using plasma spray technique. Microstructure, wear and electrical properties of coatings were investigated. Coating of Cu substrate with Cu-Mo powder mixture resulted in a significant increase in the hardness. The hardness value for the uncoated Cu was measured as $HV_{0.3}$, while the hardness value for Cu-50wt.% Mo was measured as 155 $HV_{0.3}$. The electrical conductivity of the Cu substrate is measured as 90% IACS, while the electrical conductivities of the coatings are in the range of 57-80% IACS. Although the electrical conductivities of the coatings are very small compared to the substrate, it has been determined that the coatings exhibit a very good hardness values in comparison to the substrate. These coatings can be used in areas where the electrical conductivity value is not too high than 57-80% IACS and the hardness is high. Although the electrical conductivities of the coatings are very small compared to the substrate, it has been

determined that the coatings exhibit a very good tribological performance in comparison to the substrate.

References

[1] Akhtar, F, Askari, SJ, Shah, KA, Du, X, Guo, S. Microstructure, mechanical properties, electrical conductivity and wear behaviour of high volume TiC reinforced Cu-matrix composites. Materials Characterization, 2009; 60: 327–336. https://doi.org/10.1016/j.matchar.2008.09.014

[2] Chandrasekhar, SB, Sudhakara Sarma, S, Ramakrishna, M, Suresh Babu, P, Rao, TN, Kashyap, BP, Microstructure and properties of hot extruded Cu–1wt% Al_2O_3 nano-composites synthesized by various techniques. Materials Science and Engineering: A, 2014; 591: 46-53. https://doi.org/10.1016/j.msea.2013.10.074

[3] Božić, D, Stašić, J, Ružić, J, Vilotijević, M, Rajković, V, Synthesis and properties of a Cu–Ti–TiB_2 composite hardened by multiple mechanisms. Materials Science and Engineering: A, 2011; 528: 8139-8144. https://doi.org/10.1016/j.msea.2011.07.061

[4] Akbarpour, MR, Salahi, E, Alikhani Hesari, F, Simchi, A, Kim, HS, Microstructure and compressibility of SiC nanoparticles reinforced Cu nanocomposite powders processed by high energy mechanical milling. Ceramics International, 2014; 40: 951-960. https://doi.org/10.1016/j.ceramint.2013.06.091

[5] Islak, S, Kır, D, and Buytoz, S. Effect of sintering temperature on electrical and microstructure properties of hot pressed cu-tic composites. Science of Sintering, 2014; 46: 15-21. https://doi.org/10.2298/SOS1401015I

[6] Yener, T, Altinsoy, I, Yener, SC, Efe, GC, Ozbek, I, Bindal, C. An Evaluation of Cu-B_4C Composites Manufactured by Powder Metallurgy. Acta Physica Polonica A, 2015; 127(4): 1045-104. https://doi.org/10.12693/APhysPolA.127.1045

[7] Junjie Ni, Jian Li, Wei Luo, Qi Han, Yibin Yin, Zhengfeng Jia, Baoxu Huang, Chengchao Hu, Zelu Xu, Microstructure and properties of in-situ TiC reinforced copper nanocomposites fabricated via long-term ball milling and hot pressing, Journal of Alloys and Compounds, Volume 755, 2018, Pages 24-28. https://doi.org/10.1016/j.jallcom.2018.04.327

[8] Chenchen, W, Huaijun, L, Zhiguo, Z, Wei L. Fabrication, interfacial characteristics and strengthening mechanisms of ZrB_2 microparticles reinforced Cu composites prepared by hot-pressed sintering. Journal of Alloys and Compounds, 2018; 748: 546-552. https://doi.org/10.1016/j.jallcom.2018.03.169

[9] Huanchao, L, Xinying, T, Weibing, W, Xiangwei, W, Jinfeng, L, Haoran, G. Effect of graphene addition on properties of Cu-based composites for electrical contacts. Materials Research Express, 2017; 4(6): 66506. https://doi.org/10.1088/2053-1591/aa701b

[10] Zhan, Y, and Guoding, Z. Graphite and SiC hybrid particles reinforced copper composite and its tribological characteristic. Journal of materials science letters, 2003;22: 1087-1089. https://doi.org/10.1023/A:10249868

[11] Cockerman, BV. Measuring the fracture toughness of molybdenum–0.5 pct titanium–0.1 pct zirconium and oxide dispersion-strengthened molybdenum alloys using standard and subsized bend specimens. Metallurgical and Materials Transactions A, 2002; 33A: 3685–707. https://doi.org/10.1007/s11661-002-0242-y

[12] Song, EP, Ahn, J, Lee, S, Kim, NJ. Effects of critical plasma spray parameter and spray distance on wear resistance of Al_2O_3-8 wt.%TiO_2 coatings plasma-sprayed with nanopowders. Surface and Coatings Technology, 2008; 202: 3625-3632. https://doi.org/10.1016/j.surfcoat.2008.01.002

[13] Datye, A, Koneti, S, Gomes, G, Wu, KH, Lin, HT. Synthesis and characterization of aluminum oxide-boron carbide coatings by air plasma spraying. Ceramics International, 2010; 36: 1517-1522. https://doi.org/10.1016/j.ceramint.2010.02.024

[14] Zhou, F, Wang, Y, Liu, F, Meng, Y, Dai, Z. Friction and wear properties of duplex MAO/CrN coatings sliding against Si_3N_4 ceramic balls in air, water and oil. Wear, 2009;267:1581-1588. https://doi.org/10.1016/j.wear.2009.06.009

[15] Li, CJ, Yang, GJ, Ohmori, A. Relationship between particle erosion and lamellar microstructure for plasma-sprayed alumina coatings. Wear, 2006; 260: 1166-1172. https://doi.org/10.1016/j.wear.2005.07.006

[16] Lee, CH, Kim, HK, Choi, HS, Ahn, HS. Phase transformation and bond coat oxidation behavior of plasma-sprayed zirconia thermal barrier coating. Surface and Coatings Technology, 2000;124:1-12. https://doi.org/10.1016/S0257-8972(99)00517-4

[17] Fervel, V, Normand, B, Coddet, C. Tribological behavior of plasma sprayed Al_2O_3-based cermet coatings. Wear, 1999; 230:70-77. https://doi.org/10.1016/S0043-1648(99)00096-4

[18] Kuroda, T, Kobayashi, A. Adhesion characteristics of zirconia-alumina composite coatings by gas tunnel type plasma spraying. Vacuum, 2004; 73:635-641. https://doi.org/10.1016/j.vacuum.2003.12.105

[19] Subramanian, PR, Laughlin, DE. The Cu-Mo (Copper-Molybdenum) system. Bulletin of Alloy Phase Diagrams, 1990; 11(2): 169-172. https://doi.org/10.1007/BF02841703

[20] Fathy, A, Wagih, A, Abu-Oqail, A. Effect of ZrO_2 content on properties of Cu-ZrO_2 nanocomposites synthesized by optimized high energy ball milling. Ceramics International, 2019;45:2319-2329. https://doi.org/10.1016/j.ceramint.2018.10.147

[21] Firstov, S.A, Rogul, TG, Dub, SN, Svetchnicov, VL, Zandbergen, HW. Structure, Mechanical Behavior and Nanohardness of Chromium and Molybdenum Produced by Magnetron Sputtering. In Metallic Materials with High Structural Efficiency, 2004; 146:341-346. https://doi.org/10.1007/1-4020-2112-7_34

Research Article

Influence of seawater on mechanical properties of SiO₂-epoxy polymer nanocomposites

Halil Burak Kaybal[*,a,1], Hasan Ulus[b,2], Ahmet Caner Tatar[c,3], Okan Demir[d,3], Ahmet Avcı[e,4]

[1]Department of Mechanical Engineering, Amasya University, Amasya, Turkey.
[2]Huglu Vocational High School, Selcuk University, Konya, Turkey
[3]Department of Mechanical Engineering, Konya Technical University, Konya, Turkey
[4]Department of Biomedical Engineering, Necmettin Erbakan University, Konya, Turkey

Article Info	Abstract
	In this study, dispersion of nano SiO2 in epoxy composite aged in seawater and its effect on mechanical properties were studied. The SiO2-epoxy polymer nanocomposite materials were kept in seawater for a total of six months to be tested every two months. Tensile and bending tests were applied to composite materials as a mechanical test. According to the mechanical test results, there was less decrease in strength in SiO2-epoxy polymer nanocomposite material compared to unmodified material. In usage of seawater, the mechanical properties were observed to be the best in 3 % added SiO2-epoxy nanocomposite material.

1. Introduction

Epoxy resins are thermoset materials widely used (used widely) in structural and composite materials due to their properties such as high strength, low shrinkage, effective electrical insulation, excellent adhesion, chemical and solvent resistance, low toxicity and low cost. Moreover, it has high hardness, heat and wear resistance (1-3). Also, epoxy resins are generally used as coatings, casting materials, binders and adhesives application (4). The use of nanoparticles is a common method used to improve the strength of epoxy resins. Nanoparticles can enhance interfacial area between fillers and polymer (5). Thus, an increment in performance on the properties of epoxy resin is observed (5, 6). In the literature, boron nitride, CNT (7), nano clay (8), silica (9), graphene (10), nano-Al₂O₃, nano-SiO₂, nano-CaCO₃ (11-16) nanoparticles are commonly used to improve composite material properties. For instance, Zhai et al. improved adhesion properties with 2 wt % of nano-Al₂O₃ in epoxy matrix (11). Bauer et al observed that the epoxy's glass transition temperature and viscoelastic properties changed with the addition of nano-sized silica, alumina and titania (12). Zhang et al. introduced different rates of Nano SiO₂ to the epoxy polymer. They increased the toughness of the Epoxy/ SiO₂ composite as a result of impact test (13). Suraj and Raman investigated the effect of nano and micro sized aluminum

particles in epoxy polymer on fracture toughness. They found that enhancement on(of) fracture toughness and highest values for increase in fracture toughness of epoxy is found for addition of 20 -100 nm aluminum particles (14). Park and Jana achieved to increase the tensile and impact strength of composite materials with nano clay reinforcement (17). It is known that polymeric resins can be influenced by water in marine applications. The interface of filler-polymer or fiber-polymer may weaken when the resin absorbs water (18). Wei et al. examined the effect of seawater on the tensile and bending strength of fiber reinforced composite materials. They observed that these strengths decreased with the effect of seawater (19). Li and Weitsman concentrated on seawater induced damage in composite sandwich structures, gaining weight, expansion strain, and on possible deterioration in the properties of the materials (20). Davies et al. studied on four different thermoset resins and their glass fiber reinforced composite under three immersion conditions (21). In other studies conducted in the literature, it is stated that moisture and salt water absorption directly affects the mechanical, physical and chemical properties of composite materials (20-23).

In this research, the influence of seawater aging on the mechanical performance of epoxy nanocomposites filled with different proportions from 1 wt % to 5 wt % of nano-SiO_2 have been studied for marine application. The nanocomposites were submerged in seawater for up to six months at room temperature for the first time in the literature. The specimens were mechanically examined every two months. Tensile and bending tests were evaluated as mechanical properties according to the related standard methods. The experimental results illustrate that the SiO_2 nanoparticles left a positive influence on the mechanical performance of the nanocomposites in the sea water conditioning.

2. Material and Methods

2.1. Material

The diglycidylether of bisphenol-A (DGEBA) epoxy resin (L160 code) and suitable curing agent (H160 code) supplied by Momentive Hexion Inc. as the commercially available. The SiO_2 nanoparticles, have a specific surface area of 650 m^2/g, was purchased from MKnano Canada Company and average primary particle diameter of 15 nm. It can be seen powder SiO_2 in Fig 1.
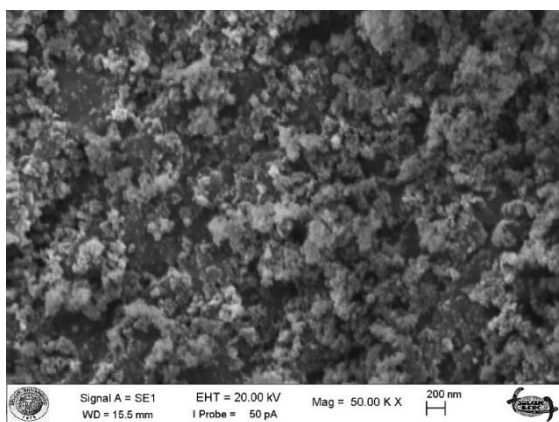
Fig. 1. SEM image of powder SiO_2

2.2. Production of Composites

Nanocomposite materials were manufactured at rates of 1 % to 5 % nano- SiO_2. These ratio values are taken in accordance with the literature (13). Epoxy and powdered nano-SiO_2 were mixed with the ultrasonicator for 30 minutes in the ice bath. After dispersing process curing agent was added in to epoxy and the mixture was degassed at 25 °C and 0.6 bar at approximately 20 min. Steel molds are covered with mold release in Fig 2(a). The epoxy mixture was cast into steel molds. Curing was performed firstly at 80 °C for approximately 1 h, then at 120 °C at approximately 2 h. After that it was slowly cooled to room temperature in the oven. Subsequently, the specimens were removed from the steel molds in Fig 2(b). All samples conventionally polished with SiC sandpapers with grit numbers of 800 to minimize effect stress concentration caused by sharp edges. The produced composite materials were transported to seawater environment and kept in seawater for 6 months.

(a)   (b)

Fig. 2 a) Steel mold b) Test specimens

2.3. Test procedure

Bending and tensile tests were performed as a mechanical test in the study. The ASTM D7264/ D7264M-07 standards were used for the bending test and the ASTM D4762 - 11a standards for the tensile test, respectively. The specimens were tested every two months. Shimadzu test machine which has 1 kN load cell was used for mechanical test. Tensile tests were carried out with 2 mm·min^{-1} tensile speed and bending tests were performed under 1 mm·min^{-1}.

3. Results and Discussions

In a previous study, we conducted that stress-displacement curves of different proportions of nano SiO_2 containing epoxy composites are shown for dry conditions in Fig. 3. It can be seen highest enhancement of the tensile strength and bending force is achieved with the 3 wt. nano % SiO_2 adding in Fig. 3 (a) and (b), respectively. Furthermore, mechanical properties of 1 wt. % and 2 wt. % epoxy/SiO_2 added nanocomposite are also increased. However, these figures shows that the tensile and bending properties are getting worse at 4 and 5 wt. % nano SiO_2 addition. We know that tensile properties decrease occurs due to the agglomerations of nano SiO_2 (24). Then, the composite specimens, aged under sea water condition, were tested every two months. Fig. 4 illustrated that curves of tensile and bending tests for SiO_2/Epoxy nanocomposite in seawater condition. It is clear that the all of composite specimens are negatively affected by sea water when the tensile strength and

bending force are examined. In addition, it is seen that nano reinforced composites are less effected than 0 wt. % epoxy/SiO$_2$. According to all curves, reinforcement of 3 wt. % SiO$_2$/Epoxy has better mechanical performance than the other proportions. In the end of 6th month, we did not get any results for bending test, due to excessive displacement in the nanocomposites.

(a) (b)
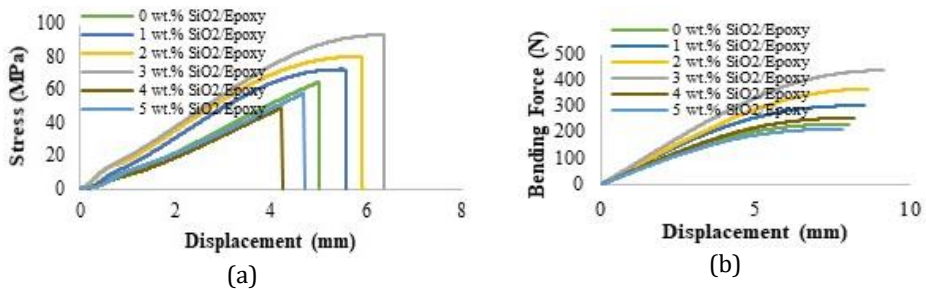
Fig 3. (a) Tensile curve (b) Bending curve in dry condition (24)
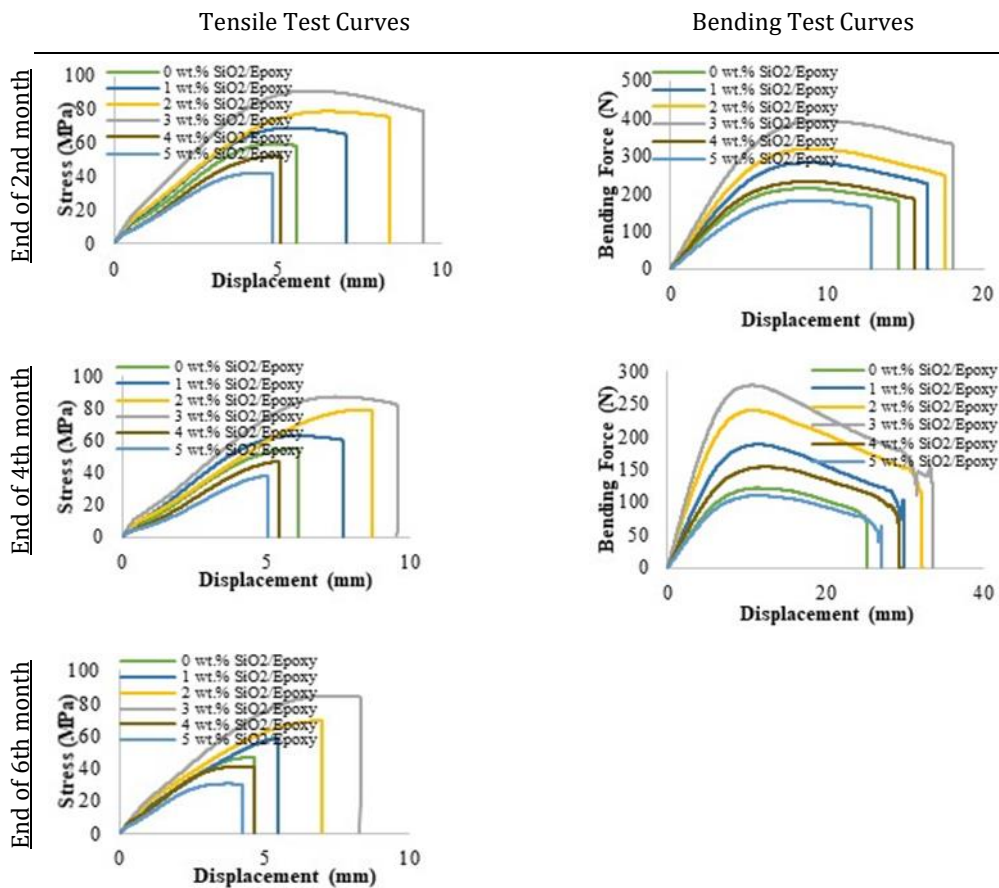
Fig 4. Tensile and Bending Curves in sea water condition for SiO$_2$/Epoxy nanocomposite

The nano-SiO_2 particles incorporated into the epoxy polymer have caused absorbing or deflection of the cracking in the matrix. The cracks in the epoxy have compelled to break and debonding the nano-SiO_2 particles. Since the composite needs more energy to achieve this event, the tensile strength and bending force values of the nanocomposite specimens are higher than neat composites. Fig. 5 gives an information about toughening mechanisms of nanocomposite materials such as crack deflection and particle debonding. The reduction of tensile strength and bending force in high proportions of nano-SiO_2 such as 4 and 5 wt. % is caused by the agglomeration of the particles. Fig. 6 demonstrates agglomeration of the SiO_2 nanoparticles in epoxy nanocomposites.
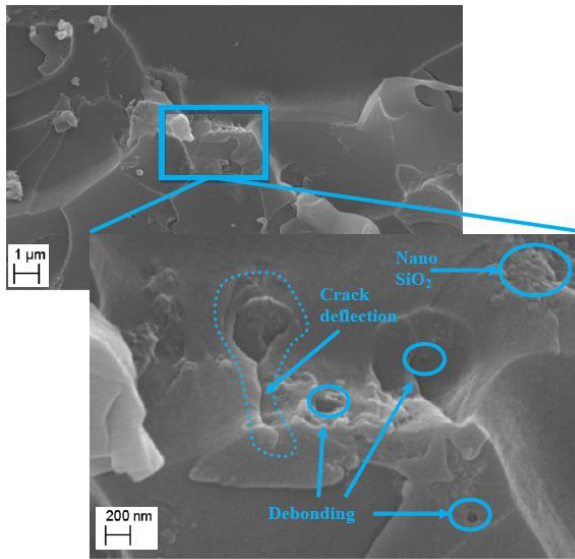
Fig 5. 3 wt. % SiO2/Epoxy Nanocomposite (24)
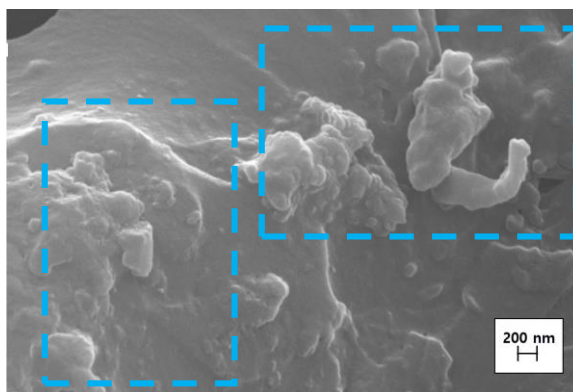
Fig 6. 5 wt. % SiO2/Epoxy Nanocomposite (24)

Compared to 0 wt. % SiO_2/Epoxy composite, the mechanical properties of 3 wt. % SiO_2/Epoxy nanocomposite are presented in Table 1. Although SiO_2 nanoparticles are enhanced the performance of tensile strength and load bending capacity in dry condition,

the particles cannot be prevented decrement of these mechanical performances after aging due to the detrimental effect of the absorbed seawater. Nevertheless, SiO_2 nanoparticles are succeeded in delaying the damage mechanisms when the numerical results in Table 1 are considered.

Table 1. Results of mechanical test for 0 wt.% and 3 wt.% SiO_2/Epoxy nanocomposite.

Mechanical Properties	Dry	Sea water			Nanocomposites
		2nd	4th	6th	
Tensile Strength (MPa)	65.2	59.4	54.9	46.7	0 wt.% SiO_2/Epoxy
	93.9	90.8	87.4	84.4	3 wt.% SiO_2/Epoxy
Bending Force (N)	233	213.5	121.2	-	0 wt.% SiO_2/Epoxy
	438.5	393.7	277.9	-	3 wt.% SiO_2/Epoxy

The mechanical properties of the composite specimens under the seawater effect are reduced in Fig. 3 and Fig. 4. In addition to the reduced load carrying capacities under the influence of seawater, the displacements under stress are increased in both of composites. In composite specimens immersed in seawater, the absorbed water interacts chemically with the epoxy polymer by way of Van der Waals and hydrogen bonds. This chain mobility causes polymerization and reducing mechanical strength for tensile and bending in the composite material (25). The minimum reducing mechanical strength is obtained for nanocomposite specimens. The fracture surfaces of tested specimens were observed by Scanning Electron Microscope (SEM) for 0 wt. % epoxy/SiO_2 composite and 3 wt. % epoxy/ SiO_2 nanocomposite in Fig. 7. Polymerization and degradation areas of 0 wt. % epoxy/ SiO_2 composite in seawater condition are shown in Fig. 7(a). Besides, strengthening mechanism of the 3 wt. % epoxy/ SiO_2 nanocomposite are seen in Fig. 7(b). Larger polymerization areas in composite material are seen compared to the nanocomposite material. Nano- SiO_2 particle debonding in fracture surface is ensured that nanocomposite is swallowed more energy and is increased its strength.

(a)   (b)
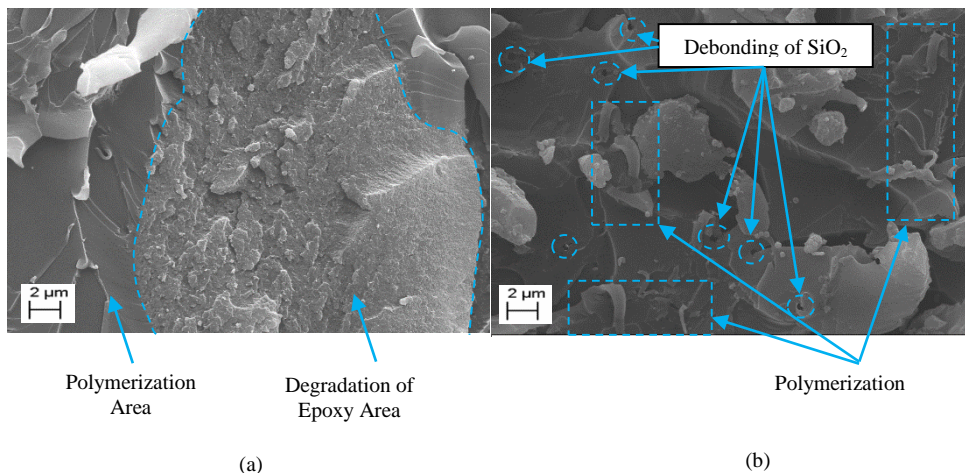
Fig. 7 SEM images of fracture surface (a) 0 wt. % epoxy/SiO_2 composite (b) 3 wt. % epoxy/SiO_2 nanocomposite

3. Conclusion

Consequently, the studies on the mechanical properties show that the reinforcement of SiO_2 nanoparticles in the epoxy matrix polymer has significant positive or negative influences on nanocomposites for both of dry and seawater conditions. From the results of this study, the following conclusions can be drawn:

- High proportions of SiO_2 nanoparticles (e.g. 4-5 wt. %) have shown weak performance in load capacity due to agglomeration of particles.
- The other proportions of SiO_2 nanoparticles in epoxy matrix polymer are demonstrated superior properties in both of condition.
- According to result of mechanical test, sea water absorption is weaken both tensile strength and bending force. But, SiO_2 added nanocomposites are less affected after aging than the others.
- At the end of the sixth month of bending test results, a displacement exceeding the device capacity has occurred.
- The reducing mechanical strength is fewest for 3 wt. % epoxy/SiO_2 in seawater condition.

References

[1] Kalogeras IM, Roussos M, Christakis I, Spanoudaki A, Pietkiewicz D, Brostow W, et al. Dielectric properties of cured epoxy resin+ poly (ethylene oxide) blends. Journal of non-crystalline solids. 2005;351(33-36):2728-34. https://doi.org/10.1016/j.jnoncrysol.2005.03.066

[2] Maity T, Samanta B, Dalai S, Banthia A. Curing study of epoxy resin by new aromatic amine functional curing agents along with mechanical and thermal evaluation. Materials Science and Engineering: A. 2007;464(1-2):38-46. https://doi.org/10.1016/j.msea.2007.01.128

[3] Shi H, Liu F, Yang L, Han E. Characterization of protective performance of epoxy reinforced with nanometer-sized TiO2 and SiO2. Progress in Organic Coatings. 2008;62(4):359-68. https://doi.org/10.1016/j.porgcoat.2007.11.003

[4] Boyle MA, Martin CJ, Neuner JD. Epoxy resins. ASM Handbook Volume 21 Composites. 2001:78-89.

[5] Zheng Y, Zheng Y, Ning R. Effects of nanoparticles SiO2 on the performance of nanocomposites. Materials Letters. 2003;57(19):2940-4. https://doi.org/10.1016/S0167-577X(02)01401-5

[6] Song G. Polymeric nano-metered composites. Mater Rep. 1996;4(1):57-60.

[7] Ulus H, Şahin ÖS, Avcı A. Enhancement of flexural and shear properties of carbon fiber/epoxy hybrid nanocomposites by boron nitride nano particles and carbon nano tube modification. Fibers and Polymers. 2015;16(12):2627-35. https://doi.org/10.1007/s12221-015-5603-4

[8] Wang L, Wang K, Chen L, Zhang Y, He C. Preparation, morphology and thermal/mechanical properties of epoxy/nanoclay composite. Composites Part A: Applied Science and Manufacturing. 2006;37(11):1890-6. https://doi.org/10.1016/j.compositesa.2005.12.020

[9] Liu Y-L, Hsu C-Y, Wei W-L, Jeng R-J. Preparation and thermal properties of epoxy-silica nanocomposites from nanoscale colloidal silica. Polymer. 2003;44(18):5159-67. https://doi.org/10.1016/S0032-3861(03)00519-6

[10] Rafiee MA, Rafiee J, Srivastava I, Wang Z, Song H, Yu ZZ, et al. Fracture and fatigue in graphene nanocomposites. small. 2010;6(2):179-83. https://doi.org/10.1002/smll.200901480

[11] Zhai L, Ling G, Li J, Wang Y. The effect of nanoparticles on the adhesion of epoxy adhesive. Materials Letters. 2006;60(25-26):3031-3. https://doi.org/10.1016/j.matlet.2006.02.038

[12] Bauer F, Decker U, Ernst H, Findeisen M, Langguth H, Mehnert R, et al. Functionalized inorganic/organic nanocomposites as new basic raw materials for adhesives and sealants Part 2. International journal of adhesion and adhesives. 2006;26(7):567-70. https://doi.org/10.1016/j.ijadhadh.2005.11.001

[13] Zhang X, Xu W, Xia X, Zhang Z, Yu R. Toughening of cycloaliphatic epoxy resin by nanosize silicon dioxide. Materials Letters. 2006;60(28):3319-23. https://doi.org/10.1016/j.matlet.2006.04.023

[14] Zunjarrao SC, Singh RP. Characterization of the fracture behavior of epoxy reinforced with nanometer and micrometer sized aluminum particles. Composites Science and Technology. 2006;66(13):2296-305. https://doi.org/10.1016/j.compscitech.2005.12.001

[15] Yu H, Wang L, Shi Q, Jiang G, Zhao Z, Dong X. Study on nano-CaCO3 modified epoxy powder coatings. Progress in Organic Coatings. 2006;55(3):296-300. https://doi.org/10.1016/j.porgcoat.2006.01.007

[16] Li H, Zhang Z, Ma X, Hu M, Wang X, Fan P. Synthesis and characterization of epoxy resin modified with nano-SiO2 and γ-glycidoxypropyltrimethoxy silane. Surface and Coatings Technology. 2007;201(9-11):5269-72. https://doi.org/10.1016/j.surfcoat.2006.07.143

[17] Park JH, Jana SC. The relationship between nano-and micro-structures and mechanical properties in PMMA–epoxy–nanoclay composites. Polymer. 2003;44(7):2091-100. https://doi.org/10.1016/S0032-3861(03)00075-2

[18] Silva R, Aquino E, Rodrigues L, Barros A. Curaua/glass hybrid composite: the effect of water aging on the mechanical properties. Journal of reinforced plastics and composites. 2009;28(15):1857-68. https://doi.org/10.1177/0731684408090373

[19] Wei B, Cao H, Song S. Degradation of basalt fibre and glass fibre/epoxy resin composites in seawater. Corrosion Science. 2011;53(1):426-31. https://doi.org/10.1016/j.corsci.2010.09.053

[20] Li X, Weitsman YJ. Sea-water effects on foam-cored composite sandwich lay-ups. Composites Part B: Engineering. 2004;35(6-8):451-9. https://doi.org/10.1016/j.compositesb.2004.04.012

[21] Davies P, Mazeas F, Casari P. Sea water aging of glass reinforced composites: shear behaviour and damage modelling. Journal of composite materials. 2001;35(15):1343-72. https://doi.org/10.1106/MNBC-81UB-NF5H-P3ML

[22] Marcovich NE, Reboredo MM, Aranguren MI. Dependence of the mechanical properties of woodflour–polymer composites on the moisture content. Journal of Applied Polymer Science. 1998;68(13):2069-76. https://doi.org/10.1002/(SICI)1097-4628(19980627)68:13<2069::AID-APP2>3.0.CO;2-A

[23] Adams R, Singh M. The effect of immersion in sea water on the dynamic properties of fibre-reinforced flexibilised epoxy composites. Compos Struct. 1995;31(2):119-27. https://doi.org/10.1016/0263-8223(95)00007-0

[24] Kaybal HB, Ulus H, Demir O, Tatar AC, Avcı A. investigations on the mechanical properties of the nano sio2 epoxy nanocomposite. Applied Engineering Letters. 2017, 2(4); 121-124.

[25] Prolongo S, Gude M, Urena A. Water uptake of epoxy composites reinforced with carbon nanofillers. Composites Part A: Applied Science and Manufacturing. 2012;43(12):2169-75. https://doi.org/10.1016/j.compositesa.2012.07.014

Research Article

Poly (vinyl alcohol) and casein films: The effects of glycerol amount on the properties of films

Bedriye Ucpinar Durmaz[a,1], Ayse Aytac[*,b,1,2]

[1] Department of Chemical Engineering, Kocaeli University, Kocaeli, Turkey
[2] Polymer Science and Technology Program, Kocaeli University, Kocaeli, Turkey

Article Info	Abstract
	The aim of the present work was to investigate the effect of glycerol (GLY) concentration on the properties of poly (vinyl alcohol) (PVA)/casein (CAS) blend films. The films were prepared by solution casting method at the different concentrations of GLY. The structural, mechanical, thermal, barrier and hydrophilic-hydrophobic properties of the films were determined by various methods. The structural analysis indicated that there were some interactions between the components. Tensile test results release that tensile strength of the film decreased with the addition of GLY while strain at break values increased. According to thermogravimetric analysis (TGA) results, the GLY included films exhibited lower thermal stability than GLY-0 film. The residual weight decreased by increasing GLY content. The contact angle measurements showed that all films were hydrophilic structure. Also, the water vapor barrier property of the GLY-0 film was developed with the addition of GLY.

1. Introduction

In recent years, there has been an increasing interest in the development of biodegradable packaging materials due to the environmental concerns, renewability and cost-effectiveness. The polymers obtained from natural and biodegradable sources are an attractive alternative for the petroleum-based synthetic polymers.

Biodegradable polymers can be classified their raw materials and production methods: (1) directly obtained from biomass with extraction, such as polysaccharides (starch, pectin), lipids and proteins (milk proteins, soy protein). (2) The chemically synthesized polymers from bio-based monomers or mixing of petroleum and biomass such poly (vinyl alcohol) and polylactic acid. (3) The polymers produced by microorganisms such as poly (hydroxyl butyrate) [1–4]. Among the first group, proteins frequently used and studied for the food packaging applications due to the their nutritive value, abundance and film forming properties [4–6]. Especially, the bovine milk protein casein (CAS) previously investigated because of its film forming properties, high barrier to gases and transparency [6–8]. In addition, CAS based films are flavourless, odorless, colorless and smooth [8,9]. These properties make it appropriate for the food packaging, protecting and edible film applications. On the other hand, the mechanical properties (brittle) and water vapor permeability of CAS films restrict the usage area [10]. The addition of plasticizer and blending with biodegradable polymers can be used to develop these limitations.

Poly (vinyl alcohol) (PVA) is a biodegradable, water soluble, nontoxic and biocompatible polymer. It produces by the hydrolysis of poly (vinyl acetate). PVA has good mechanical and thermal property, chemical resistance and good barrier to gases and aroma [3,11,12]. Due to the its good film-forming property and water solubility PVA is a suitable polymer to blend with natural polymers and proteins. Different PVA/ natural polymer studies have been reported in the literature such as soy protein, myofibrillar protein, tara gum, alyssum homolocarpum seed gum, whey protein isolate which were produced by solution casting method. Generally, these blends have been prepared to use in the packaging, protecting and agricultural mulching film applications [5,12–17]. Also, in the literature PVA/CAS films have been prepared by electrospinning method for the wound dressing material [18] and enzyme substrate [19]. According to the best of authors knowledge, there is no PVA/CAS solution casting film study in the literature.

PVA has many hydroxyl groups in its structure and can form hydrogen bonds with protein molecules. These strong interactions restrict the molecular, chain movement and processability of the blends [12,15,19,20]. Besides that, casein has brittle film structure. In this sense, to overcome this processability and mechanical limitations plasticizers can be used. The plasticizers are low molecular weight non-volatile organic compounds. A plasticizer decreases the second order transition temperature and increases the flexibility of the materials by increasing the free volume of polymer. Furthermore, suitable amount plasticizer obstructs the crack formation during the transportation and packaging and improve the tear resistance and toughness of films. The polarity and molecular weight of plasticizer affects the efficiency. In addition, compatibility is important factor [10,21,22]. The natural based plasticizers generally used for PVA and CAS films. The most common plasticizers include different types of polyols (glycerol, poly (ethylene glycol)), sorbitol, lipids, oligosaccharides and sucrose [22]. Among these, glycerol is efficient and most widely used plasticizer. Because, it has more hydrophilic nature compared to sorbitol and also glycerol molecules are small [23–25]. Glycerol (GLY) was used as the plasticizer in our study. GLY is a high boiling point, water soluble, sweet taste liquid compound [26]. It is a good choice for the food packaging films due to the non-toxic property.

In this study, we aimed to develop a biodegradable, environmentally friendly material instead of non-biodegradable petroleum-based materials. The preparation of such a material will be an important development for both of the environment and living health. Additionally, it is a great advantage that casein used in the study is obtained from an edible and renewable source and cheap. This study proposes a new material produced by traditional method from cheap and renewable raw materials. It is believed that this material can be used in particular for packaging purposes. It is also important to find the optimum amount of plasticizer that affects many properties of the material obtained. So with this motivation, plasticized PVA/CAS films were prepared. Firstly, CAS was plasticized with different amount of GLY and blended with PVA as the ratio of 20:80. The effects of different loading levels of GLY in the film properties were investigated.

2. Experimental setup

2.1. Materials

Bovine milk casein powder (C3400) was obtained from Sigma Aldrich. High molecular weight poly (vinyl alcohol) (degree of hydrolysis = 86.7-88.7 mol%) was supplied from Kuraray Co. Ltd. as trade name of Kuraray Poval 47-88. Plasticizer glycerol ($C_3H_8O_3$, d=1.26kg/l) was supplied from Merck. Triethanolamine (TEA) (Purity: 99%, d= 1.12kg/l) was also supplied from Merck which was used as solvent for the CAS. The structures of materials are given in Fig. 1.
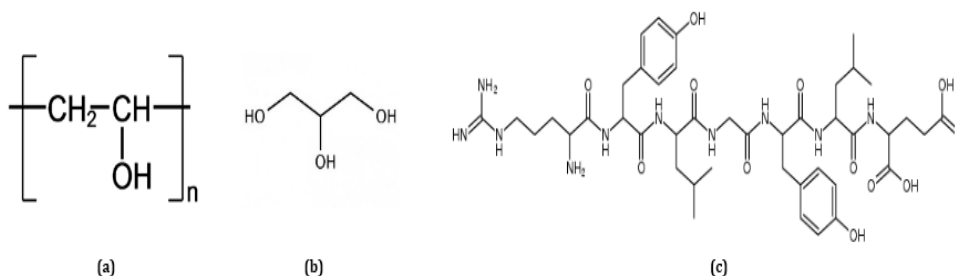
Fig 1. Chemical structures of materials (a) PVA, (b) GLY, (c) CAS

2.2. Preparation of films

The PVA/CAS/GLY films were prepared by solution casting method. Firstly, PVA was dissolved in distilled water under continuously stirring for 1h at 80 °C to obtain 6 wt.% solution. CAS and GLY were dissolved in the 5% TEA solution under magnetic stirring for 1h at 35°C to prepare a 6% plasticized CAS solution. The GLY/CAS ratio was changed as 0:100, 10:90, 15:85, 20:80 and 25:75. Then, plasticized CAS which includes different amount GLY and PVA were blended at the ratio of 20:80 (v/v). The mixed solution was continuously stirred for 15 min at room temperature to prepare homogeneous solution. The total solid content was kept at 6 g to obtain uniform film thickness. Finally, the film-forming solutions were casted onto the polystyrene petri plate (120mm x120mm) and dried at room conditions for 2 days. The prepared films were denoted according to different ratios of GLY as shown in Table 1.

Table 1 Formulations of prepared PVA/CAS films

| Sample Code | Dosage | | | | Total solid (g) (in 100 ml) | Number of produced specimens |
| | Plasticized CAS (g) | | | PVA (g) | | |
	CAS (g)	GLY (g)	GLY Percentage			
GLY-0	1.20	0	**0%**	4.8	6	3
GLY-10	1.08	0.12	**10%**	4.8	6	3
GLY-15	1.02	0.18	**15%**	4.8	6	3
GLY-20	0.96	0.24	**20%**	4.8	6	3
GLY-25	0.90	0.3	**25%**	4.8	6	3

2.3 Characterization

The structural analysis of the film was characterized by Fourier transform infrared spectroscopy (FTIR). A Perkin Elmer Spectrum 100 testing machine was used for the analysis. Spectra were obtained in the ranging from 650 to 4000 cm^{-1} wavelength.

The tensile test was used to determine the mechanical properties of the films. The test was applied according to ASTM-D 882 standard by using computer controlled Instron universal testing machine. The samples were cut into 20 mm x 80 mm rectangle pieces and measurement were conducted with 10 mm/min crosshead speed. The elongation at break and tensile strength values was determined.

The surface hydrophobicity of the films was determined by the sessile-drop method using Attention Theta Lite contact angle measurement instrument. The distilled water was dropped on the surface of film and the contact angle was recorded. To obtain the average contact angle value at least 10 measurements were made for each specimen.

Thermogravimetric analysis (TGA) (Mettler Toledo TGA 1) was conducted to measure the thermal stability of the PVA/CAS blend films. Measurements was carried out at temperatures ranging from 25 °C to 600 °C at the heating rate of 20 °C/min under nitrogen atmosphere. The sample weight was approximately 8-10 mg. The residual mass at 600°C, the onset temperature (T_{onset}), the end temperature (T_{end}) and the temperature at maximum rate of weight loss (T_{max}) were determined.

The water vapor permeability (WVP) of films was determined through the modified gravimetric method according to the ASTM E96 standard at 35% RH and 23°C.

3. Results and Discussions

3.1. FTIR analysis

The FTIR spectra of the pure and blend films can be seen at Fig. 2. The broad peaks at the range from 3282-3294 cm^{-1} are associated to the stretching of the hydroxyl (OH) groups of CAS and PVA from the intermolecular and intramolecular hydrogen bonds [18]. The -OH peak of GLY-0 (unplasticized PVA/CAS) film was shifted higher wavelength region and intensity of peak decrease on the GLY-25 spectrum. These are the evidence of interactions between PVA/CAS and GLY. GLY may cause destroyed the crystalline regions of polymers and random chain rearrangement [26].
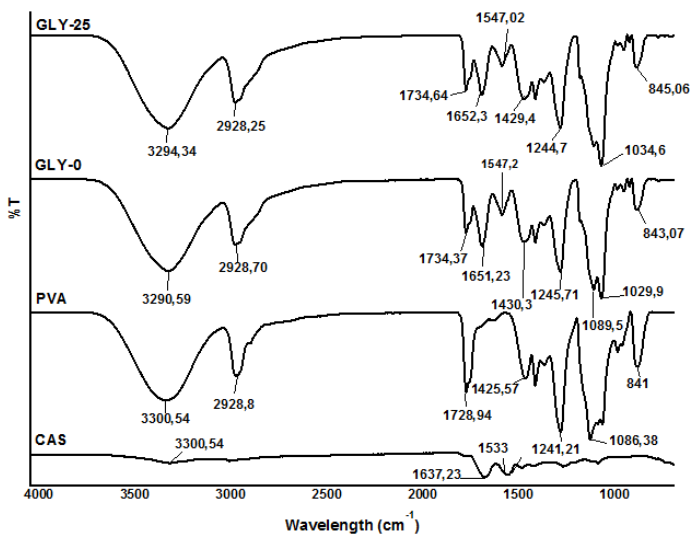
Fig. 2 FTIR spectra of pure PVA, CAS, GLY-0 and GLY-25

The absorptions bands of CAS at 1637 cm^{-1} indicate the –CONH vibration. Also, 1533 and 1515 cm^{-1} peaks are -NH bending vibrations of CAS structure. All these peaks indicate that the protein network structure of casein. These peaks were also seen in the spectra of PVA/CAS blend films and shifted high wavelengths. In the pure PVA film spectrum, a broad band at 3300 cm^{-1} which is attributed to the –OH groups, stretching vibration of C-H was seen at 2928 cm^{-1}, carbonyl group (C=O) vibration at 1728 cm^{-1}, C-O stretching vibration at 1086 cm^{-1} [15,18,26]. These bands were shifted at high or low wavelengths with

incorporation of CAS and GLY in the PVA structure. These results attributed to the interaction between the CAS, GLY and PVA materials.

3.2. Mechanical Properties of Films

The effects of plasticizer GLY amount on the mechanical properties of PVA/CAS film were evaluated and obtained results were given in Fig. 3-4.

The tensile strength results of blend films are given in Fig. 3 as a function of the amount of GLY. Tensile strength can be defined as the resistance of the film to the elongation under the applied stress [25]. The tensile strength value of unplasticized PVA/CAS film (GLY-0) was measured as 38 MPa. This value decreased by adding plasticizer and the reduction is about 22% for GLY-10 and GLY-15. As the amount of GLY increased, the tensile strength decreased. The maximum reduction observed for the GLY-25 as %50. The reduction of tensile strength is the result of the plasticization effect of GLY which destruct the hydrogen bonds and crystalline region in the film structure and resulted reduced the film strength and hardness too. The plasticizing ability of GLY may be the result of asymmetry and branched OH groups that increase the free volume [10,26,27]. Similar plasticizer effect was also observed different studies in the literature for the sodium caseinate [25], PVA-GLY [26], PVA-Sorbitol [27], PVA/SPI film [12] and sodium caseinate/GLY films [9].
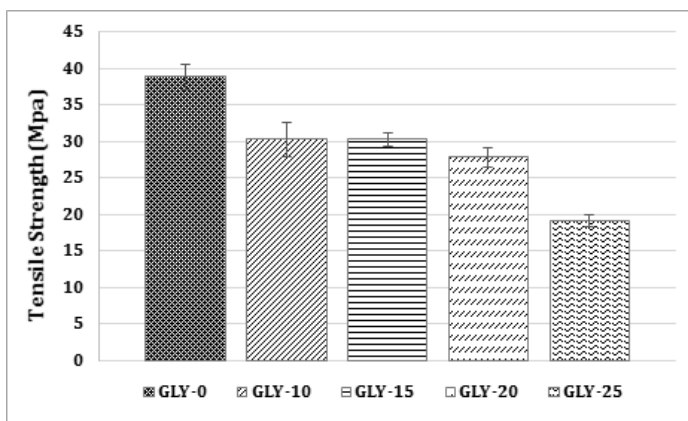
Fig. 3 Tensile strength values of the PVA/CAS films with different GLY amount

The percentage elongation value gives the information about the stretching capacity of the films. It is defined as maximum elongation a material can sustain before breaking [28]. Fig. 4 shows the elongation values (%) of the films as a function of GLY amount. The elongation value of GLY-0 was measured as 207%. With the increase of GLY percentage, the elongation prominently enhanced. The maximum increment was seen at GLY-15 as 36%. The GLY addition destruct the hydrogen bonds and increase the chain mobility and also free volume of PVA. And also decreases the interaction between the protein chains CAS. Eventually, flexibility of the films increases.
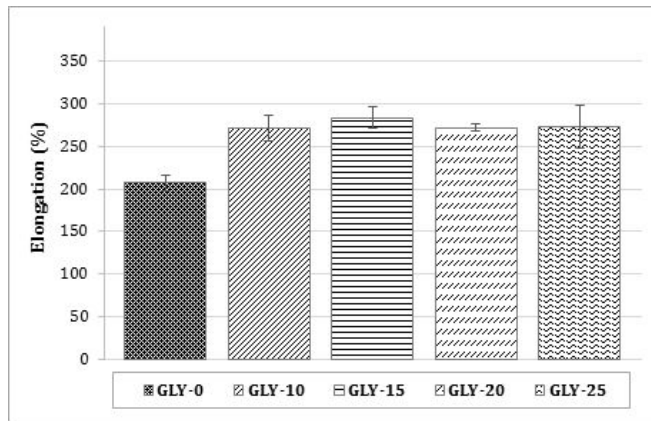
Fig. 4 Elongation values of the PVA/CAS films with different GLY amount

3.3. Contact Angle

The surface hydrophilicity-hydrophobicity characteristics of the films can be directly determined with the water contact angle (θ). The contact angle values of hydrophilic films are $0<\theta<90$. The hydrophobicity increased with the increasing θ value [29].
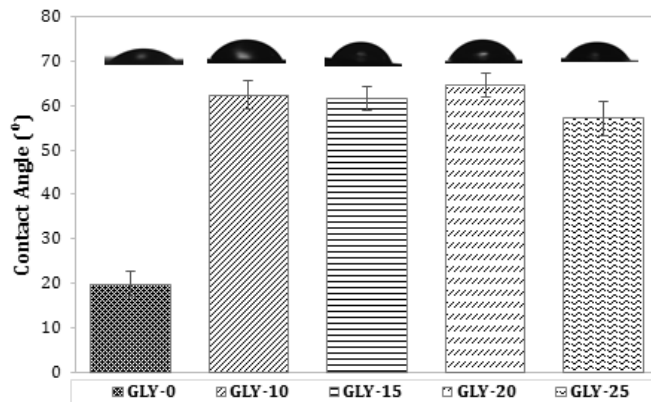
Fig. 5 The water contact angle values of the films

The water contact angle values of each film surface were illustrated in Fig. 5. All films exhibited hydrophilic character ($\theta<70$). The unplasticized GLY-0 film has lowest θ value as $19°$ and this value increased with the addition of glycerol about % 65-70. The maximum contact angle was observed for the GLY-20 sample. The hydrophilic groups such as hydroxyl on the film surface, impurity and roughness of the surface affect the contact angle of the materials [15] . The increasing of contact angle by increasing GLY content may be due to the consumption of hydrophilic –OH groups on the film surface. The FTIR spectra of the samples support this result. A plasticizer decreased the number of free –OH group in the structure which causes decreasing the hydrogen bonds between the PVA and water molecules [27]. The contact angle values of PVA/CAS/GLY blends are higher than in the ported biodegradable film studies on the literature. According to Su et al., the θ values of soy protein isolate/PVA/GLY films are lower than $50°$ [17].

3.4. Thermogravimetric Analysis (TGA)

The thermal properties of the samples were determined with TGA. The thermal stability of the polymers is related with the degradation of macromolecules and low molecular weight molecules for a specific time and temperature. The stability of these molecules depends on the interactions like hydrogen, van der Waals bonds, dipole dipole. When the thermal energy given to the material is higher than the bond energy, chain scission and bond dissociations of related bonds begin [26,30].

The results of studied samples were given in Fig. 6 and Table 2. As illustrated in Fig. 6 all samples exhibited multiple degradation. This is explained by the presence of several molecular weight molecules. The first degradation stage was shown in the range of 110-121 $^{\circ}$C for all samples. This weight loss is assignable to the water or moisture vaporization from the film structure [18,30] . Biranje et al. reported that the PVA/CAS blends exhibited initial weight loss about 100 $^{\circ}$C due to the hydrophilic structure of the films. $T_{onset-1}$ value of the pure PVA is 113.8 $^{\circ}$C which increased with the incorporation of casein in the structure to 121.6 $^{\circ}$C. After that $T_{onset-1}$ value of GLY-0 decreased with the increasing content of GLY. The second weight loss was started at 335 $^{\circ}$C for the pure PVA due to the main polymer chain scission and acetate group decomposition. This is followed by a third smaller weight loss approximately at 395 $^{\circ}$C due to the decomposition of polymer backbone [27]. As for the GLY-0 blend film $T_{onset-2}$ decreased to the 287 $^{\circ}$C and this reduction continued with increasing GLY content according to data listed in Table 2. This may be due to the plasticizing effect of GLY and the boiling point of GLY is about 290 $^{\circ}$C. GLY might have been eliminated from the film structure about this temperature. On the other hand, the residual weight of pure PVA was 0.75% and it increased with the addition of casein to the 7.7%. However, this value decreased by adding GLY. The minimum residual weight at 500 $^{\circ}$C was observed for the GLY-25 film. So, GLY accelerated the degradation of the films.
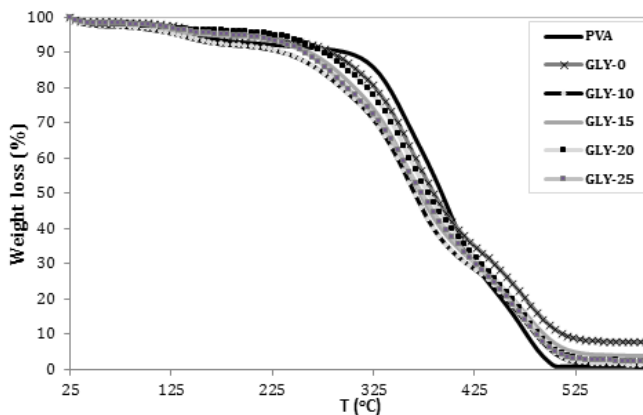
Fig. 6 TGA curves of the samples

Table 2 Thermal properties of the films obtained from TGA

Samples	$T_{onset-1}$ (°C)	$T_{endset-1}$ (°C)	$T_{onset-2}$ (°C)	$T_{endset-2}$ (°C)	T_{max} (°C)	Residue $_{500\,°C}$ (wt%)
PVA	113.8	159.9	335.0	504.1	398.3	0.75
GLY-0	121.6	158.3	300.1	508.3	362.6	7.7
GLY-10	120.8	163.1	279.4	496.9	358.4	1.2
GLY-15	114.7	142.7	277.6	502.2	358.8	3.8
GLY-20	113.5	126.3	275.7	495.2	357.6	2.4
GLY-25	110.2	141.8	266.4	479.5	357.6	0.75

3.4. Water Vapor Permeability (WVP)

The WVP is the amount of the transferred vapor between the film and ambient. It is important property which determines the usage are of the films and product shelf-life of the packaged material. The water vapor barrier property of the films depends on several factors such as ambient conditions, thickness, the composition of the structure and crystallinity of the polymer [3,15]. The hydrophilic-hydrophobic nature of the materials controls the barrier properties. PVA is the water soluble, hydrophilic polymer and casein is also hydrophilic structure. Thus, their WVP is higher than the other polymers. The hydrophilic polar groups interact with the water and causes increased permeability [3,17].

The WVP values of selected films were given in Table 3. The water barrier property of the pure PVA is higher than CAS. The blend film (GLY-0) exhibited lower WVP than both of components PVA and CAS as 6.413×10^{-11} g m^{-1} s^{-1} Pa^{-1}. This may be due to the interaction (hydrogen bonds) between the casein and PVA molecules. By contrast, the WVP value of the PVA-CAS film increased to 7.798×10^{-11} g m^{-1} s^{-1} Pa^{-1} for the GLY-25. It was because plasticization effect of GLY. The film structure has become more porous and hydrophilic. Also, the plasticizers increase the free volume of the polymer matrix and protein network [6]. By increasing free volume and pore size of the film, water molecules can permeate easily in the structure. Wagh et al. reported that, the WVP values of casein and whey protein concentrate films increased with the increasing plasticizer content [6].

Table 3 The WVP values of selected films

Samples	Water Vapor Permeability g m^{-1} s^{-1} Pa^{-1} (x 10^{-11})
PVA	13.288
CAS	10.971
GLY-0	6.413
GLY-25	7.798

4. Conclusions

The development of new biodegradable materials instead of petroleum-based products attracts attention with the increased sensitivity to health and environmental problems. The milk protein casein and biodegradable synthetic polymer PVA blend films were produced by using solution casting method in our study. To improve the mechanical properties of the films glycerol was used as plasticizer at different concentrations.

The FTIR results indicated that there were interactions between the components via hydrogen bonding due to the hydroxyl groups. The tensile strength decreased by increasing GLY content. The flexibility of the films developed with the addition of GLY. The maximum increment was observed for the GLY-15 film as 33%. The TGA gave the

information about the thermal properties of the films. It was showed that all films exhibited multiple degradation stage. Firstly, the water in the structure was eliminated about 110 $^{\circ}$C and then polymer chain scissions and degradations occurred. The $T_{onset-1}$ value decreased with the increasing content of GLY. Also, it was observed that the GLY accelerated the degradation of the PVA-CAS films. The contact angle values revealed that the all films were hydrophilic because of hydrophilic nature of the components. The WVP property were enhanced by adding GLY. Based on the data obtained from this study, it is planned to perform cross-linking to these films in order to further improve the properties of the films.

References

[1] Gómez-Estaca BJ, Gavara R, Catalá R, Hernández-Mu-oz P. The Potential of proteins for producing food packaging materials: A review. Packaging Technology and Science, 2016;29(May):203–224. https://doi.org/10.1002/pts.2198

[2] Abdul Khalil HPS, Banerjee A, Saurabh CK, Tye YY, Suriani AB, Mohamed A, Karim AA, Rizal S, Paridah MT. Biodegradable Films for Fruits and Vegetables Packaging Application: Preparation and Properties. Food Engineering Reviews, 2018;10(3):139–153. https://doi.org/10.1007/s12393-018-9180-3

[3] Abdullah ZW, Dong Y, Davies IJ, Barbhuiya S. PVA, PVA blends and their nanocomposites for biodegradable packaging application. Polymer-Plastics Technology and Engineering, 2017;56(12):1307–1344. https://doi.org/10.1080/03602559.2016.1275684

[4] Pan Y, Farmahini-Farahani M, O'Hearn P, Xiao H, Ocampo H. An overview of bio-based polymers for packaging materials. Journal of Bioresources and Bioproducts, 2016;1(3):106–113.

[5] Limpan N, Prodpran T, Benjakul S, Prasarpran S. influences of degree of hydrolysis and molecular weight of poly (vinyl alcohol) (PVA) on properties of fi sh myo fi brillar protein / PVA blend fi lms. Food hydrocolloids, 2012;29:226–233. https://doi.org/10.1016/j.foodhyd.2012.03.007

[6] Wagh YR, Pushpadass HA, Emerald FME, Nath BS. Preparation and characterization of milk protein films and their application for packaging of Cheddar cheese. Journal of Food Science and Technology, 2014;51(12):3767–3775. https://doi.org/10.1007/s13197-012-0916-4

[7] Juvonen H, Smolander M, Boer H, Pere J, Buchert J, Peltonen J. Film formation and surface properties of enzymatically crosslinked casein films. Journal of Applied Polymer Science, 2010;119:2205–2213. https://doi.org/10.1002/app.32943

[8] Bonnaillie LM, Zhang H, Akkurt S, Yam KL, Tomasula PM. Casein films: The effects of formulation, environmental conditions and the addition of citric pectin on the structure and mechanical properties. Polymers, 2014;6(7):2018–2036. https://doi.org/10.3390/polym6072018

[9] Chen H. Formation and Properties of Casein Films and Coatings. In: Protein-based films and coatings. Gennadios A, editor. USA: CRC Press; 2003. 181–209, ISBN 978-1-4200-5962-5

[10] Audic JL, Chaufer B. Influence of plasticizers and crosslinking on the properties of biodegradable films made from sodium caseinate. European Polymer Journal, 2005;41(8):1934–1942. https://doi.org/10.1016/j.eurpolymj.2005.02.023

[11] Dominguez-Martinez BM, Martínez-Flores HE, Berrios JDJ, Otoni CG, Wood DF, Velazquez G. Physical Characterization of Biodegradable Films Based on Chitosan, Polyvinyl Alcohol and Opuntia Mucilage. Journal of Polymers and the Environment, 2017;25(3):683–691. https://doi.org/10.1007/s10924-016-0851-y

[12]   Su J, Huang Z, Liu K, Fu L, Liu H. Mechanical properties , biodegradation and water vapor permeability of blend films of soy protein isolate and poly (vinyl alcohol) compatibilized by glycerol. Polymer Bulletin, 2007;58:913–921. https://doi.org/10.1007/s00289-007-0731-7

[13] Lara BRB, Araújo ACMA, Dias MV, Guimarães M, Santos TA, Ferreira LF, Borges SV. Morphological, mechanical and physical properties of new whey protein isolate/ polyvinyl alcohol blends for food flexible packaging. Food Packaging and Shelf Life, 2019;19:16–23. https://doi.org/10.1016/j.fpsl.2018.11.010

[14]   Monjazeb Marvdashti L, Koocheki A, Yavarmanesh M. Alyssum homolocarpum seed gum-polyvinyl alcohol biodegradable composite film: Physicochemical, mechanical, thermal and barrier properties. Carbohydrate Polymers, 2017;155:280–293. https://doi.org/10.1016/j.carbpol.2016.07.123

[15] Ma Q, Du L, Yang Y, Wang L. Food hydrocolloids rheology of fi lm-forming solutions and physical properties of tara gum fi lm reinforced with polyvinyl alcohol (PVA). Food hydrocolloids, 2016;63:677–684. https://doi.org/10.1016/j.foodhyd.2016.10.009

[16]   Gaikwad KK, Lee JY, Lee YS. Development of polyvinyl alcohol and apple pomace bio-composite film with antioxidant properties for active food packaging application. Journal of Food Science and Technology, 2016;53(3):1608–1619. https://doi.org/10.1007/s13197-015-2104-9

[17] Su J, Huang Z, Zhao Y, Yuan X, Wang X, Li M. Moisture sorption and water vapor permeability of soy protein isolate / poly (vinyl alcohol)/ glycerol blend films. Industrial Crops and Products, 2010;31:266–276. https://doi.org/10.1016/j.indcrop.2009.11.010

[18] Biranje S, Madiwale P. Porous electrospun casein / PVA nanofibrous mat for its potential application as wound dressing material. Journal of Porous Materials, 2018, https://doi.org/10.1007/s10934-018-0602-7

[19]   Xie J, Hsieh Y. Ultra-high surface fibrous membranes from electrospinning of natural proteins : casein and lipase enzyme. Journal of Materials Science, 2003;8:2125–2133. https://doi.org/10.1023/A:1023763727747

[20] Alper A, Ilberg V. Effect of different polyol-based plasticizers on thermal properties of polyvinyl alcohol : starch blends. Carbohydrate Polymers, 2016;136:441–448. https://doi.org/10.1016/j.carbpol.2015.08.093

[21]   Saez-Orviz S, Laca A, Díaz MRM. Approaches for casein film uses in food stuff packaging. Afinidad, 2016;74(577):26–29 .

[22] Gurgel M, Vieira A, Altenhofen M, Oliveira L, Beppu MM. Natural-based plasticizers and biopolymer films : A review. European Polymer Journal, 2011;47(3):254–263. https://doi.org/10.1016/j.eurpolymj.2010.12.011

[23] Orsuwan A, Sothornvit R. Effect of banana and plasticizer types on mechanical, water barrier, and heat sealability of plasticized banana-based films. Journal of Food Processing and Preservation, 2018;42(1):1-8. https://doi.org/10.1111/jfpp.13380

[24] Tian H, Guo G, Xiang A, Zhong WH. Intermolecular interactions and microstructure of glycerol-plasticized soy protein materials at molecular and nanometer levels. Polymer Testing, 2018;67197–204. https://doi.org/10.1016/j.polymertesting.2018.03.002

[25]   Talens P, Chiralt A, Jose M. Tensile properties and water vapor permeability of sodium caseinate films containing oleic acid – beeswax mixtures. Journal of Food Engineering, 2008;85:393–400. https://doi.org/10.1016/j.jfoodeng.2007.07.022

[26] Mohsin M, Hossin A, Haik Y. Thermal and mechanical properties of poly (vinyl alcohol) plasticized with glycerol. Journal of Applied Polymer Science, 2011;122:3102–109. https://doi.org/10.1002/app.34229

[27] Tian H, Liu D, Yao Y, Ma S, Zhang X, Xiang A. Effect of sorbitol plasticizer on the structure and properties of melt processed polyvinyl alcohol films. Journal of Food Science, 2017;82(12):2926:2935.

[28] Brzoska N, Müller M, Nasui L, Schmid M. Effects of film constituents on packaging-relevant properties of sodium caseinate-based emulsion films. Progress in Org, 2018;114:250–258. https://doi.org/10.1016/j.porgcoat.2017.10.016

[29]   Cao L, Liu W, Wang L. Developing a green and edible film from Cassia gum: The effects of glycerol and sorbitol. Journal of Cleaner Production, 2018;175:276–282. https://doi.org/10.1016/j.jclepro.2017.12.064

[30] Sirocic AP, Krehula LK, Katancic Z, Hrnjak-Murgic Z. Characterization of casein fractions – comparison of commercial casein and casein extracted from cow's milk. Chemical and Biochemical Engineering Quarterly Journal, 2017;30(4):501–509. https://doi.org/10.15255/CABEQ.2015.2311

Production and characterization of ternary sheep hydroxyapatite (SHA)-wollastonite (W)-commercial inert glass (CIG) biocomposite

Nermin Demirkol[*,a,1,2], Merve Turan[b,2]

[1]*Ceramic, Glass & Tile Program, Kocaeli University, Kocaeli, Turkey*
[2]*Department of Biomedical Engineering, Kocaeli University, Kocaeli, Turkey*

Article Info	Abstract
	Hydroxyapatite [HA] is the most widely accepted biomaterial for the repair and reconstruction of bone tissue defects. It has all the characteristic features of biomaterials such as biocompatible, bioactive, osteoconductive, nontoxic, non-inflammatory and non-immunogenic properties. It has low mechanical properties for load bearing applications. HA must be reinforced with other ceramics or metals to produce more load resistible composites. HA also can be produced from natural materials such as bovine, sheep, chicken, human bones, fish bones with simple calcination method. In this study, 5 wt% wollastonite and 5 wt% commercial inert glass were added to sheep hydroxyapatite together to improve mechanical properties. Mechanical properties of composite increased with increasing sintering temperature. The highest Vickers microhardness and compression strength values were obtained with SHA-5 wt% wollastonite- 5 wt% CIG composite sintered at 1300ºC as 197 HV and 94 MPa, respectively.

1. Introduction

Hydroxyapatite [HA; $Ca_{10}(PO_4)_6(OH)_2$] is biocompatible and bioactive material. It is replaced over a period of time. HA and its composites due to their absorption ability and biocompatibility are of interests for application in medicine [1,2]. However, the mechanical properties of HA are not good enough to be used as an implant in load-bearing applications. There have been many investigations aimed at improving the mechanical properties of HA, like preparing them as composite materials. Addition of second phase ceramic materials (e.g. alumina, titania) into HA matrix for enhancing strength has been an interesting research field in recent years. Wollastonite ($CaSiO_3$) generally has been used as a reinforcement phase to produce composites with improved mechanical properties. It has also been used as a biomaterial for artificial bones and dental roots because of its good biocompatibility and bioactivity [3].

Demirkol [4] examined the physical and mechanical properties of hydroxyapatite-wollastonite-titania composites. Lin [5] et. all. worked on fabrication and characterization of hydroxyapatite/wollastonite composite bioceramics with controllable properties for tissue repair. In their study, the hydroxyapatite/wollastonite ($Ca_{10}(PO_4)_6(OH)_2/CaSiO_3$, HA/CS with different weight ratio were fabricated. The effects of composite ratio on sintering behavior, microstructure, mechanical properties, bioactivity, degradability behavior and the bone marrow mesenchymal stem cells (MSC) response to the composites were investigated. When the weight ratio of CS increased, the linear shrinkage of the

ceramics decreased, while the porosity increased. Due to high porosity, mechanical properties of composite decreased. Harabi et.all. [6] prepared highly resistant wollastonite bioceramics using local raw materials. In their study, wollastonite-based ceramics were obtained by solid state reaction. The starting powders were sintered at different temperatures (850-1250°C) for 2 h. Moreover, different amounts of B_2O_3 (0.5-5.0 mass %) have been added. A relative density of about 97% of the theoretical was reached for samples sintered at 1050°C for 2 hours, containing 3 and 5 mass % B_2O_3. Excellent values of both three-point flexural strength (343±34 MPa) and micro hardness (4.8 GPa) for samples containing 5 mass % B_2O_3 sintered at 1050°C for 2 h. Besides this a relatively low mass loss ratio has been measured (1.1 %) for wollastonite samples containing 5 mass % B_2O_3, sintered under the same conditions, after soaking in lactic acid for 9 days. Finally, the bioactivity of wollastonite by the possibility of formation of apatite on the surface of wollastonite immersed in simulated body fluid was confirmed.

Glass compositions would be a good idea for doping apatite matrix. Demirkol [7] et. all. investigated influence of commercial inert glass addition on the mechanical properties of commercial synthetic hydroxyapatite (CSHA). In their study, CSHA powders were mixed with 5 and 10 wt.% CIG separately. The powder portions were pressed at 350 MPa between hardened steel dies. Pressed samples were sintered between 1000°C and 1300°C for 4 h. The physical and mechanical properties were determined by measuring density, compression strength, the Vickers microhardness. Structural characterization was carried out with X-ray diffraction and scanning electron microscopy studies. The highest mechanical properties and the highest density were obtained in CSHA-5 wt.% CIG composite sintered at 1300°C. Rocha [8] et. all. worked on production and characterization of hydroxyapatite/niobo phosphate glass scaffold for bone repair. The scaffolds were produced by hydrothermal deposition of monetite on polyurethane sponge substrates, further converted to hydroxyapatite in an alkali solution. In their study, after heat treatment, elimination of the organic sponge provides a three-dimensional (3D) structure. Niobo-phosphate glasses were added to the heat treated struts and the scaffolds were sintered. The samples incorporated with niobo phosphate glass showed a higher densification of the interconnections, when compared to samples without glass. This result may determine the development of an interface more resistant to the forces subjected on these scaffolds. Salman [9] et. all. investigated the sintering effects and mechanical properties of bovine hydroxyapatite-commercial inert glass composites. In their study, bovine hydroxyapatite containing 5 wt% CIG and 10 wt% CIG biocomposites were produced at different sintering temperatures, separately. Addition of glass components into the HA structure in small quantities is very popular for improving sinterability and improving the mechanical performance of HA biomaterials.

The objective of this study was to produce and to characterize ternary sheep hydroxyapatite (SHA)-wollastonite (W)-commercial inert glass (CIG) biocomposite for orthopedical applications.

2. Materials and Methods

In this study, materials and methods part includes experimental studies and characterization of ternary sheep hydroxyapatite (SHA)-wollastonite (W)-commercial inert glass (CIG) biocomposite.

2.1. Experimental Studies

The SHA used in this study was prepared from calcinated sheep bones. Firstly, fresh cut femurs were deproteinized with NaOH and after reirrigation the samples were subjected to calcination at 750°C. Then calcinated sheep bones were wet ball milled for 24 hours and they were dried at the drying oven. Mean particle size of obtained SHA powders were 10 µm. The SHA powder was mixed with 5 wt% wollastonite (W) and 5 wt% commercial inert glass (CIG) for 4 h together. Used wollastonite was obtained from Eczacibasi Company. The samples were prepared according to a British Standard for compression tests. The samples were pressed at 350 MPa because this is a British standard for the preparing mechanical test samples for bioceramic and ceramic materials (BS 7253) [10]. The powder portions were pressed at 350 MPa between hardened steel dies. Pressed samples sintered at different temperatures between 1000°C and 1300°C (with the heating rate of +5°Cmin^{-1}) for 4 h (Ozmak Furnaces, Istanbul, Turkey). According to my former studies and some literatures 4 hours sintering time is sufficient and suitable for this kind of biocomposite materials [7, 9].

2.2. Characterization

Chemical analysis of used commercial inert glass was determined by XRF. Compression strength, Vickers microhardness, as well as density were measured. The density of composites was gauged with the Archimedes method. Scanning electron microscopy (SEM) was used to characterize the microstructure of the composite. Scanning electron microscopy (SEM) images were taken with scanning electron microscope (FEI NovaNanoSEM650 attached with EDAX Tridient System). The compression tests were done with a universal test apparatus, at the crosshead speed of 3 mm/min. Microhardness values were determined under 200 g load for 15 s (HMV Shimadzu JP).

3. Results and Discussion

Table 1 Chemical Analysis of Used Commercial Inert Glass (CIG).

Oxide	wt%	Oxide	wt%
SiO_2	68.80	TiO_2	0.017
Na_2O	17.02	Al_2O_3	2.15
CaO	9.25	Cr_2O_3	0.012
MgO	1.77	CuO	0.0036
Fe_2O_3	0.084	Others	Trace

Table 1 shows the chemical analysis results of used commercial inert glass (CIG). Quartz is the major element as expected. Used CIG is typically soda lime silica window glass.
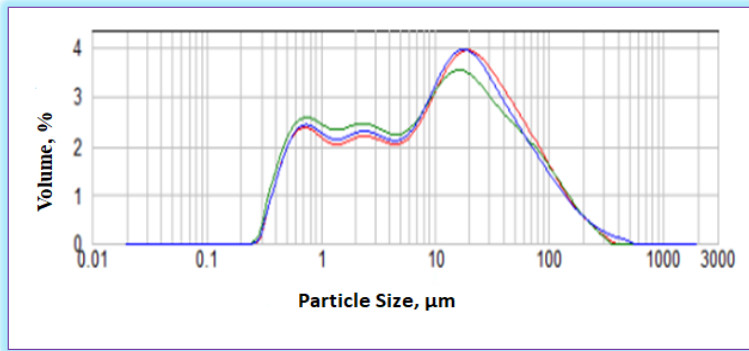
(a)
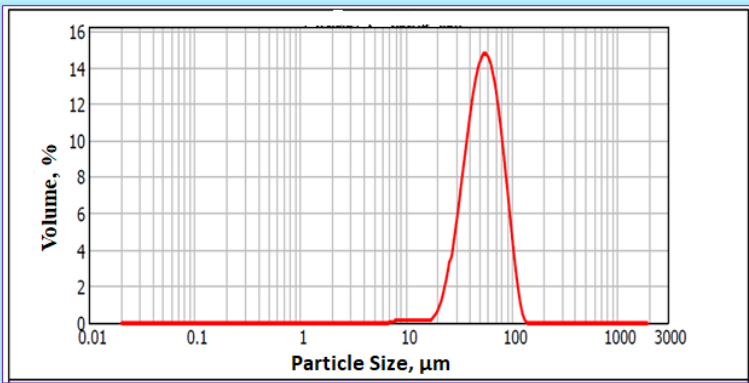
(b)
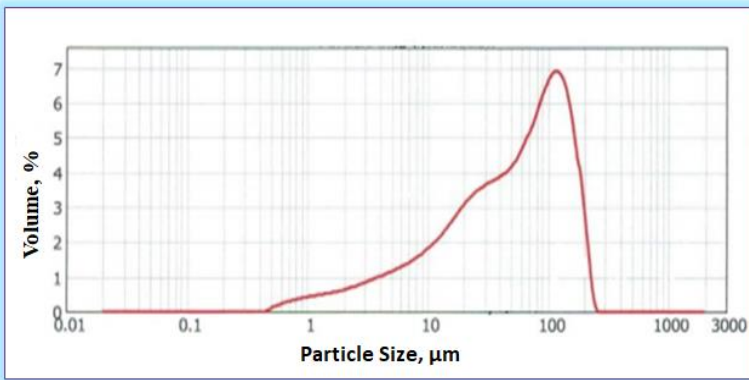
(c)

Fig. 1 Particle size distribution of (a) used sheep hydroxyapatite(SHA) (b) used
wollastonite (W) (c) used commercial inert glass (CIG) [11].

Figure 1 exhibits the particle size distribution of used raw materials in this study. Demirkol
[11] determined the mean particle sizes of used raw materials in her former study. The

mean particle sizes of sheep hydroxyapatite, wollastonite and commercial inert glass are 10, 65 and 68 μm, respectively.

Table 2 Density, compression strength and Vickers microhardness results of SHA-5W5CIG biocomposite sintered at different temperatures.

Sintering Temperature (°C)	Density (g/cm³)	Compression Strength (MPa)	Vickers Microhardness (HV)
1000	2,38±0,05	58±8,10	77±4,81
1100	2,57±0,11	72±5,70	101±5,75
1200	2,73±0,22	81±9,93	181±8,93
1300	2,81±0,15	94±4,88	197±9,97

Table 2 summarizes the experimental results of density, compression strength and the Vickers microhardness of the samples sintered at different temperatures.

Density, compression strength and Vickers microhardness values increased with increasing sintering temperatures. As seen as also Bulut [12] et. all.'s study with increasing sintering temperature, the density of the composite increased while their porosity decreased. The highest density, compression strength and Vickers microhardness values were obtained with SHA-5W5CIG biocomposite sintered at 1300°C as 2,81 g/cm³, 94 MPa and 197 HV, respectively.

(a)   (b)
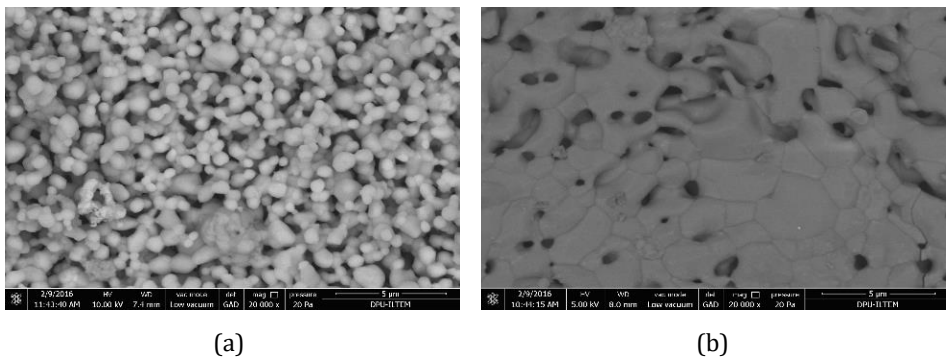
Fig 2. SEM micrographs of SHA-5W5C biocomposite sintered at (a) 1000°C and (b) 1300°C

Figure 2 exhibits the scanning electron microscopy photos of SHA biocomposites containing 5 wt% wollastonite and 5 wt% commercial inert glass (SHA-5W5C) sintered at 1000 and 1300°C.

When Figure 2a compared with Figure 2b, grain growth occurred and amount of porosity is also decreased with increasing sintering temperature. The composite sintered at 1300°C is more compact than the composite sintered at 1000°C.

Bulut [12] et. all investigated biocompatibility of hydroxyapatite-alumina and hydroxyapatite-zirconia composites including commercial inert glass (CIG) as a ternary component. In their study, grain growth occurred with increasing sintering temperature similar to this study.

(a)

(b)

(c)
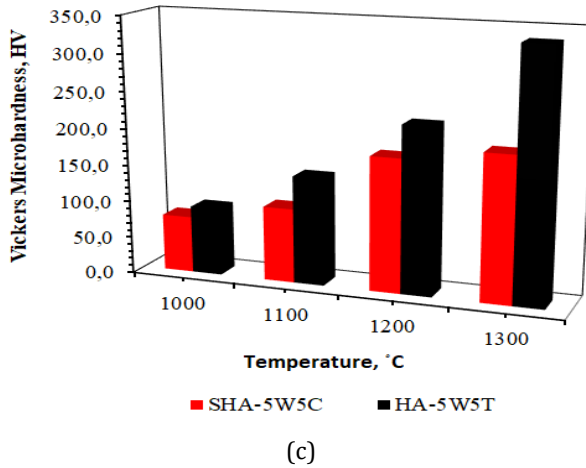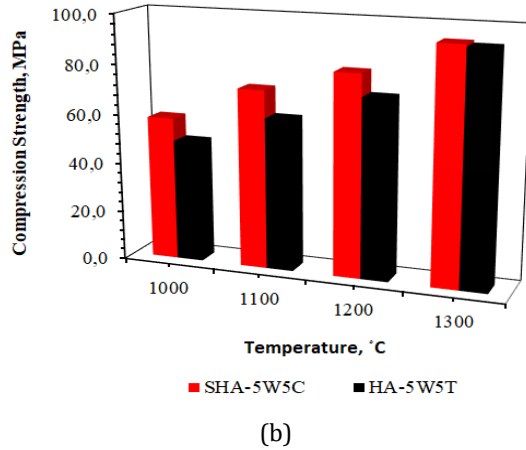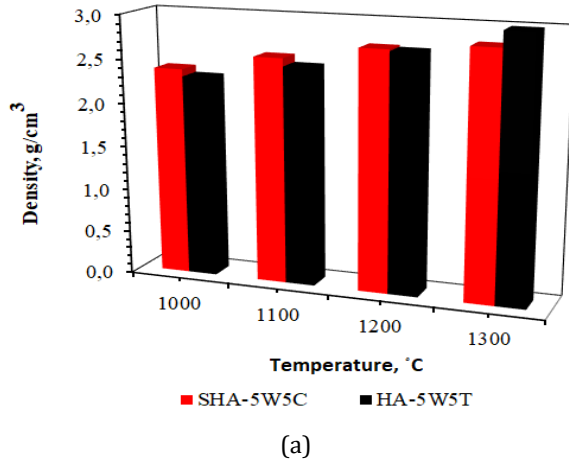
Fig 3. Comparison of (a) density (b) compression strength (c) Vickers microhardness of SHA-5W5C and HA-5W5T composites sintered at different temperatures

Demirkol [4] investigated physical and mechanical properties of commercial synthetic hydroxyapatite (CSHA)-wollastonite-titania composites. In her study, CSHA-2.5 wt% wollastonite-2.5 wt. % titania and CSHA-5 wt% wollastonite-5 wt. % titania (HA-5W5T) composites prepared and sintered at 1000-1300**°C.** The physical and mechanical properties were determined by measuring density, compression strength and Vickers microhardness (HV). Density, compression strength and Vickers microhardness results of SHA-5W5C and HA-5W5T biocomposites sintered at different sintering temperature were compared in Figure 3.

As can be seen in Fig. 3, density, compression strength and Vickers microhardness results of both composites increased with increasing sintering temperature. Both addition of 5 wt.% titania and 5 wt.% commercial inert glass to hydroxyapatite containing 5 wt.% wollastonite showed similar compression strength value with the samples sintered at 1300°C. But, Vickers microhardness values of HA-5W5T composites higher than SHA-5W5C composites for all sintering temperatures. As a result in this study, increasing the temperature resulted in higher compression strength and density for 5 wt% glass addition to SHA-W composite similar to Oktar et.all's study [13].

Titania also improves the biocompatibility properties like commercial inert glass [14].

5. Conclusion

In this experimental study; 5 wt% wollastonite and 5 wt% commercial inert glass were added to sheep hydroxyapatite together to improve mechanical properties. From the results of this study, the following conclusions can be drawn:

- Commercial inert glass (CIG) and wollastonite (W) are suitable for making hydroxyapatite biocomposite with high mechanical properties.
- Density, compression strength and Vickers microhardness values increased with increasing sintering temperature.
- Porosity level of SHA-5W5C decreased with increasing sintering temperature. The compact structure was obtained with the biocomposite sintered at 1300°C.
- The highest density, compression strength and Vickers microhardness values were obtained with SHA-5W5C composite sintered at 1300°C as 2,81 g/cm^3, 94 MPa and 197 HV, respectively.
- Addition of 5 wt.% wollastonite and 5 wt.% CIG to sheep hydroxyapatite increases the density, compression strength and Vickers microhardness values up to 8,49%, 36,23% and 19,39%, respectively.
- Addition of 5 wt% CIG to SHA-5 wt% wollastonite increases the compression strength value as well as 5 wt% titania addition to HA-5 wt% wollastonite with the composite sintered at 1300°C.
- Titania addition to hydroxyapatite- wollastonite composite increases the Vickers microhardness more than commercial inert glass (CIG) addition to hydroxyapatite-wollastonite composite.
- While wollastonite improves the mechanical properties, commercial inert glass (CIG) improves both mechanical properties and bioactivity.
- Using natural sources hydroxyapatite (sheep, fish, chicken, bovine bones etc.) is more economic than the synthetic hydroxyapatite.
- Biocompatibility studies are going on.
- Sheep hydroxyapatite-5W5C composite will be a good candidate for orthopedical applications after biocompatibility test results.

References

[1] Stipniece L. Salma-Ancane K. Putnins A. and Berzina-Cimdina L. Evaluation of Sr-and/or Mg-containing Hydroxyapatite Behavior in Simulated Body Fluid, Key Engineering Materials, 2015; 631: 61 – 66. https://doi.org/10.4028/www.scientific.net/KEM.631.61

[2] Skwarek E. Bolbukh Y. Janusz W. and Tertykh V. Hydroxyapatite Composites with Multiwalled Carbon Nanotubes. Adsorption Science & Technology, 2017; 35(5-6): 534 – 544. https://doi.org/10.1177/0263617417700637

[3] Encinas-Romero MA. Aguayo-Salinas S. Valenzuela-Garcia JL. Payan SR. and Castillon-Barraza FF. Mechanical and Bioactive Behavior of Hydroxyapatite-Wollastonite Sintered Composites. Int, J. Appl. Ceram. Technol., 2010; 7(2): 164-177. https://doi.org/10.1111/j.1744-7402.2009.02377.x

[4] Demirkol N. Physical and Mechanical Properties of Hydroxyapatite-Wollastonite-Titania Composites. Journal of Turkish Ceramic Federation, 2016; 49: 102-109.

[5] Lin K. Zhang M. Zhai W. Qu H. Chang J. Fabrication and Characterization of Hydroxyapatite/Wollastonite Composite Bioceramics with Controllable Properties for Hard Tissue Repair. Journal of the American Ceramic Society, 2011; 94(1): 99-105. https://doi.org/10.1111/j.1551-2916.2010.04046.x

[6] Harabi A. Chehlatt S. Preperation Process of a Highly Resistant Wollastonite Bioceramics Using Local Raw Materials. Journal of Thermal Analysis and Calorimetry, 2013; 111(1): 203-211. https://doi.org/10.1007/s10973-012-2242-5

[7] Demirkol N. Oktar F.N. Kayali E.S. Influence of Commercial Inert Glass Addition on the Mechanical Properties of Commercial Synthetic Hydroxyapatite. Acta Physica Polonica A, 2013; 123(2): 427-429. https://doi.org/10.12693/APhysPolA.123.427

[8] Rocha D.N. Oliveira Cruz L.R. Prado Neto J.L. Elmassalami Ayad N.M. Gobbo L.A. and Silva M.H.P. Production and Characterization of Hydroxyapatite/Niobo Phosphate Glass Scaffold. Key Engineering Materials, 2014; 587: 128-131. https://doi.org/10.4028/www.scientific.net/KEM.587.128

[9] Salman S. Oktar F.N. Gunduz O. Agathopoulos S. Ovecoglu M.L. Kayali E.S. Sintering Effect on Mechanical Properties of Composites Made of Bovine Hydroxyapatite(BHA) and Commercial Inert Glass (CIG). Key Engineering Materials, 2007; 330-332: 189-192. https://doi.org/10.4028/www.scientific.net/KEM.330-332.189

[10] British Standard Non-metallic materials for surgical implants. Part 2. Specification for

[11] Demirkol N. Production and Characterization of Sheep Hydroxyapatite Composites, Yalın Publication, 2016; 59-62.

[12] Bulut B. Erkmen Z.E. Kayali E.S. Biocompatibility of Hydroxyapatite-Alumina and Hydroxyapatite-Zirconia Composites Including Commercial Inert Glass (CIG) as a Ternary Component. J. Ceram. Sci. Tech. 2016; 07[03]: 263-276.

[13] Oktar FN. Goller G. Sintering Effects on Mechanical Properties of Glass-Reinforced Hydroxyapatite Composites. Ceramics International. 2002; 28: 617-621. https://doi.org/10.1016/S0272-8842(02)00017-2

[14] Sidane D. Rammal H. Beljabbar a. Gangloff S.C. Chicot D. Velard F. Khireddine H. Montagne A. Kerdjoudj H. Biocompatibility of Sol-Gel Hydroxyapatite-Titania Composite and Bilayer Coatings. Materials Science and Engineering: C, 2017; 72: 650-658. https://doi.org/10.1016/j.msec.2016.11.129

Research Article

Optimum design of anti-buckling behavior of graphite/epoxy laminated composites by differential evolution and simulated annealing method

Mehmet Akçair [a,1], Melih Savran [b,1], Levent Aydın[*,c,2], Ozan Ayakdaş[d,3], Savaş Öztürk[e,4], Nilay Küçükdoğan[f,1]

[1]Department of Graduate School of Natural and Applied Sciences, Izmir Katip Çelebi University, Izmir, Turkey
[2]Department of Mechanical Engineering, Izmir Katip Çelebi University, Izmir, Turkey
[3]Department of Graduate School of Engineering and Sciences, Izmir Institue of Technology, Izmir, Turkey
[4]Department of Metallurgical and Materials Engineering, Manisa Celal Bayar University, Manisa, Turkey

Article Info	Abstract
	Stacking sequence design and optimization of 64 layered symmetric-balance graphite/epoxy laminated composite have been performed. The optimization problems aim to find the optimum stacking sequence maximizing the critical buckling load by single objective optimization approach. Differential Evolution (DE) and Simulated Annealing (SA) optimization algorithms are proposed to solve the problems. The effect of the aspect ratios (a/b) and in-plane biaxial compressive loading ratios (N_x/N_y) on critical buckling load are investigated. In order to see the effect of discrete increments of fiber orientation angle on critical buckling load, 1°, 5°, 15°, 30° and 45° fiber angle increments are also considered. The results show that (i) the proposed algorithms DE and SA exhibit comparable performance in terms of critical buckling load when compared Genetic algorithm (GA) and Generalized pattern search algorithm (GPSA), (ii) DE and SA find distinct stacking sequence configurations in terms of buckling load for the same laminated structure design problems.

1. Introduction

In recent years, laminated composites have been very popular due to their high specific modulus and high specific strength values in manufacturing industry both in high-class industries like aerospace applications and middle-class industries such as marine, automotive and military applications [1, 2]. In addition to these characteristics of the laminated structures, fiber reinforced composites have a distinctive feature that allows the structural properties of composite materials such as fiber orientation and stacking sequence to be adjusted. These distinguishing features provide great possibilities for designers as an alternative to isotropic materials. Despite all of these superior properties of these materials, there are critical problems in some specific working conditions. These special conditions can be classified as overstress, over deflection, resonant vibration, and buckling. It can be said that the determination of the buckling load capacity of the laminated composite plate under the in-plane compressive loads is very important for the design of composite structures [1, 3].

Laminated composite plates are frequently exposed to uniaxial or biaxial pressures depending on the site of use. Thin and wide composite plates are exposed to a load in the compression plane, buckling in the plate is considered a critical failure mode. Determination of the buckling load capacity under in plane biaxial compression during the design of composite plates is crucial for understanding the post-buckling behavior especially in the engineering applications such as aircraft, automotive and ships design. Many studies have been carried out in the literature to solve this problem [1, 3]. For this purpose, Chao et al. [4] studied the optimization of buckling load under uniaxial compression conditions. Erdal and Sonmez [5] determined optimum stacking sequence design of composite plate to maximize critical buckling load. Aymerich and Serra [6] maximized buckling load capacity of laminated composite plate under strength, ply-contiguity and symmetric-balance constraints. Deveci *et al.* [7] obtained optimum integer and discrete stacking sequences of laminated composite plates for maximum buckling load capacity considering Puck fiber and inter-fiber failure (IFF) criteria as nonlinear constraints. Many stochastic optimization methods have been used to optimize buckling behavior. Kim and Lee [8] reported that Genetic Algorithms (GA), Generalized Pattern Search Algorithm (GPSA), Differential Evolution (DE) and Simulated Annealing (SA) algorithms are suitable for the solution of buckling problems. Karakaya and Soykasap [9] used the GA method to maximize the critical buckling load factor of composite plates and designed optimum ones with conventional fiber angles.

In the literature, studies on optimizing the stacking sequence of laminate composites have been carried out with GPSA [9], SA [10], Scatter Search [5], Tabu Search [11], Ant Colony Optimization (ACO) [6, 12] and GA, SA [13] algorithms in order to maximize the buckling load factor.

In the present study, in order to maximize critical buckling load factor (objecitive function), single objective optimization of 64 layered symmetric-balance graphite/epoxy laminated composite plate is considered by utilizing modified version of two stochastic optimization methods: Differential Evolution and Simulated Annealing. Fiber orientations are selected as design variables. The effect of aspect ratio and loading ratios on critical buckling load are also investigated.

2. Mechanical Analysis

The used laminated composite plate is simply supported on four edge and specially orthotropic. The geometric dimension and fiber configuration of plate are length *a,* width *b*, total thickness *h* and fiber orientation angle *θ* in the *x, y, z* and *1* directions, respectively (Fig 1). The composite plate is subjected to biaxial in-plane loads per unit length N_x and N_y. The material of the composite laminated plate is assumed to be homogeneous and the layers have equal thickness. The governing equation of the buckling process based on the classical laminated plate theory for the described symmetric laminate is given as follow [14]

$$D_{11}\frac{\partial^4 w}{\partial x^4} + 2(D_{12} + 2D_{66})\frac{\partial^4 w}{\partial x^2 \partial y^2} + D_{22}\frac{\partial^4 w}{\partial y^4} = \lambda\left(N_x\frac{\partial^2 w}{\partial x^2} + N_y\frac{\partial^2 w}{\partial y^2} + N_{xy}\frac{\partial^2 w}{\partial x \partial y}\right)$$

(1)
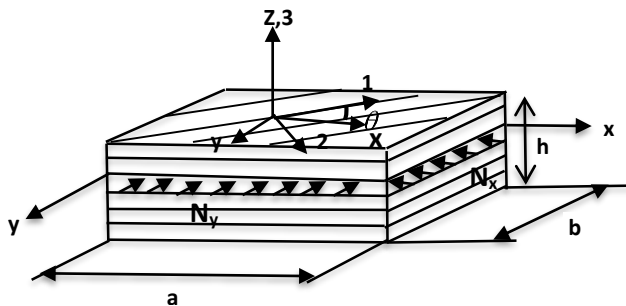
Fig. 1 Thin laminated composite plate subject to in-plane loading

where w is the deflection in the z direction and D_{ij} is the bending stiffness as

$$w(x, y) = \sum_{m=1}^{\infty} \sum_{n=1}^{\infty} A_{mn} \sin \frac{m\pi x}{a} \sin \frac{n\pi y}{b} \tag{2}$$

$$D_{ij} = \frac{1}{3} \sum_{k=1}^{N} \int_{z_k}^{z_{k+1}} \bar{Q}_{ij}^{(k)} z^2 dz \qquad i, j = 1, 2, 6 \tag{3}$$

where N is the total number of plies, k is the ply number and $\bar{Q}_{ij}^{(k)}$ is the transformed reduced stiffness of the kth layer

The boundary conditions for the simply supported plate are given as

$$w = 0 \; at \; x = 0, \; w = 0 \; at \; y = 0$$
$$M_x = 0 \; at \; x = 0, \; M_y = 0 \; at \; y = 0 \tag{4}$$

where, the moment resultants are defined as:

$$\left(M_x, M_y \right) = \int_{-h/2}^{h/2} \left(\sigma_x, \sigma_y \right) dz \tag{5}$$

where, σ_x, σ_y are the normal stress resultants in x and y directions.

For specially orthotropic laminate, the fiber configurations consist of only 0° and 90° and in this case, the element of stiffness matrix: $A_{16}=A_{26}=B_{16}=B_{26}=D_{16}=D_{26}=0$. Nemeth [15] has given the detail explanation about the usage of specially orthotropic case in composite laminates for buckling problems. If the laminated composite is not specially orthotropic, the bending–twisting terms D_{16} and D_{26} will be neglected only when the non-dimensional parameters fulfill the conditions.

$$\gamma \leq 0.2, \; \delta \leq 0.2 \tag{6}$$

where,

$$\gamma = D_{16}(D_{11}^{3} D_{22})^{-1/4}$$
$$\delta = D_{26}(D_{11} D_{22}^{3})^{-1/4} \tag{7}$$

With the substitution of Eq. (2) into Eq. (1) under Eq. (4) boundary condition, and solving eigen function problem, buckling load factor expression can be obtained as [14]

$$\lambda_b = \frac{\pi^2 \left[D_{11}\left(\dfrac{m}{a}\right)^4 + 2\left(D_{12} + 2D_{66}\right)\left(\dfrac{m}{a}\right)^2\left(\dfrac{n}{b}\right)^2 + D_{22}\left(\dfrac{n}{b}\right)^4 \right]}{N_x\left(\dfrac{m}{a}\right)^2 + N_y\left(\dfrac{n}{b}\right)^2 + N_{xy}\left(\dfrac{m}{a}\right)\left(\dfrac{n}{b}\right)} \tag{8}$$

where, m and n are integer numbers corresponding to different modes shapes; λ_b is buckling load factor; N_x and N_y are applied loads. Buckling loads are identified as $N_{xb}=N_x$ λ_b and $N_{yb}=N_y$ λ_b. Critical load factor λ_{cb} is the lowest buckling load factor, and it can be found by using appropriate combinations of m and n. For the present problem, m and n are taken to be 1 or 2, and hence the smallest of λ_b (1,1), λ_b (1,2), λ_b (2,1), λ_b (2,2) yields λ_b. Also, the critical load equals to λ_{cb} when unit loads are applied.

3. Optimization Algorithms

Optimization techniques can be divided into two main categorize as traditional and non-traditional. One of the traditional optimization techniques Lagrange Multipliers is used to find the optimum solution of only continuous and differentiable functions. Due to the fact that the design problems of the composites have discrete search spaces, the nontraditional optimization techniques can be used. In these cases, the stochastic optimization methods such as Genetic Algorithms (GA), Generalized Pattern Search Alogorithm (GPSA), Ant Colony Optimization (ACO), Differential Evolution (DE) and Simulated Annealing (SA) can be utilized. A detail explanation about stochastic optimization methods can be found in Rao [16] and in Gurdal *et al.* [17] for composite design problems and various applications. In this study, DE and SA methods are utilized to solve the defined laminated composite optimizations problems. Related parameters of the algorithms used in adjusting the options correctly are listed in Tables 1.

3.1 Differential Evolution Method

Differential Evolution is one of the stochastic optimization methods and a preferable to use in complex structured composite design problems such as a finding of critical buckling load, estimation of the natural frequency of the system and acquire the lightweight design. Differential Evolution algorithm contains the four main stages: initialization, mutation, crossover and selection as shown in Fig. 2. To find the optimum result, the effective parameters of the algorithm: scaling factor, crossover and population size. For more information about DE, can be referred to Storn and Price [18]. A population of solutions is handled instead of a single solution at each iteration in DE algorithm and also this algorithm is computationally expensive. Even if DE Algorithm is not guaranteed to find the global optima for all types of optimization problems, in some studies it is shown that it is relatively robust and efficient in finding global optimum compared to the other search techniques. In he Mathematica implementation of DE algorithm, it considers a population of r points, { $\theta_1, \theta_2,..., \theta_j,..., \theta_r$ }. It is important that r should be much greater than the number of design variables. At the iteration proses, firstly, the algorithm generates a new population that is produced by selecting random points. By introducing the real scailing factor as "*rsf*" and defining $\theta_{rsf} = \theta_w + rsf(\theta_u - \theta_v)$, ith iteration points can be obtained from the previous population. Secondly, a new point θ_{new} is established by selecting jth coordinate from θ_{rsf} with probability *P.* In Mathematica

software, P can be adjusted by the option "CrossProbability". In that step, if the constraint f(θ_{new})<f(θ_i) is valid then θ_i is taken instead of θ_{new} in the population. Stoping criteria for this process is that

(i) if the difference between the optimum output values at the new and old populations,

(ii) the difference between two (the new and old) points the new best points are less than the tolerances provided by the parameters which specifies how many effective digits of accuracy and precision should be sought in the final result.
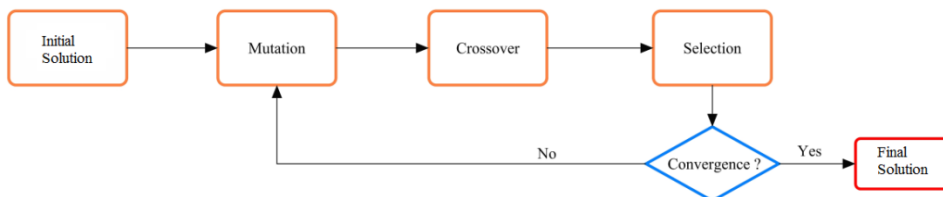
Fig. 2 Flowchart of the DE algorithm [19]

3.2 Simulated annealing

SA is the most popular search method based on the physical process of the annealing related to a metal object which is heated to a high temperature and permit to cool slowly. During the melting process, the material becomes a tougher material by means of the atomic structure settle to a lower energy state. In the optimization problems, SA algorithm can arrive at a better global optimum thanks to the annealing process allows the structure to get away from a local minimum. It is possible to solve mixed-integer, discrete, or continuous optimization problems by using SA. The main advantage related to SA is to be a talented algorithm for these problems [20].

Mathematica implementation of SA can be briefly explained as follows:

Firstly, an initial guess is introduced as θ_{in}, Secondly, a new point, θ_{new}, is produced in the neighborhood of the current point, θ at each iteration so far, θ_{best}, is also tracked. The main idea is here that the radius of the neighborhood decreases with the iteration. If

f(θ_{new}) <=f(θ_{best}), θ_{new} replaces θ_{best} and θ. Otherwise, θ_{new} replaces θ with a probability.

The distance of the new point from the current point is based on Boltzmann's probability distribution $e^{B(i,\Delta f,f_0)}$.

In this distribution "B" is the function defined by Boltzmann Exponent, i is the current iteration, Δf is the change in the fitness function value, and f0 represents the value of the objective function from the (i-1)[th] iteration. B is $\frac{-\Delta f log(i+1)}{10}$ if it is not introduced by the user. Instead of only one initial guess the Mathematica command "Simulated Annealing" uses two or more starting points. The number of initial points is given by the option Search Points, and is calculated as min (2 r, 50), where r is the number of variables.

For each starting point, this is repeated until the maximum number of iterations is reached, the method converges to a point, or the method stays at the same point consecutively for the number of iterations given by Level Iterations.
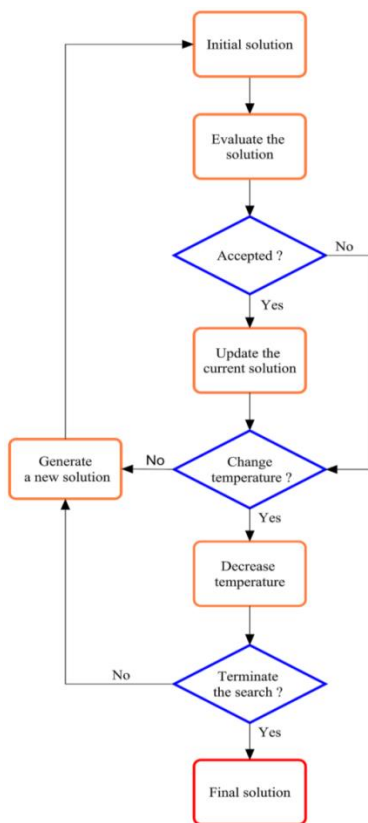
Fig. 3 Flowchart of the SA algorithm [21]

Table 1 Two optimization methods options

Options Name	DE	SA
Cross Over fractions	0.5	-
Random Seed	0	0
Scaling Factor	0.6	-
Tolerance	0.001	0.001
Mutation Fraction	0.1	-
Level Iterations	-	50
Perturbation Scale	-	1.0
Search Point	-	3000

4. Problem Definition

In this study, the optimum stacking sequence designs of 64 layered symmetric-balance graphite/epoxy laminated composite plates have been investigated. Single-objective

optimization formulation has been used for mathematical verification of model problems. The critical buckling load factor (λ_{cb}) is considered as the objective function. Fiber orientation angles of laminated composite plate are taken as discrete design variables. The optimization has been conducted for various aspect ratios (a/b) and in plane biaxial compressive loading ratios (N_x/N_y) using Differential Evolution (DE) and Simulated Annealing (SA) stochastic algorithms. In the design process, thickness of each layer is 0.127 mm and N_x has been taken as 1 N/m. N_y has been calculated from the load ratio (N_x/N_y). In Tables 2 and 3, detailed descriptions of material properties and load cases are introduced.

Table 2 The elastic properties of graphite/epoxy layers [9]

Parameters	Graphite/Epoxy
E_1, Longitudinal Modulus (MPa)	127600
E_2, Transverse Modulus (MPa)	13000
G_{12}, In-plane Shear Modulus (MPa)	6400
v_{12}, Poisson's ratio	0.3
t, Ply thickness (m)	0.127×10^{-3}

Table 3 Composite plate load cases

Load case	a (m)	b (m)	N_x (N/m)	N_y (N/m)
LC1	0.508	0.254	1	1
LC2	0.508	0.508	1	1
LC3	0.508	1.016	1	1
LC4	0.508	0.254	1	0.5
LC5	0.508	0.508	1	0.5
LC6	0.508	1.016	1	0.5
LC7	0.508	0.254	1	2
LC8	0.508	0.508	1	2
LC9	0.508	1.016	1	2

In the following part, descriptions of the model problems (problems 1 and 3) are introduced.

Problem 1

The problem given in Karakaya and Soykasap [9] and Deveci [22] is selected as benchmark. Stacking sequence design and optimization of 64 layered symmetric-balance graphite/epoxy composites are considered so as to maximize critical buckling load. The considered laminated composite plate is subjected to N_x= 1 N/m, N_y=1 N/m (LC1)and N_x= 1 N/m, N_y=2 N/m (LC9) in-plane biaxial compressive loading. Fiber orientation angles of the layers are considered in the range of 0 and 90° with 45° increments for the aspect ratio a/b=2 (LC1) and a/b=0.5 (LC9). The stochastic optimization methods DE, SA are

utilized and the performances of these methods are compared with those of Generalized Pattern Search Algorithm (GPSA) by Karakaya and Soykasap [9] and Genetic Algoritm (GA) by Karakaya and Soykasap [9] and Deveci [22] in terms of critical buckling load.

Problem 2

Organization of the problem is similar to problem 1 such that single objective optimization in order to maximize critical buckling load comprising aspect ratios a/b=2 (LC1) and a/b=0.5 (LC9) of the laminated composite plates for biaxial compressive loading $N_x= 1$ N/m, $N_y=1$ N/m (LC1) and $N_x= 1$ N/m, $N_y=2$ N/m (LC9). However, in order to see the effect of discrete increments of fiber orientation angle on the critical buckling load, 1°, 5°, 15°, 30° and 45° fiber angle increments are considered. The stochastic optimization methods DE and SA are utilized.

Problem 3

The aim of the optimization problem is to determine the effect of the aspect ratios a/b and in-plane biaxial compressive loading ratios N_x/N_y for all the cases (LC1-LC9)on critical buckling load. Fiber orientation angles of the layers are considered in the range of 0 and 90° with 5° increments. The stochastic optimization method DE is used for the optimization process.

5. Results and Discussions

In this section, the results of buckling problems (1-3) are given based on DE and SA methods. Table 4 shows the result of the Problem 1. This problem is solved to validate the proposed Differential Evolution and Simulated Annealing optimization algorithms. It is shown that DE and SA exhibit comparable performance in terms of critical buckling load when compared Generalized Pattern Search Algorithm (GPSA) by Karakaya and Soykasap [9] and Genetic Algorithm (GA) by Karakaya and Soykasap [9] and Deveci [22]. As it is seen from the results given in the Table 4 that stochastic algorithms (DE and SA) work correctly thus they have a potential to obtain reliable results for the Problems 2 and 3.

Table 4 Optimum stacking sequence designs for load cases 1 and 9 under 45° increment using DE and SA

Loading cases	Stacking sequence (DE)	Stacking sequence (SA)
LC1	$[90_8/\pm45_2/90_4/\pm45_3/\pm45_5]_s$	$[90_4/\pm45/90_6/\pm45/90_4/\pm45_2/90_4/\pm45/90_4]_s$
LC9	$[\pm45_4/0_8/0_4/\pm45_3/0_2/\pm45_2]_s$	$[0_6/90_6/90_2/\pm45/0_6/\pm45_3/90_2/0_2]_s$

Table 4 cont. Optimum stacking sequence designs for load cases 1 and 9 under 45° increment using DE and SA

Loading cases	λ_{cb} [9]	λ_{cb} [22]	λ_{cb} (Present DE)	λ_{cb}(Present SA)
LC1	695,781.3	695,663.1	695,822.2	695,822.2
LC9	132,243.5	132,237.8	132,244.6	132,232.9

Table 5 shows optimum stacking sequence designs of 64-layered symmetric-balance graphite/epoxy laminated composites for maximum critical buckling load utilizing the proposed DE algorithm. The increments of fiber orientation angles of the plies are selected as 1°, 5°, 15°, 30° and 45°. For LC1, the buckling load values of graphite/epoxy composite vary in the range of 695,822.2 and 722,978.4 N/m. The lowest buckling load value (695,822.2) of graphite/epoxy is gained for the configuration $[90_8/\pm45_2/90_4/\pm45_8]_s$ while the highest value of that (722,978.4) is obtained for the configuration $[(\pm72/\pm73)_2/\pm72_2/\pm74/\pm73/\pm72/\pm71/\pm72/\pm71/\pm74/\pm81/\pm66/90_2]_s$. For the case LC9, the buckling load values of graphite/epoxy composite vary in the range of 132,244.6 and 140,664.3 N/m. The lowest buckling load value (132,244.6) of graphite/epoxy is obtained for $[(\pm45/0_2)_4/0_4/\pm45_3/0_2/\pm45_2]_s$ while the highest value of that (140,664.3) is obtained for the configuration $[\pm27_5/\pm28/\pm27/\pm26/\pm27/\pm28/\pm27/\pm26/\pm30/\pm29/\pm23/\pm27]_s$.

The same problem (Problem 2) have also been solved by SA and the maximum critical buckling load values corresponding to stacking sequences are given in Table 6. For the case LC1, the buckling load values of graphite/epoxy composite vary between 695,822.2 and 721,500.6 N/m. Unlike DE method, the maximum critical buckling load value of graphite/epoxy composite is obtained for 5° fiber angle increment by SA. Even though the stacking sequences design of laminated composite under symmetric balance constraint based on DE and SA are different for 30° and 45° fiber angle increments, the maximum critical buckling load values are the same. When it is compared for 1°, 5° and 15° fiber angle increments, both optimum stacking sequence and critical buckling load have been found as distinct and DE gives higher critical buckling load values than that of SA.

Table 5 Optimum stacking sequence designs for load cases 1 and 9 under different fiber orientation increments using DE (D1, D2, D3, D4 and D5, correspond to 1°, 5°, 15°, 30° and 45° increments, respectively).

Loading Cases	LC1	LC9
Stacking Sequence (D1)	$[(\pm72/\pm73)_2/\pm72_2/\pm74/\pm73/\pm72/\pm71/\pm72/\pm71/\pm74/\pm81/\pm66/90_2]_s$	$[\pm27_5/\pm28/\pm27/\pm26/\pm27/\pm28/\pm27/\pm26/\pm30/\pm29/\pm23/\pm27]_s$
Stacking Sequence (D2)	$[\pm70/\pm75_2/\pm70/\pm75/\pm70_2/\pm75_2/\pm70_2/\pm75_3/\pm80/\pm50]_s$	$[\pm25_2/\pm30_2/\pm25/(\pm25/\pm30)_3/\pm30/\pm25_2/\pm30/0_2]_s$
Stacking Sequence (D3)	$[\pm75_6/\pm60/\pm75/\pm60_3/\pm75/90_8]_s$	$[\pm30_4/\pm15/\pm30/(\pm30/\pm15)_2/\pm15/\pm30_2/\pm15_2/\pm30]_s$
Stacking Sequence (D4)	$[90_2/(90_2/\pm60)_4/\pm60_3/(90_2/\pm60)_2]_s$	$[\pm30_5/0_2/\pm30_2/0_2/\pm30_2/0_4/\pm30_3]_s$
Stacking Sequence (D5)	$[90_8/\pm45_2/90_4/\pm45_8]_s$	$[(\pm45/0_2)_4/0_4/\pm45_3/0_2/\pm45_2]_s$

Table 5 cont. Optimum stacking sequence designs for load cases 1 and 9 under different fiber orientation increments using DE (D1, D 2, D3, D4 and D5, correspond to 1°, 5°, 15°, 30° and 45° increments, respectively).

Loading Cases	λ_{cb} (D1)	λ_{cb}(D2)	λ_{cb}(D3)	λ_{cb}(D4)	λ_{cb}(D5)
LC1	722,978.4	722,659.5	720,153.0	714,584.3	695,822.2
LC9	140,664.3	140,510.2	139,954.5	139,660.0	132,244.6

Table 6 Optimum stacking sequence designs for load cases 1 and 9 under different fiber orientation increments using SA. (D1, D 2, D3, D4, D5, corresponds to 1°, 5°, 15°, 30°, 45° increments, respectively)

Loading Cases	LC1	LC9
Stacking Sequence(D1)	$[\pm69/\pm73_2/90_2/\pm72/\pm78/\pm65/ \pm82/\pm62/\pm65/\pm67/\pm71/\pm76/ 90_2/\pm62/\pm63]_s$	$[\pm29/\pm27/\pm29_2/\pm28/\pm27_2/\pm20/\pm5/ \pm33/\pm10/\pm30/\pm44/\pm46/\ \pm63/\pm12]_s$
Stacking Sequence(D2)	$[\pm70_2/\pm75/\pm80/\pm75/\pm70/+80/ \pm65/\pm80/\pm60/\pm65/\pm75/\pm85/ \pm80/\pm60/\pm50]$	$[\pm25/\pm35/\pm20/\pm35/\pm30/\pm25_3/\pm20 /\pm25/\pm10/\pm30/\pm35/\pm20/ \pm15/\pm25]_s$
Stacking Sequence(D3)	$[\pm75_4/90_2/\pm75/\pm60_3/90_2/\pm60_3 /\pm75_2/\pm60]_s$	$[\pm30_5/\pm15/\pm30/\pm15_2/\pm30_2/\ \pm15_2/ 0_2/\pm75/0_2]_s$
Stacking Sequence(D4)	$[90_4/\pm60_2/90_6/\pm60_4/90_2/\pm60_3 /\ 90_2]_s$	$[\pm30_6/0_4/\pm30_2/0_2/\pm30_2/0_2/\pm30/\pm6 /0]_s$
Stacking Sequence(D5)	$[90_4/\pm45/90_6/\pm45/90_4/\pm45_2/ 90_4/\pm45/90_4]_s$	$[0_6/90_6/90_2/\pm45/0_6/\pm45_3/90_2/0_2]_s$

Table 6 cont. Optimum stacking sequence designs for load cases 1 and 9 under different fiber orientation increments using SA. (D1, D 2, D3, D4, D5, corresponds to 1°, 5°, 15°, 30°, 45° increments, respectively)

Loading Cases	λ_{cb} (D1)	λ_{cb}(D2)	λ_{cb}(D3)	λ_{cb}(D4)	λ_{cb} (D5)
LC1	721,044.0	721,500.6	719,280.4	714,584.3	695,822.2
LC9	140,013.0	139,691.0	139,734.4	139,649.0	132,232.9

In order to ensure convergence performances of the proposed algorithms, two convergence graphs have been performed and presented in Fig. 4. It is seen that both of the algorithms show good performance to reach optimum fitness values.
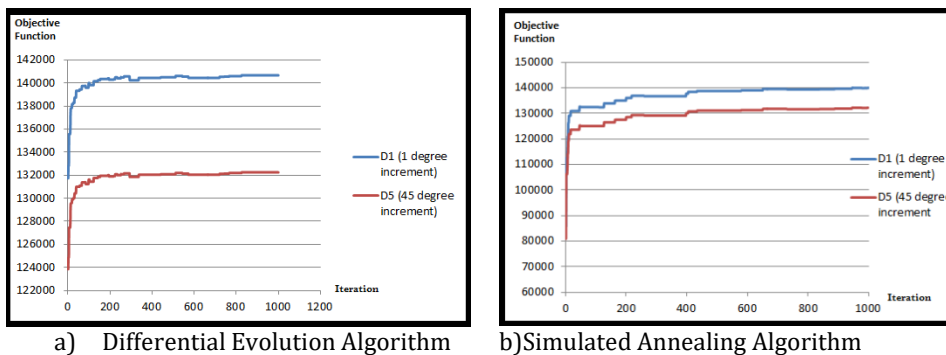
a) Differential Evolution Algorithm   b)Simulated Annealing Algorithm

Fig. 4 The convergence graphs based on DE and SA for LC9

Figure 5 shows the effect of loading cases including different aspect ratios a/b= 0.5, 1, 2 and loading ratios N_x/N_y=0.5, 1 and 2 on critical buckling load (Problem 3). According to results, it can be stated that (i) Load case 4 (a/b = 2; N_x/N_y =2) gives the highest critical buckling load, (ii) Load case 9   (a/b =0.5; N_x/N_y =0.5) gives the lowest critical buckling load, (iii) Load case 3, 6 and 8 give the approximately the same result.
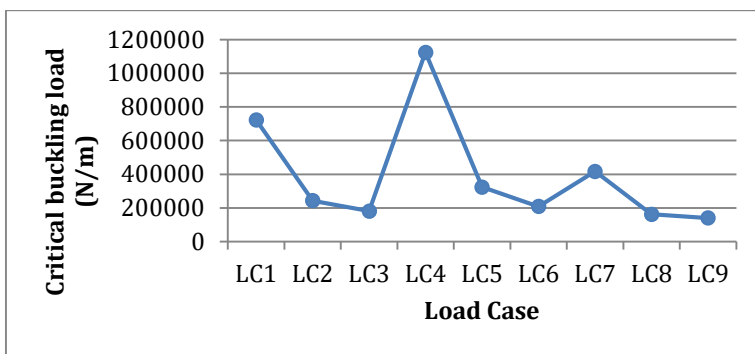
Fig. 5 The effect of load case on critical buckling load (Problem 3)

Table 7 shows the optimum stacking sequence designs of 64-layered symmetric-balance graphite/epoxy laminated composites for maximum critical buckling load utilizing the proposed DE algorithm (Problem 3). The increments of fiber orientation angles of the plies are selected as 5°. According to results, the stacking sequence configurations of laminated composite plates are obtained as $[\pm45_{16}]_s$ for LC2, LC5 and LC8 cases. It is mean that Although biaxial compressive loading ratios (N_x/N_y) are distinct for Square composite plates (a/b=1, shown in Table 3 for LC2, LC5 and LC8), stacking sequence configurations do not change.

Table 7 Optimum stacking sequence designs for load cases 1 - 9 under 5-degree fiber orientation increments using DE.

Loading Cases	Stacking Sequence	λ_{cb}
LC1	$[\pm70/\pm75_2/\pm70/\pm75/\pm70_2/\pm75_2/\pm70_2/\pm75_3/\pm80/\pm50]_s$	722,659.5
LC2	$[\pm45_{16}]_s$	242,844.4
LC3	$[\pm20_2/\pm15_5/\pm20_4/\pm15/\pm20/\pm15/\pm25/0]_s$	180,667.2
LC4	$[\pm60/\pm65/\pm60/\pm65_4/\pm60_2/\pm65_3/\pm60/\pm65_2/\pm60]_s$	1,124,072.3
LC5	$[\pm45_{16}]_s$	323,792.5
LC6	$[\pm5_2/\pm10_2/\pm5/\pm10_2/\pm5/\pm10/0_4/\pm5_2/0_6]_s$	208,273.4
LC7	$[90_2/\pm85/\pm80/\pm85_2/\pm80/\pm85_3/\pm80/90_2/\pm85_3/\pm80/90_2]_s$	416,550.6
LC8	$[\pm45_{16}]_s$	161,896.2
LC9	$[\pm25_2/\pm30_2/\pm25_4/\pm30_4/\pm25_2/\pm30/0_2]_s$	140,510.2

6. Conclusion

In this study, the optimum stacking sequence designs of 64 layered symmetric-balance graphite/epoxy laminated composite plates have been investigated using Differential Evolution (DE) and Simulated Annealing (SA) algorithms. For this reason, three optimization problems have been introduced to see the effect of different load cases (LC1-LC9) correspond to aspect ratios a/b and loading ratios N_x/N_y on critical buckling load. Also the effect of fiber orientation angle increments (1°, 5°, 15°, 30°, 45°) on buckling load are investigated. It can be concluded from the results that

- The stochastic optimization algorithms DE and SA have been performed for the same laminated composite design problems (Problem1 and Problem 2), successfully. Thus, this attempt has improved reliability and robustness of the process and also provided to avoid inherent scattering of the proposed algorithms. According to given convergence graphs, it is seen that both of the algorithms show good performance to reach optimum fitness values.
- The results based on stochastic optimization algorithms DE and SA have been compared to results given in Karakaya and Soykasap [9] by GA and GPSA methods and Deveci [22] by GA method for the same laminated composite structure design and optimization problems. Regarding the results, DE and SA show comparable performance to obtain the maximum critical buckling load.
- The critical buckling load performance of graphite/epoxy laminated composite obtained using conventional design variable (45° increment) is approximately 3.75% and 5.5% lower than that obtained utilizing 1° increment design variable for LC1 and LC9, respectively. These results are also valid for both Table 5 and Table 6.
- LC 4 (a/b=2; N_x/N_y=2) gives the highest critical buckling load and LC 9 (a/b=0.5; N_x/N_y=0.5) gives the lowest critical buckling load for 64 layered graphite/epoxy composite.

References

[1] Halpin JC. *Primer on Composite Materials Analysis (Revised),* CRC Press, Florida, NW, USA, 2017.
[2] Polat H. Turkiye Ekonomisinde Imalat Sanayi. Dicle Universitesi Iktisadi ve Idari Bilimler Fakultesi Dergisi, 2011; 1(2): 24-39.

[3] Vasiliev VV, Morozov EV. *Advanced Mechanics of Composite Materials and Structural Elements*, Elsevier, Massachusetts, MA, USA, 2013.

[4] Chao C, Koh S, Sun C. Optimization of buckling and yield strengths of laminated composites. AIAA Journal, 1975; 13(9): 1131-1132. https://doi.org/10.2514/3.60515

[5] Erdal O, Sonmez FO. Optimum design of composite laminates for maximum buckling load capacity using simulated annealing. Composite Structures, 2005; 71(1): 45-52. https://doi.org/10.1016/j.compstruct.2004.09.008

[6] Aymerich F, Serra M. Optimization of laminate stacking sequence for maximum buckling load using the ant colony optimization (ACO) metaheuristic. Composites Part A: Applied Science and Manufacturing, 2008; 39(2): 262-272. https://doi.org/10.1016/j.compositesa.2007.10.011

[7] Deveci HA, Aydin L, Artem HS. Buckling optimization of composite laminates using a hybrid algorithm under Puck failure criterion constraint. Journal of Reinforced Plastics and Composites, 2016; 35(16): 1233-1247. https://doi.org/10.1177/0731684416646860

[8] Kim C, Lee J. Optimal design of laminated composite plates for maximum buckling load using genetic algorithm. Proceedings of the Institution of Mechanical Engineers, Part C: Journal of Mechanical Engineering Science, 2005; 219(9): 869-878. https://doi.org/10.1243/095440605X31751

[9] Karakaya S, Soykasap O. Buckling optimization of laminated composite plates using genetic algorithm and generalized pattern search algorithm. Structural and Multidisciplinary Optimization, 2009; 39(5): 477-486. https://doi.org/10.1007/s00158-008-0344-2

[10] Pai N, Kaw A, Weng M. Optimization of laminate stacking sequence for failure load maximization using Tabu search. Composites Part B: Engineering, 2003; 34(4): 405-413. https://doi.org/10.1016/S1359-8368(02)00135-X

[11] Rao ARM, Arvind N. A scatter search algorithm for stacking sequence optimization of laminate composites. Composite Structures, 2005; 70(4): 383-402. https://doi.org/10.1016/j.compstruct.2004.09.031

[12] Sebaey TA, Lopes CS, Blanco N, Costa J. Ant colony optimization for dispersed laminated composite panels under biaxial loading. Composite Structures, 2011; 94(1): 31-36. https://doi.org/10.1016/j.compstruct.2011.07.021

[13] Di Sciuva M, Gherlone M, Lomario D. Multiconstrained optimization of laminated and sandwich plates using evolutionary algorithms and higher-order plate theories. Composite Structures, 2003; 59(1): 149-154. https://doi.org/10.1016/S0263-8223(02)00132-0

[14] Reddy JN. *Mechanics of Laminated Composite Plates and Shells: Theory and Analysis*, CRC Press, Florida, NW, USA, 2004. https://doi.org/10.1201/b12409

[15] Nemeth MP. Importance of anisotropy on buckling of compression-loaded symmetric composite plates. AIAA Journal, 1986; 24(11): 1831-1835. https://doi.org/10.2514/3.9531

[16] Rao SS. *Engineering Optimization: Theory and Practice*, John Wiley and Sons, New York, NY, USA, 2009.

[17] Gurdal Z, Haftka RT, Hajela P. *Design and Optimization of Laminated Composite Materials*, John Wiley and Sons, New York, NY, USA, 1999.

[18] Storn R and Price K. Differential evolution–a simple and efficient heuristic for global optimization over continuous spaces. Journal of Global Optimization, 1997; 11(4): 341-359. https://doi.org/10.1023/A:1008202821328

[19] Savran M, Aydin L. Stochastic optimization of graphite-flax/epoxy hybrid laminated composite for maximum fundamental frequency and minimum cost. Engineering Structures, 2018. 174: 675-687. https://doi.org/10.1016/j.engstruct.2018.07.043

[20] Ozturk S, Aydin L, Kucukdogan N, Celik E. Optimization of lapping processes of silicon wafer for photovoltaic applications. Solar Energy, 2018; 164: 1-11. https://doi.org/10.1016/j.solener.2018.02.039

[21] Ozturk S, Aydin L, Celik E. A comprehensive study on slicing processes optimization of silicon ingot for photovoltaic applications. Solar Energy, 2018; 161: 109-124. https://doi.org/10.1016/j.solener.2017.12.040

[22] Deveci HA. Optimum design of anti-buckling behavior of the laminated composites considering puck failure criterion by genetic algorithm. MSc Thesis, İzmir Institute of Technology, İzmir, Turkey, 34-68, 2011.

Research Article

Optimal design of the type III hydrogen storage tank for different carbon/epoxy materials by modified differential evolution method

Ozan Ayakdaş[*,a,1], Levent Aydın[b,3], Melih Savran[c,2], Nilay Küçükdoğan[d,2], Savaş Öztürk[e,4]

[1]Department of Graduate School of Engineering and Sciences, Izmir Institue of Technology, Izmir, Turkey
[2]Department of Graduate School of Natural and Applied Sciences, Izmir Katip Çelebi University, Izmir, Turkey
[3]Department of Mechanical Engineering, Izmir Katip Çelebi University, Izmir, Turkey
[4]Department of Metallurgical and Materials Engineering, Manisa Celal Bayar University, Manisa, Turkey

Article Info	Abstract
	In this study, the main objective is to minimize the failure index of a cylindrical laminated composite hydrogen storage tank under internal pressure. The first step is to obtain the distribution of stress components based on Classical Laminated Plate Theory (CLPT). The second is to evaluate the burst pressure of the tank according to three different first ply failure criteria and then to compare the results with the experimental and numerical ones from literature. In the final part of the study, the best possible combination of winding angles, stacking sequences and thicknesses of laminates satisfying minimum possible stress concentration will be obtained for different Carbon/Epoxy materials by Differential Evolution Method. The stress components and, the burst pressures reached according to Hashin-Rotem, Maximum Stress, and Tsai-Wu first-ply failure criteria, have been complied with experimental and numerical results in the literature for Type III pressure vessels. Manufacturable Type-III tank designs have been proposed satisfying the 35 MPa burst pressure for different Carbon/Epoxy materials.

1. Introduction

The world's energy requirement is largely derived from fossil resources. Today, an important part of it is fulfill with the use of sources such as nuclear, solar, wind, geothermal, biomass, glacier energies as alternatives to fossil resources. It should also be noted that the use of fossil fuels is subject to restrictions depending on environmental legislation mandates. For this reason, the use of alternative energy sources is increasing in importance and it can be said that the most important alternative energy source of the 21st century is hydrogen energy technology with high energy efficiency in low volumes [1]. Hydrogen energy technology is used in various fields such as gas plants, power plants, aviation, chemical and automotive industries. However, the most restrictive factor in the use of these energy technologies is the storage of hydrogen gas [2]. The design of composite tanks to store hydrogen gas in both high volumes and high pressures has been intensively studied in recent years [3]. For this purpose, the use of low volume and lightweight components is the most important design parameter especially in automotive

and aerospace industrial applications, hence, pressure vessels used in this area are required to have the prescribed characteristics [4].

Many researchers are investigating the design and optimization of lightweight composite pressure vessels, recently. In the literature, the design and optimization studies of the strength of composite hydrogen storage tanks have focused on laminate stacking sequence. It should be noted that the strengths of these vessels are directly related to the volumes of the fibers[5, 6]. The literature is examined, it can be seen that many studies have been made on the analysis of composite hydrogen storage tanks. For example, in Messager et al. [7], an analytical model has been built on the stacking sequence of the composite cylinders and optimization studies with Genetic Algorithm (GA) have been carried out. It has been shown that the optimization results are compatible with the experimental ones. However, they have not studied optimal design works for complex filamentary structures. Parnas and Katirci [8] obtained optimum winding angles in the production of composite pressure vessels using the Classical Laminated Plate and the Tsai-Wu failure theories. They found that the optimum fiber orientation angles were 52.1° and 54.1° according to the material type. Tabakov [9] performed a stochastic optimization study using GA to calculate the three-dimensional stress-strain in the cylindrical part of the composite pressure vessel. Exact elasticity solutions have been solved by considering the closed ends of the cylindrical shell into account. Richard and Perreux [10] have studied the problems of internal pressure single-sided composite pipe optimization. They investigated the behavior of e-glass, carbon and kevlar fiber supported composites and determined three angles 53.2°, 54.3° and 54.9°as optimum ones. Lin et al. [11] have performed optimization of the angles and thickness of composite plates using GA and Simplified Conjugate Gradient algorithms. They obtained similar results with both algorithms and determined composite layer thickness and winding angle as 1.6 mm and 36.54 °(at 489.941 MPa), respectively. Han and Chang [12] performed a failure analysis of a Type-III pressure vessels according to Hashin failure criterion and investigated stress distribution and damage conditions. They have carried out both experimental and numerical studies using carbon epoxy and have achieved coherent results. The overall structure was safe under the service conditions. Park et al. [13] studied the crack behavior in a type III high-pressure hydrogen vessel using a ply modeling method and the extended finite element method. The weak point of the composite layers has been observed in the transverse direction at the helical winding angle of 35°. In the boundary of the cylinder and dome, 35° winding angle may be important to design safety hydrogen pressure vessel.

Many studies have been also carried out on optimization of composite laminates. Nikbakta et al. [14] have achieved a review study on optimization problems of structures to improve mechanical or thermal behavior of the composites such as buckling resistance, stiffness and strength along with reducing weight, cost and stress under various types of loadings. Roque and Martins [15] carried out a study on staking sequences for maximization of the natural frequency of symmetric and asymmetric laminates by using Differential Evolution (DE). Chakraborty and Dutta [16] have studied the optimization of the weights of 3-component laminated composites with GA, which is a random search method. Jing et al. [17] investigated the composite critical buckling using with multi-criteria objective function. Similarly, Irisarri et al. [18] studied multi-objective stacking sequence optimization for composite plates. They concluded that non-traditional ply orientations may lead to better designs than classical ones. Zu et al. [19] found the best non-geodesic trajectory with GA for circular toroidal vessels. Francesco et al. [20] have worked with GA to study composite pressure vessels overwrapping a metallic liner (type III COPV) under internal pressure. They have reached the conclusion that the optimal design is first-ply or last-ply failure design objective. However, the

authors did not focus on optimum stacking sequence, which is the main motivation and contribution of the current study.

In the present study, the main purpose is to see effect of the different carbon/epoxy material type on optimum stacking sequences design of Type III pressure vessel. The first step is to gain the distribution of stress components based on Classical Laminated Plate Theory (CLPT). The second step is to determine the burst pressure of the Type III pressure vessel by using Tsai-Wu failure criterion and then to compare the result with analytical, experimental and numerical ones from literature. In the final part of the study, for different carbon/epoxy materials, the best possible combination of winding, stacking sequences and thicknesses of laminates satisfying minimum possible stress concentration have been obtained by Modified Differential Evolution (MDE) stochastic optimization method.

2. Stress Analysis of the Tank

Cylindrical part of the Type III tank is composed of isotropic metallic liner and orthotropic composite layers. The laminated composite pressure vessel having radius of "R" is subjected to the internal pressure "p". The force resultants, calculated via considerations of static equilibrium can be expressed as follow [21]:

$$N_x = \frac{1}{2}pR \qquad N_y = pR \qquad N_{xy} = 0 \tag{1}$$

For Type III pressure vessel, strain for the composite and metallic liner is assumed to be the same and also only membrane effects are considered. The stress in metallic liner and composite is related to the stiffness of each material and in the Type III analysis, the stiffness of the metallic liner and composite layer are considered together within the calculation of [A] extensional stiffness matrix.

$$A_{ij} = \sum_{k=1}^{n}[(\bar{Q}_{ij})]_k\,(h_k - h_{k-1}) + [Q_L]\,t_L \tag{2}$$

where, h_k is the distance from the middle plane to the bottom surface of the k_{th} layer, $(\bar{Q}_{ij})_k$ transformed reduced stiffness of the k_{th} layer. Q_L is stifness matrix of the metallic liner and t_L is the thickness of the liner.

By using matrix [A], the strains occurred by the loading in the cylinder, can be calculated as follow [22]:

$$\begin{bmatrix} \varepsilon_x \\ \varepsilon_y \\ \gamma_{xy} \end{bmatrix} = [A]^{-1} \begin{bmatrix} pR/2 \\ pR \\ 0 \end{bmatrix} \tag{3}$$

After the obtaining strains for laminates, and using stress-strain relationships, stress at the liner and each lamina can be written as [22]:

$$\begin{bmatrix} \sigma_x \\ \sigma_y \\ \tau_{xy} \end{bmatrix} = [Q_L] \begin{bmatrix} \varepsilon_x \\ \varepsilon_y \\ \gamma_{xy} \end{bmatrix} \tag{4}$$

$$\begin{bmatrix} \sigma_x \\ \sigma_y \\ \tau_{xy} \end{bmatrix} = [\bar{Q}]^{(k)} \begin{bmatrix} \varepsilon_x \\ \varepsilon_y \\ \gamma_{xy} \end{bmatrix} \tag{5}$$

2.1 Failure Analysis

Failure is inability of the structure against to the applied loads. The main reasons of failure can be listed as follows: (i) insufficient of the design procedure, (ii) wrong material choice, (iii) inadequate production facilities and (iv) diversity of service conditions. Many researchers have proposed the formulations for failure predictions of isotropic and anisotropic materials [23-25]. The number of the approaches and important progress clearly demonstrated that there is not any criterion universally accepted by designers as enough under various load conditions. In the present study, three failure criteria chosen from interactive, partial interactive and non-interactive failure approaches have been used for composite material design. Maximum Shear Strain Energy (Von- Mises) theory has been used for isotropic liner.

Relationships between the stress components and Von-Mises, Tsai-Wu, Hashin-Rotem and Maximum Stress failure theories can be defined as in below:

Maximum shear strain energy (Von-Mises):

σ_{yield} is the yield stress in simple tension, the theory considers the principle stresses $\sigma_1 \geq \sigma_2 \geq \sigma_3$ and point out that failure when the following equality is valid [26].

$$(\sigma_1 - \sigma_2)^2 + (\sigma_2 - \sigma_3)^2 + (\sigma_3 - \sigma_1)^2 = 2\sigma_{yield}^2 \tag{6}$$

Tsai-Wu Tensor failure criterion:

According to the theory assumption, failure occurs when the following expression is valid

$$F_1\sigma_1 + F_2\sigma_2 + F_{11}\sigma_1^2 + F_{22}\sigma_2^2 + F_{66}\tau_{12}^2 + 2\,F_{12}\sigma_1\sigma_2 = 1 \tag{7}$$

where, F_{12} can be determined with only a biaxial tension test. For calculating the value of F_{12} an empirical expression is suggested as [27]

$$F_1 = \frac{1}{(\sigma_1^T)_{ult}} + \frac{1}{(\sigma_1^C)_{ult}} \qquad , \qquad F_{11} = -\frac{1}{(\sigma_1^T)_{ult}(\sigma_1^C)_{ult}} \tag{8}$$

$$F_2 = \frac{1}{(\sigma_2^T)_{ult}} + \frac{1}{(\sigma_2^C)_{ult}} \qquad , \qquad F_{22} = -\frac{1}{(\sigma_2^T)_{ult}(\sigma_2^C)_{ult}} \tag{9}$$

$$F_{12} = -\frac{1}{2}\sqrt{F_{11}F_{22}} \qquad , \qquad F_{66} = \frac{1}{(\tau_{12}^F)_{ult}^2} \tag{10}$$

Maximum Stress criterion:

The maximum stress first ply failure criterion based on the assumption that failure is occurred if the σ_1, σ_{12} and τ_{12} reach the corresponding ultimate strength parameters of materials. There are three possible modes of failure comparing the stress components of the ply with tensile, compression and shear ultimate values.[27]

$$\sigma_1 \leq (\sigma_1^T)_{ult} \;\; , \sigma_2 \leq (\sigma_2^T)_{ult} \qquad \text{if} \qquad \sigma_1 > 0, \; \sigma_2 > 0 \tag{11}$$

$$|\sigma_1| \leq (\sigma_1^C)_{ult} \;\; , |\sigma_2| \leq (\sigma_2^C)_{ult} \quad \text{if} \qquad \sigma_1 < 0, \; \sigma_2 < 0 \tag{12}$$

$$|\tau_{12}| \leq (\tau_{12})_{ult} \tag{13}$$

Hashin - Rotem criterion:

This criterion involves two failure mechanisms which to be fiber failure and matrix failure, distinguishing between tension and compression [28].

Fiber failure in tension $(\sigma_1 > 0)$; $\sigma_1 = (\sigma_1^T)_{ult}$ $\hspace{2cm}$ (14)

Fiber failure in compression: $(\sigma_1 < 0)$; $-\sigma_1 = (\sigma_1^C)_{ult}$ $\hspace{2cm}$ (15)

Matrix failure in tension: $(\sigma_2 > 0); \left(\frac{\sigma_1}{(\sigma_2^T)_{ult}}\right)^2 + \left(\frac{\tau_{12}}{(\tau_{12})_{ult}}\right)^2 = 1$ (16)

Matrix failure in tension: $(\sigma_2 < 0); \left(\frac{\sigma_2}{(\sigma_2^C)_{ult}}\right)^2 + \left(\frac{\tau_{12}}{(\tau_{12})_{ult}}\right)^2 = 1$ (17)

3. Optimization Algorithms

Differential Evolution Method

As a stochastic optimization method, Differential Evolution (DE) enables to find alternative solution for composite design. In DE, there are four main stages: initialization, mutation, crossover, and selection. Scaling factor, crossover, and population size are three parameters checked by the algorithm, also. A population of solutions instead of a single solution at each of iteration is considered in Differential Evolution method. DE is effective in attaining global optimum avoiding local minimum of the objective function [29, 30]. However, it is computationally expensive. In the literature, DE has been investigated to design of fiber composite structures from simple rectangular plates to complex geometries [31].

4. Problem Definition

In this study, there are three different Type III Aluminum Carbon/Epoxy pressure vessel problems which have been solved; Problem 1 and 2 are verification cases and Problem 3 is an optimization problem which proposes optimum design satisfying the mentioned burst pressure. In the first step, for verification problems 1 and 2, stress components and failure index values based on Tsai-Wu, Hashin-Rotem and Maximum Stress failure theories only (which is related with burst pressure of the tank) have been calculated and then compared to experimental and Finite Element Analysis results from the literature [32, 33]. In the prediction of burst pressure and stacking optimization problems, it is focused on cylindrical parts of the pressure vessels. In these problems, Type III tanks are considered as composed of composite plies and aluminum liner (see Figure 1).

The second step is design and optimization part: overall procedures for different optimization cases can be summarized as

- Close-end cylindrical section of the Type III tanks have been only considered subjected to high internal pressure " P ".
- It is considered to be constant over the length of the cylinder for inner radius (R) thicknesses of the composite layers (t_c) and aluminum liner (t_{liner}).
- For the Problem 3, three different failure criteria to be interactive, partial-interactive and non-interactive: Tsai-Wu, Hashin-Rotem and Maximum Stress have been used as constraints.
- All optimization cases of composite cylindrical tanks have been assumed to be single objective optimization problem.
- Fiber orientation angles $\theta_1, \theta_2, \theta_3, \dots, \theta_n$ and number of layers are selected as the design variables.

Problem 1:

In the Problem 1, the stress and failure indexes of Tsai-Wu and Maximum Stress failure criteria have been computed for Type III Aluminum-Carbon/Epoxy composite pressure vessel. Material properties have been taken from ref. [22] (see Tables 1 and 2). The internal radius of the tank is 100 mm and the volume is 10 Liter. The other parameters; ply thickness, liner thickness and applied pressure are 0.42, 3 mm and 164.5 MPa, respectively. For Type III tank, it has been considered that the liner and reinforcing materials are Aluminum T6061 and composite T700 Carbon/Epoxy. The main purpose of this problem is to compare failure indexes obtained by the present study and results by Alcantar [22] for Type III pressure vessel.
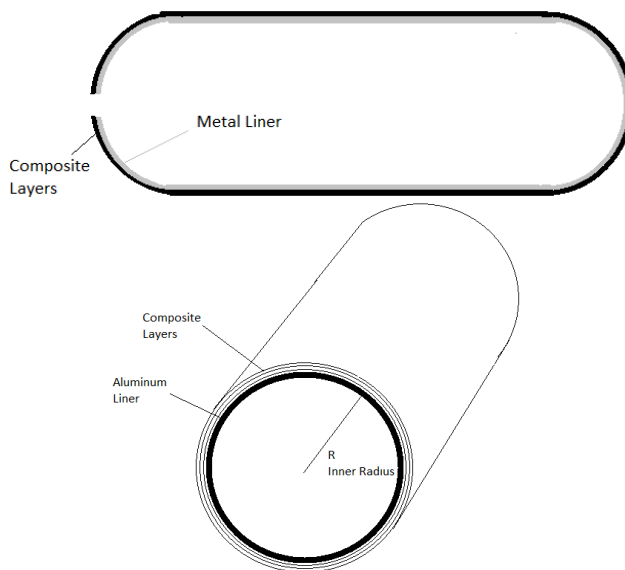

Fig. 1 Configuration of the Type III tank

Table 1 Mechanical properties of T6061 Al and T700 Carbon/Epoxy composite materials [22]

	E_1(GPa)	E_2(GPa)	G_{12}(GPa)	v_{12}	v_{23}	σ_{ult} (MPa)
6061Al	70	70	26.92	0.3	0.3	310
T700 Carbon/Epoxy	181	10.3	5.86	0.28	0.49	-

Table 2 Strength parameters of T700 Carbon/Epoxy composite materials [22]

$\sigma_{1_{ult}}^T$(MPa)	$\sigma_{1_{ult}}^C$(MPa)	$\sigma_{2_{ult}}^T$(MPa)	$\sigma_{2_{ult}}^C$(MPa)	$\tau_{12_{ult}}$(MPa)
2150	2150	298	298	778

Problem 2:

194

In Problem 2, stress calculation and determination of the burst pressure according to Classical Laminated Plate Theory and Tsai-Wu failure criterion have been done for Aluminum- Carbon Epoxy pressure vessel (Type III). The burst pressure results have been compared with experimental and Finite Element analysis results by Liu et al [32]. The pressure vessel is composed of T6061 Aluminum liner and T700 Carbon/Epoxy composite plies. Mechanical properties and strength parameters of these materials are given in Table 3 and 4, respectively.

Table 3 Mechanical properties of T6061 Al and T700 Carbon/Epoxy composite materials [32]

	E_1(GPa)	E_2(GPa)	G_{12}(GPa)	v_{12}	v_{23}	σ_{yield} (MPa)
6061Al	70	70	26.92	0.3	0.3	246
T700 Carbon/Epoxy	154.1	10.3	5.17	0.28	0.49	-

Table 4 Strength parameters of T700 Carbon/Epoxy composite materials [32]

$\sigma_{1_{ult}}^{T}$(MPa)	$\sigma_{1_{ult}}^{C}$(MPa)	$\sigma_{2_{ult}}^{T}$(MPa)	$\sigma_{2_{ult}}^{C}$(MPa)	$\tau_{12_{ult}}$(MPa)
2500	1250	60	186	85

Geometrical properties for considered Type III pressure vessel have been indicated in Table 5.

Table 5 Geometrical Dimensions of the Type-III Pressure Vessel [32]

Internal Radius (mm)	Stacking Sequences (°)	Liner Thickness (mm)	Thickness of Composite Ply (mm)
44	[90_2/18.6/ -18.6/ 90_2 /28.9/ -28.9/ 90_2]	1.8	0.42

Problem 3:

The main aim of the Problem 3 is to see effect of usage different Carbon/Epoxy materials on the design and optimization of the Type III hydrogen storage tanks. The optimization problems have been solved by using Differential Evolution Method. The materials considered in this problem and their properties are listed in Table 6. Thickness of the each lamina (t_{liner}) and radius of the tanks (R) are 1.8 and 200 mm, respectively. In the failure index calculations the strength properties of the materials are taken from references [22], [32] and [34].

The mathematical representation of Problem 3 is defined as

Minimize: $F_{T[1]}$ (Tsai-Wu Failure Index at first layer)

Constraints: $\{F_{\text{Tsai-Wu}}, F_{\text{Hashin-Rotem}}, F_{\text{Maximum Stress}}\} \leq 1,$

$\{\theta_1, \theta_2, \theta_3, ...\} \, \epsilon \, \{0, 15, 30, 45, 60, 75, 90\}$

P_{burst} > 35 MPa, Symmetric & Balance stacking sequences:

$[\pm\theta_1 / \pm\theta_2 / \pm\theta_3 / ... / \mp\theta_3 / \mp\theta_2 / \mp\theta_1]$

Table 6 Mechanical properties of the materials

	E_1 (GPa)	E_2 (GPa)	G_{12} (GPa)	v_{12}	σ_{yield} (MPa)
T6061Al [22]	70	70	26.92	0.3	246
Carbon/Epoxy (T700) [22]	181	10.3	5.86	0.28	-
Carbon/Epoxy (IM6/SC1081) [34]	177	10.8	7.6	0.27	-
Carbon/Epoxy (T700s) [32]	154.1	9.66	5.17	0.25	

4. Results and Discussion

There are three main stages to find the optimum solution. The first step is to enter the material properties and calculate the stiffness matrices. The second part is to give the fiber orientation angles parametrically and arriving at the objective function. The last step is running the optimization algorithms (Differential Evolution) and finding the optimum solution (see Figure 2).

Problem 1:

The results of the Problem 1 can be summarized as: (i) the present failure indexes calculations using Tsai-Wu and Maximum Stress theories have been compared with the results achieved by Finite Element Method (see Table 7). It is shown that good agreement between the present and FEM results by Alcantar et al. [22] are obtained. (ii) For Type III pressure vessels, the burst pressure prediction has also been developed by using the stress-strain matrix calculation method given in Alcantar et al. [22].

Table 7 Results of the Tsai-Wu and Maximum Stress failure indexes

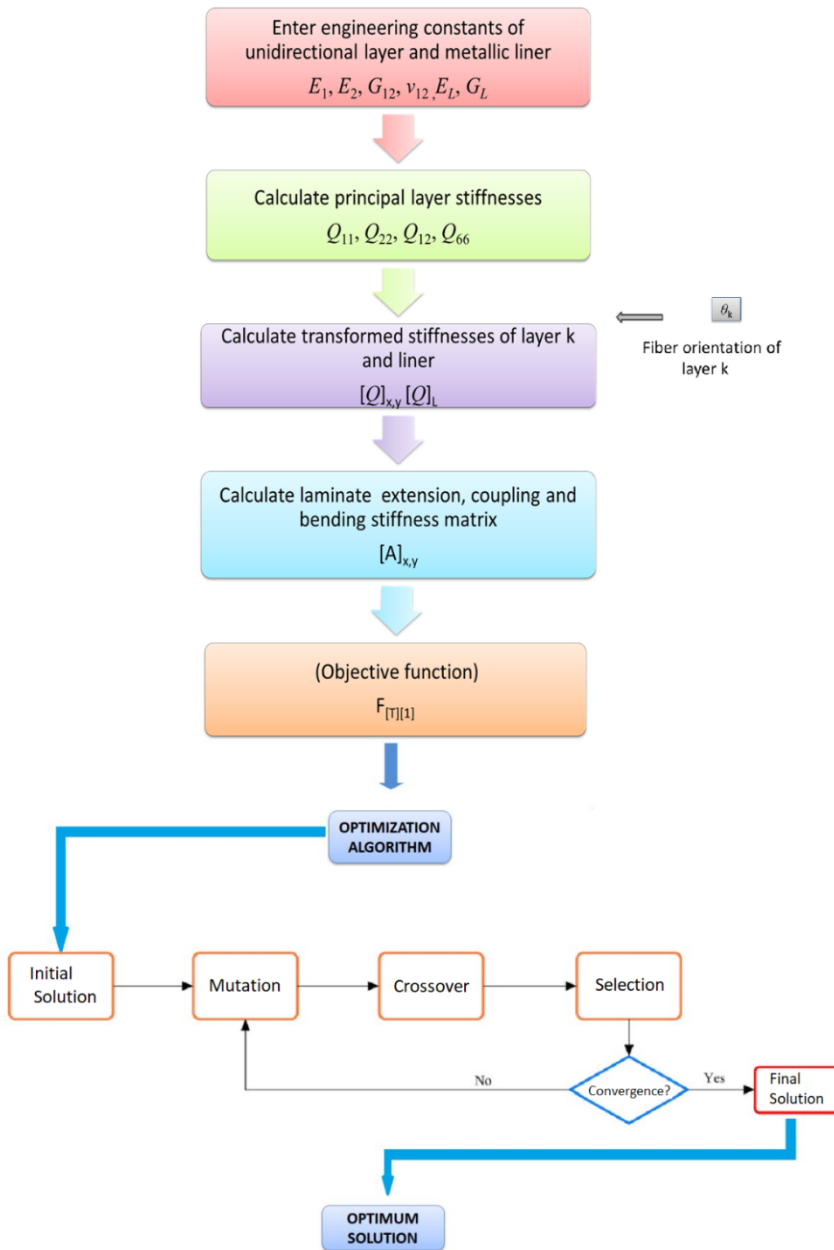| Burst Pressure (MPa)	Failure Index			
	Tsai-Wu [22]	Tsai-Wu [Present Study]	Maximum Stress[22]	Maximum Stress [Present Study]
164.5	0.83	0.85	0.90	1.00
105	0.51	0.35	0.56	0.64

Fig. 2 Optimization process of the Type III Hydrogen Storage Tank

Problem 2:

Table 8 shows comparison results of the calculated burst pressure values that satisfy Tsai-Wu failure criterion constraint with the experimental and Finite Element analysis results. It can be seen that good agreement is reached between the experimental and Tsai-Wu burst pressure values with the error of 15%. Additionally, burst pressure values

calculated by using Maximum Stress and Hashin-Rotem failure criterion have predicted with the maximum error of 30 %. It should be noted that the predicted results in the manuscript is based on first ply failure theories. Therefore, progressive failure approach would produce more accurate results.

Table 8 Comparison of the burst pressure for Problem 2

	First Ply Failure				
	Tsai-Wu [Present Study]	Maximum Stress [Present Study]	Hashin-Rotem [Present Study]	Finite Element [15]	Experimental [15]
Burst Pressure (MPa)	90	70	70	99.8	106

It is seen that the predictions made here are based on the first ply failure criteria, however, the progressive failure approach should be used in order to obtain the final ply failure burst pressure. It should also be noted that the use of first ply failure approach provide safer designs during the optimization procedure.

Problem 3:

The optimization problem given above has been solved for different three Carbon/Epoxy materials. After the solution of the optimization problems, three different stacking sequences design of Type III pressure vessel having burst pressure over the 35 MPa have been reached (see Table 9). According the results:

(i)   it is seen that obtaining distinct designs having total thickness satisfying over 35 MPa burst pressure are possible.

(ii)   All of the designs have symmetric, balanced and integer fiber orientation angles, therefore, it provides easy manufacturable productions.

Table 9 Optimization results of the Problem 3 for different Carbon/ Epoxy composites

Design Cases	Material	Ply Thickness (mm)	Stacking Sequences	Ply No	Total Thickness (mm)
a	Carbon/E poxy (T700)	0.42	$[90_2/\mp60/\pm45/\mp45/\mp45/\pm45/\pm45]_s$	28	11.76
b	Carbon/E poxy (T700s)	0.127	$[90_2/\mp30/90_2/\pm60/\pm30/90_4/\pm45/\pm45/\pm60/\mp30/\pm30/90_4/\pm45/\pm30/90_4/\mp45/\mp45]_s$	80	10.16
c	Carbon/E poxy (IM6/SC1 081)	0.127	$[90_2/\pm30/\mp75/\pm60/\pm60/\pm30/\pm45/90_4/\pm30/\pm60/\pm45/\mp45/\pm30/90_2/\pm30/\mp45/\mp30/90_2/\pm45/$	112	14.224

$$\mp 45/\pm 30/90_4/\mp 75/$$
$$\mp 45/90_2]_s$$

The results of the present study can be summarized as;

    (i)   A manufacturable Type III pressure vessel designs have been proposed for different materials.

    (ii)   Even for the same materials, different mechanical properties have significantly changed the design. Additionally, small differences on thickness of the ply and mechanical properties have been found to be important for the same material types.

5. Conclusion

In this study, the failure analysis and the optimum designs of composite hydrogen storage tanks have been investigated. The optimizations have been carried out for different Aluminum-Carbon/Epoxy (Type III) materials. The number of plies and fiber orientation angles of the laminated composites are taken as design variables. Single-objective optimization approach has been selected for design and mathematical verification of model problems. The burst pressure calculations for Type III hydrogen storage tanks have been compared with the experimental and Finite Element Method results from the literature. It can be seen that good agreement is reached between them with the maximum error of 10%. Even for the three Carbon/Epoxy materials in close proximity to each other, design and optimization results have crucially changed. It can be concluded that the generalization for optimum stacking sequences of Carbon/ Epoxy materials should be avoided.

References

[1] George G, Schillebeeckx SJD. *Managing Natural Resources: Organizational Strategy. Behaviour and Dynamics*, Edward Elgar Publishing, Massachusetts, MA, USA, 2018. https://doi.org/10.4337/9781786435729

[2] Cox R. *Hydrogen: Its Technology and Implication: Production Technology*, CRC Press, Florida, USA, 2018.

[3] Barthelemy H, Weber H, Barbier F. Hydrogen storage: recent improvements and industrial perspectives. International Journal of Hydrogen Energy, 2017; 42(11): 7254-7262. https://doi.org/10.1016/j.ijhydene.2016.03.178

[4] Cohen D. Influence of filament winding parameters on composite vessel quality and strength. Composites Part A: Applied Science and Manufacturing, 1997; 28(12): 1035-1047. https://doi.org/10.1016/S1359-835X(97)00073-0

[5] Barbero EJ. *Introduction to Composite Materials Design*. CRC Press, Florida, NW, USA, 2017.

[6] Liu PF, Chu JK, Hou SJ, Xu P, Zheng JY. Numerical simulation and optimal design for composite high-pressure hydrogen storage vessel: A review. Renewable and Sustainable Energy Reviews, 2012; 16(4): 1817-1827. https://doi.org/10.1016/j.rser.2012.01.006

[7] Messager T, Pyrz M, Gineste B, Chauchot P. Optimal laminations of thin underwater composite cylindrical vessels. Composite Structures, 2002; 58(4): 529-537. https://doi.org/10.1016/S0263-8223(02)00162-9

[8] Parnas L, Katırcı N. Design of fiber-reinforced composite pressure vessels under various loading conditions. Composite Structures, 2002; 58(1): 83-95. https://doi.org/10.1016/S0263-8223(02)00037-5

[9] Tabakov PY. Multi-dimensional design optimization of laminated structures using an improved genetic algorithm. Composite Structures, 2001; 54 (2): 349-354. https://doi.org/10.1016/S0263-8223(01)00109-X

[10] Richard F, Perreux D. A reliability method for optimization of [+ φ,− φ] n fiber reinforced composite pipes. Reliability Engineering and System Safety, 2000; 68(1): 53-59. https://doi.org/10.1016/S0951-8320(00)00002-8

[11] Lin DT, Hsieh JC, Chindakham N, Hai PD. Optimal design of a composite laminate hydrogen storage vessel. International Journal of Energy Research, 2013; 37(7): 761-768. https://doi.org/10.1002/er.2983

[12] Han MG, Chang SH. Failure analysis of a Type III hydrogen pressure vessel under impact loading induced by free fall. Composite Structures, 2015; 127: 288-297. https://doi.org/10.1016/j.compstruct.2015.03.027

[13] Park WR, Fatoni NF, Kwon OH. Evaluation of stress and crack behavior using the extended finite element method in the composite layer of a type III hydrogen storage vessel. Journal of Mechanical Science and Technology, 2018; 32(5): 1995-2002. https://doi.org/10.1007/s12206-018-0407-2

[14] Nikbakt S, Kamarian S, Shakeri M. A review on optimization of composite structures part I: Laminated Composites. Composite Structures, 2018; 195: 158-185. https://doi.org/10.1016/j.compstruct.2018.03.063

[15] Roque CMC, Martins PALS. Maximization of fundamental frequency of layered composites using differential evolution optimization. Composite Structures, 2018; 183(1): 77-83. https://doi.org/10.1016/j.compstruct.2017.01.037

[16] Chakraborty D, Dutta A. Optimization of FRP composites against impact induced failure using island model parallel genetic algorithm. Composites Science and Technology, 2005; 65(13): 2003-2013. https://doi.org/10.1016/j.compscitech.2005.03.016

[17] Jing Z, Sun Q, Silberschmidt VV. Sequential permutation table method for optimization of stacking sequence in composite laminates. Composite Structures, 2016; 141: 240-252. https://doi.org/10.1016/j.compstruct.2016.01.052

[18] Irisarri FX, Bassir DH, Carrere N, Maire JF. Multiobjective stacking sequence optimization for laminated composite structures. Composites Science and Technology, 2009; 69(7-8): 983-990. https://doi.org/10.1016/j.compscitech.2009.01.011

[19] Zu L, Koussios S, Beukers A. Design of filament-wound circular toroidal hydrogen storage vessels based on non-geodesic fiber trajectories. International Journal of Hydrogen Energy, 2010; 35(2): 660-670. https://doi.org/10.1016/j.ijhydene.2009.10.062

[20] Francescato P, Gillet A, Leh D, Saffre P. Comparison of optimal design methods for type 3 high-pressure storage tanks. Composite Structures, 2012; 94(6): 2087-2096. https://doi.org/10.1016/j.compstruct.2012.01.01

[21] Pelletier JL, Vel SS. Multi-objective optimization of fiber reinforced composite laminates for strength, stiffness and minimal mass. Computers and Structures, 2006; 84(29-30): 2065-2080. https://doi.org/10.1016/j.compstruc.2006.06.001

[22] Alcantar V, Ledesma S, Aceves SM, Ledesma E, Saldana A. Optimization of type III pressure vessels using genetic algorithm and simulated annealing. International Journal of Hydrogen Energy, 2017; 42(31): 20125-20132. https://doi.org/10.1016/j.ijhydene.2017.06.146

[23] Tsai SW. Strength Characteristics of Composite Materials. NASA CR-224, National Aeronautics and Space Administration, Washington, D. C., 1965:5-43.

[24] Hill R. A Theory of the Yielding and Plastic Flow of Anisotropic Materials. Proceedings of the Royal Society, 1948; 193: 281-297.

[25] Hoffman O. The Brittle Strength of Orthotropic Materials. Journal of Composite Materials, 1967; 1: 200-206. https://doi.org/10.1177/002199836700100210

[26] Kaw AK. *Mechanics of composite materials*, CRC press, Florida, USA, 2005.

[27] Aydin L, Artem HS, Oterkus E, Gundogdu O, Akbulut H. Mechanics of fiber composites. Fiber Technology for Fiber-Reinforced Composites, Woodhead Publishing, Cambridge, England, 2017:5-50. https://doi.org/10.1016/B978-0-08-101871-2.00002-3

[28] Hashin Z, Rotem A. A fatigue failure criterion for fiber reinforced materials. Journal of Composite Materials, 1973; 7(4): 448-464. https://doi.org/10.1177/002199837300700404

[29] Ozturk S, Aydin L, Kucukdogan N, Celik E. Optimization of lapping processes of silicon wafer for photovoltaic applications. Solar Energy, 2018; 164: 1-11. https://doi.org/10.1016/j.solener.2018.02.039

[30] Ozturk S, Aydin L, Celik E. A comprehensive study on slicing processes optimization of silicon ingot for photovoltaic applications. Solar Energy, 2018; 161: 109-124. https://doi.org/10.1016/j.solener.2017.12.040

[31] Aydin L, Artem HS. Design and optimization of fiber composites. Fiber Technology for Fiber-Reinforced Composites. Woodhead Publishing, Cambridge, England, 2017:299-315. https://doi.org/10.1016/B978-0-08-101871-2.00014-X

[32] Liu P, Xing L, Zheng J. Failure analysis of carbon fiber/epoxy composite cylindrical laminates using explicit finite element method. Composites Part B: Engineering, 2014; 56: 54-61. https://doi.org/10.1016/j.compositesb.2013.08.017

[33] Zheng J, Liu P. Elasto-plastic stress analysis and burst strength evaluation of Al-carbon fiber/epoxy composite cylindrical laminates. Computational Materials Science, 2008; 42(3): 453-461. https://doi.org/10.1016/j.commatsci.2007.09.011

[34] Mian HH, Wang G, Dar UA, Zhang W. Optimization of composite material system and lay-up to achieve minimum weight pressure vessel. Applied Composite Materials, 2013; 20(5): 873-889. https://doi.org/10.1007/s10443-012-9305-4

Research on
Engineering Structures & Materials

C
O
N
T
E
N
T

Research on
Engineering
Structures & Materials

Research Group